



**POLITECNICO DI TORINO**

Master of Science in Civil Engineering

Master's degree Thesis

**Numerical Study on the Structural Performance of Concrete-  
Infilled Cold-Formed Steel Moment-Resisting Connections**

**Supervisor:**

Prof. Francesco Tondolo

**Co-supervisor:**

PhD. Eng. Ward Alarab Safarani

**Candidate:**

Mahsa Salehi Moghadam

July 2025

## Acknowledgements

I would like to express my sincere gratitude to my academic supervisor, Prof. Francesco Tondolo, for his expert guidance, continuous support, and valuable feedback throughout the development of this thesis. I am also deeply thankful to Eng. Ward Alarab Safarani for his technical supervision, constructive input, and encouragement at every stage of the work. Their mentorship played a key role in shaping this research and pushing it forward.

I am truly grateful to my family for their unconditional love and support throughout this journey. A heartfelt thanks goes to Mirco, whose presence, patience, and motivation made a real difference during challenging moments. I would also like to thank all my friends, colleagues, and anyone who supported or helped me in any way, your kindness and encouragement have been deeply appreciated and will never be forgotten.

## Abstract

Cold-formed steel (CFS) structural elements are gaining increasing attention in modern construction due to their superior material efficiency and economic advantages compared to traditional hot-rolled steel members. In addition to cost and weight benefits, CFS production generally involves lower energy consumption and reduced CO<sub>2</sub> emissions, making it a more environmentally sustainable choice. However, their use in seismic regions presents notable challenges, primarily because the thin-walled nature of CFS profiles makes them vulnerable to local and distortional buckling. Moreover, conventional CFS bolted moment connections often demonstrate limited structural and seismic performance.

To address these limitations, this research proposes a novel connection enhancement technique involving concrete infill in the beam-column joint region. The goal is to enhance structural integrity by mitigating buckling and improving load transfer mechanisms. A finite element model, developed using ABAQUS software, incorporates nonlinear material behavior and interaction effects, and is validated against experimental data. This validated model provides a reliable basis for evaluating the proposed connection's performance in comparison to existing methods in seismic applications.

Before analyzing the main folded flange (FF) beam configurations, the finite element modeling approach was validated using simulations of curved back-to-back CFS beams under cyclic loading. The numerical results closely matched the experimental observations in terms of stiffness, strength, and degradation trends, confirming the reliability of the adopted numerical modeling strategy. From a practical and execution standpoint, folded flange geometries were found to be more suitable than curved flanges due to their ease of fabrication and assembly. Consequently, the study transitions from curved flange validation models to folded flange configurations for the main analysis.

Subsequently, various FF beam-column connections were studied, including unstiffened, stiffened, and fully bonded concrete-infilled models. The Concrete Damaged Plasticity (CDP) model was used to simulate concrete, following validation through compressive, tensile, and flexural tests.

Normalized moment-rotation results showed that unstiffened connections (FFNSS/FFNSD) exhibited the weakest performance, placing them in the partial-strength category. Steel-stiffened connections (FFWSS/FFWSD) demonstrated substantially improved behavior, qualifying them as full-strength. Among fully bonded models, the elastic variant (FFFBES) exhibited the most stable and enhanced performance, clearly achieving full-strength classification. In contrast, the CDP-based model (FFFBPD) displayed an early peak followed by a sudden decline due to damage localization and post-peak degradation.

These results confirm that integrating concrete infill, especially with full bonding and appropriate material modeling can enhance the structural performance of CFS beam-column connections in terms of strength. However, the post-peak behavior and the interaction between concrete and steel after concrete yielding require further investigation and validation against experimental tests to ensure reliable performance predictions.

# Table of Contents

## Contents

|   |     |
|---|-----|
| Acknowledgements .....  | III |
| Abstract .....  | IV  |
| Table of Contents.....  | V   |
| List of Figures .....   | VII |
| List of Tables.....   | XI  |
| Chapter 1. Introduction .....   | 1   |
| 1.1 Background .....  | 1   |
| 1.2 Cold-formed Steel Sections .....  | 3   |
| 1.2.1 Manufacturing.....  | 3   |
| 1.2.2 Form of Cold-formed Steel Sections.....                                 | 6   |
| 1.2.3 Materials .....   | 10  |
| 1.3 Design Standards.....   | 13  |
| 1.4 Connections and Joints .....  | 16  |
| 1.5 Applications .....  | 25  |
| Chapter 2. Literature Review .....  | 32  |
| 2.1 Cold Formed Steel Bolted Moment Frames .....                              | 32  |
| Chapter 3. Methodology .....  | 55  |
| 3.1 Introduction.....   | 55  |
| 3.2 Finite Element Method .....   | 55  |
| 3.3 Abaqus Software.....  | 56  |
| 3.4 Introduction to Abaqus .....  | 57  |
| 3.5 Basic Principles of Abaqus .....  | 58  |
| 3.6 Modeling Stages .....   | 59  |
| 3.6.1 Creating the Geometric Model (Part Module) .....                        | 59  |
| 3.6.2 Defining Material Properties (Property Module) .....                    | 63  |
| 3.6.3 Assembling Different Parts (Assembly Module).....                       | 64  |
| 3.6.4 Creating and Configuring Analysis Steps (Step Module).....              | 65  |
| 3.6.5 Defining Surface Interactions (Interaction Module) .....                | 65  |
| 3.6.6 Boundary Condition and Loading Definition Assignment (Load Module)..... | 66  |
| 3.6.7 Finite Element Meshing (Mesh Module) .....                              | 68  |



|   |     |
|---|-----|
| 3.7 Validation of Numerical Simulations Against Experimental Results..... | 72  |
| Chapter 4. Modeling of Plain Concrete .....                               | 79  |
| 4.1 Elasto-Plastic Modeling of Concrete .....                             | 79  |
| 4.2 The Concrete Damaged Plasticity .....                                 | 79  |
| 4.3 The Drucker-Prager Model.....   | 85  |
| 4.4 Uniaxial Compressive Behavior .....                                   | 88  |
| 4.5 Uniaxial Tensile Behavior.....  | 92  |
| 4.6 Concrete Test Modeling: Compression, Tension, and Bending.....        | 93  |
| 4.6.1 Uniaxial Compressive Test.....                                      | 93  |
| 4.6.2 Uniaxial Tensile Test .....   | 97  |
| 4.6.3 Three-Point Bending Test .....                                      | 99  |
| 4.7 Case Study Description and Modeling Assumptions .....                 | 104 |
| Chapter 5. Result and Numerical Investigation.....                        | 109 |
| 5.1 Overview of Finite Element Models .....                               | 109 |
| 5.2 Comparative Analysis of Normalized Moment–Rotation Behavior .....     | 122 |
| 5.2.1 Main Model Response: FFNSS and FFNSD .....                          | 122 |
| 5.2.2 Steel Stiffener Models: FFWSS and FFWSD.....                        | 123 |
| 5.2.3 Fully Bonded Concrete Infill Models – FFFBES and FFFBPD .....       | 123 |
| Chapter 6. Conclusions and Recommendations for Future Work .....          | 125 |
| Summary of Key Findings .....   | 125 |
| Future Work Recommendations .....   | 127 |
| Bibliography.....   | 128 |

# List of Figures

|   |    |
|---|----|
| Figure 1.1: Cold-formed steel portal frame (photograph courtesy of CSB) [3].  | 2  |
| Figure 1.2: Stages in roll forming a simple section (Rhodes, 1991) [5].   | 4  |
| Figure 1.3: Roll Form Machines.   | 4  |
| Figure 1.4: Forming steps in press braking process [5].   | 5  |
| Figure 1.5: Industrial brake press [5].   | 6  |
| Figure 1.6: Forming of folding [5].   | 6  |
| Figure 1.7: Typical forms of sections for cold-formed members [8].  | 7  |
| Figure 1.8: Examples of cold-formed members and profiled sheets [8].  | 8  |
| Figure 1.9: Typical forms of stiffeners for cold-formed members and sheeting [8].   | 9  |
| Figure 1.10: Typical edge stiffeners [8].   | 9  |
| Figure 1.11: Typical intermediate longitudinal stiffeners [8].  | 9  |
| Figure 1.12: Groove welds in butt joints.   | 17 |
| Figure 1.13: Arc spot weld with weld washer [8].  | 18 |
| Figure 1.14: Arc spot welds [8].  | 19 |
| Figure 1.15: Arc Seam Weld (Elongated arc spot weld) [8].   | 19 |
| Figure 1.16: Fillet Welds-Lap Joint [9].  | 20 |
| Figure 1.17: Fillet Welds-T-Joint [9].  | 20 |
| Figure 1.18: Fillet Weld Failure Modes [9].   | 20 |
| Figure 1.19: Fillet welded lap connection [8].  | 21 |
| Figure 1.20: types of flare groove welds.   | 22 |
| Figure 1.21: Flare Groove Weld Failure Modes [9].   | 22 |
| Figure 1.22: Failure modes of bolted connections in shear.  | 23 |
| Figure 1.23: Failure modes for bolted connections in tension.   | 23 |
| Figure 1.24: Washers for self-tapping/self-drilling screws: a) metal washers; b) elastomeric washers; c), d) elastomeric bonded or vulcanized to metal washers.                                     | 24 |
| Figure 1.25: Thread types for thread-forming screws.  | 24 |
| Figure 1.26: Threads and points of thread-cutting screws.   | 24 |
| Figure 1.27: (a) fastenings of roof sheeting on purlins; (b) fastening of sheeting at an eave detail; (c) fastening of wall sheeting on side rails; (d) fastenings of wall cassettes on stanchions. | 25 |
| Figure 1.28: Renovated Piatt Place [10].  | 26 |
| Figure 1.29: CFS-framed structure of Victory Hall at the University of North Texas [9].   | 27 |
| Figure 1.30: CFS truss [10].  | 27 |
| Figure 1.31: Individual roof trusses [10].  | 28 |
| Figure 1.32: Roof trusses are lifted into place, completing the steel framing of a Cantiro home in Edmonton [10].   | 28 |
| Figure 1.33: steel floor trusses allow for long spans [9].  | 29 |
| Figure 1.34: Prefab CFS exterior panels [10].   | 30 |
| Figure 1.35: Prefab's exterior finished panels [10].  | 30 |
| Figure 1.36: Cold-Formed Steel Deck [9].  | 31 |
| Figure 1.37: The University of Hawaii Atherton Hall project features cold-formed steel (CFS) framing for a rehabilitation project [10].   | 31 |
| Figure 2.38: CFS-SBMF connections [12].   | 32 |

|  |    |
|--|----|
| Figure 2.39: Stiffening evolution of flat elements toward curved elements [13].  | 35 |
| Figure 2.40: CFS beam–column connections: (a) Diamond column, cross through plates and curved flange beam. (b) Assembled moment resistant connections [13].  | 36 |
| Figure 2.41: In-plane action of the column walls with through plate connection [13].   | 36 |
| Figure 2.42: Different out-of-plane stiffener configurations for the CFS beam–column connections, M– $\theta$ curves and local buckling deformation of beam without stiffener and beam with optimum stiffener.   | 37 |
| Figure 2.43 :Moment–rotation curves of the beams.  | 39 |
| Figure 2.44 : $MMP - \theta$ hysteretic curves and local buckling deformation of Specimens A1–3  | 41 |
| Figure 2.45: Instrumentation sketches of the specimens [15].   | 43 |
| Figure 2.46: Simplified FE model for slip-bearing action of the bolts.   | 45 |
| Figure 2.47: Bearing behavior of a single bolt against steel plate used in CFS bolted-moment connection [18].  | 48 |
| Figure 2.48: Details of the back-to-back beam cross-sectional dimensions (in mm), L = 2000 mm.   | 49 |
| Figure 2.49: Different bolt arrangements.  | 49 |
| Figure 2.50: Cross-sectional classification based on moment-rotation curves.   | 50 |
| Figure 3.51: plate with a hole, showing the deformation of the plate overlaid on its undeformed state. The plate is fixed along the left edge and subjected to a tensile stress of 1000 psi along the right edge. The maximum horizontal displacement is $7.046 \times 10^{-4}$ in | 56 |
| Figure 3.52: General Workflow of Abaqus Software   | 58 |
| Figure 3.53: Model parts   | 60 |
| Figure 3.54: Models A1, A2 and A3  | 61 |
| Figure 3.55: CFS column and curved flange beam parts   | 62 |
| Figure 3.56: through-plate part  | 62 |
| Figure 3.57: beam and column stiffeners parts  | 63 |
| Figure 3.58: Assembled parts for FE model A1   | 64 |
| Figure 3.59: FE modelling of the tested connections: (a) bolt arrangement and (b) discrete fasteners [19].   | 66 |
| Figure 3.60: Boundary conditions of the FE models.   | 67 |
| Figure 3.61: Cyclic loading protocol adopted from AISC 341-16 [43].  | 68 |
| Figure 3.62: Element Groups in ABAQUS/CAE  | 69 |
| Figure 3.63: Quadratic (Parabolic) Element   | 70 |
| Figure 3.64: Linear Element  | 70 |
| Figure 3.65: Mesh configuration for beam   | 71 |
| Figure 3.66: Mesh configuration for beam and column stiffeners   | 71 |
| Figure 3.67: Mesh configuration for column and throughplate  | 72 |
| Figure 3.68: Mesh of assembled components  | 72 |
| Figure 3.69: Moment–Rotation comparison ( $M/M_p$ vs. $\theta$ ) between FEA and experimental result for Model A1 under cyclic loading [15].   | 73 |
| Figure 3.70: Left – Von Mises stress field (MPa) from FEA simulation of Model A1 at peak load. Right – Photograph of specimen A1 after cyclic testing, showing deformations in predicted regions.  | 74 |
| Figure 3.71: Moment–Rotation comparison ( $M/M_p$ vs. $\theta$ ) between FEA and experimental result for Model A2 under cyclic loading [15].   | 75 |
| Figure 3.72: Left – Von Mises stress field (MPa) from FEA simulation of Model A2 at peak load. Right – Photograph of specimen A2 after cyclic testing, showing deformations in predicted regions.  | 76 |

|  |     |
|--|-----|
| Figure 3.73: Moment–Rotation comparison ( $M/M_p$ vs. $\theta$ ) between FEA and experimental result for Model A3 under cyclic loading [15].....   | 77  |
| Figure 3.74: Left – Von Mises stress field (MPa) from FEA simulation of Model A3 at peak load. Right – Photograph of specimen A3 after cyclic testing, showing deformations in predicted regions. .... | 78  |
| Figure 4.75: Response of concrete to uniaxial loading in tension (a) and compression (b).....  | 81  |
| Figure 4.76: Post-failure stress-displacement curve .....  | 82  |
| Figure 4.77: Post-failure stress-fracture energy curve.....  | 82  |
| Figure 4.78: Yield surface in plane stress. ....   | 83  |
| Figure 4.79: Illustration of the effect of the compression stiffness recovery parameter $\omega_c$ .....   | 84  |
| Figure 4.80: Uniaxial load cycle (tension-compression-tension) .....   | 85  |
| Figure 4.81: Linear Drucker-Prager yield criterion for concrete [30] .....   | 86  |
| Figure 4.82: stress plane deviation shape for different values of K .....  | 87  |
| Figure 4.83: Equivalent uniaxial stress–strain curves for confined and unconfined .....  | 89  |
| Figure 4.84: geometry of folded flange beam .....  | 89  |
| Figure 4.85: Schematic representation of the stress-strain relation for structural analysis .....  | 90  |
| Figure 4.86: Stress–strain curves for C40 concrete cylinder using the CDP model with 20 mm and 40 mm mesh sizes (compressive test).....  | 95  |
| Figure 87: Stress–strain curves for C40 concrete cylinder using the DP model with 20 mm and 40 mm mesh sizes (compressive test).....   | 96  |
| Figure 4.88: cylindrical mesh sizes 20mm and 40 mm from left to right respectively. ....   | 97  |
| Figure 4.89: Stress–strain curves for C40 concrete cylinder using the CDP model with 20 mm and 40 mm mesh sizes .....  | 98  |
| Figure 4.90: Stress–strain curves for C40 concrete cylinder using the DP model with 20 mm and 40 mm mesh sizes .....   | 98  |
| Figure 4.91: Plot of Maximum Principal Stress Distribution Numerical model (DP) of a cylinder under uniaxial tensile loading, Mesh 20mm.....   | 99  |
| Figure 4.92: Plot of Maximum Principal Stress Distribution Numerical model (CDP) of a cylinder under uniaxial tensile loading, Mesh 20mm.....  | 99  |
| Figure 4.93: Comparison of Numerical (CDP) and Experimental Load-Deflection Curves under Three-Point Bending .....   | 101 |
| Figure 4.94: Comparison of Numerical (DP) and Experimental Load-Deflection Curves under Three-Point Bending.....   | 102 |
| Figure 4.95: Maximum principal stress contour for the mesh 50, CDP Model. ....   | 102 |
| Figure 4.96 : Maximum principal stress contour for the mesh 50, DP Model .....   | 103 |
| Figure 4.97: Cross-sectional geometry of the cold-formed folded flange beam used in the numerical model.....   | 104 |
| Figure 4.98: Folded flange beam-to-column connection with 600 mm concrete infill at the joint region. ....   | 105 |
| Figure 4.99: Meshed Model of Folded Flange Beam with Concrete Infill In the Dynamic Explicit analysis .....  | 108 |
| Figure 4.100` : Meshed Model of Folded Flange Beam with Concrete Infill In the Static General analysis .....   | 108 |
| Figure 5.101: Von Mises Stress Contour- FFNSS Model .....  | 110 |
| Figure 5.102: Force-Displacement Diagram-FFNSS Model .....   | 111 |

|   |     |
|---|-----|
| Figure 5.103: Moment-Rotation Diagram-FFNSS Model .....                       | 111 |
| Figure 5.104: Von Mises Stress Contour- FFNSD Model.....                      | 112 |
| Figure 5.105: Force-Displacement Diagram-FFNSD Model .....                    | 112 |
| Figure 5.106: Moment-Rotation Diagram-FFNSD Model.....                        | 113 |
| Figure 5.107: Von Mises Stress Contour- FFWSS Model.....                      | 114 |
| Figure 5.108: Force-Displacement Diagram-FFWSS Model.....                     | 114 |
| Figure 5.109 : Moment-Rotation Diagram-FFWSS Model.....                       | 115 |
| Figure 110: Von Mises Stress Contour- FFWSD Model .....                       | 115 |
| Figure 5.111: Force-Displacement Diagram-FFWSD Model .....                    | 116 |
| Figure 5.112: Moment-Rotation Diagram-FFWSD Model .....                       | 116 |
| Figure 5.113: Von Mises Stress Contour- FFFBES Model.....                     | 117 |
| Figure 5.114: Von Mises Stress Contour in CFS Beam- FFFBES Model.....         | 117 |
| Figure 5.115: Von Mises Stress Contour in Concrete Infill- FFFBES Model.....  | 118 |
| Figure 5.116: Force–displacement curve for FFFBES Model .....                 | 118 |
| Figure 5.117: Moment-Rotation Diagram-FFFBES Model.....                       | 119 |
| Figure 5.118: Von Mises Stress Contour- FFFBPD Model .....                    | 119 |
| Figure 5.119: Von Mises Stress Contour in CFS Beam- FFFBPD Model .....        | 120 |
| Figure 5.120: Von Mises Stress Contour in Concrete Infill- FFFBPD Model ..... | 120 |
| Figure 5.121 : Force–displacement curve for FFFBPD Model .....                | 121 |
| Figure 5.122: Moment-Rotation Diagram-FFFBPD Model .....                      | 121 |

## List of Tables

|   |     |
|---|-----|
| Table 1: (a) Nominal values of basic yield strength $f_{yb}$ and ultimate tensile strength $f_u$ [8]..... | 10  |
| Table 2: (b) Nominal values of basic yield strength $f_{yb}$ and ultimate tensile strength $f_u$ [8]..... | 11  |
| Table 3: Comparison of Key Aspects Across Standards .....   | 15  |
| Table 4: The specimens configurations [14]. .....   | 39  |
| Table 5: The specimens configurations [15] .....  | 42  |
| Table 6: Different channel types and bolt configurations [17]. .....                                      | 47  |
| Table 7: 3D graphical representations of different connection types [19]. .....                           | 53  |
| Table 8: material properties for beam and gusset plate .....  | 64  |
| Table 9: strength and deformation characteristics for concrete [32].....                                  | 92  |
| Table 10: FEA Models .....  | 109 |

# Chapter 1. Introduction

## 1.1 Background

The building sector plays a significant role in the energy consumption landscape. In the European Union (EU), nearly 50% of final energy consumption is attributed to heating and cooling, with 80% of this energy used in buildings [1]. Furthermore, the building sector contributes approximately 36% of the EU's total CO<sub>2</sub> emissions, underscoring its critical importance in decarbonization efforts [1].

Producing one ton of hot-rolled steel using traditional methods typically generates between 1.85 and 2.33 tons of CO<sub>2</sub> emissions. This variation depends on factors such as the energy mix and the efficiency of the production process [2]. Building materials play a significant role in the environmental impact of the construction industry, primarily due to the energy consumption and carbon dioxide emissions associated with their production. Despite this, the environmental consequences of material choices are often overlooked by designers. However, selecting more sustainable materials and optimizing construction methods can considerably reduce the embodied energy and CO<sub>2</sub> emissions in a building [3].

With proper design, cold-formed steel (CFS) sections offer several notable advantages, including:

- Advantages include higher strength-to-weight ratio of the steel [3].
- CFS members can be manufactured at any length since they are produced from rolled plates [4].
- ease of erection by manual semi-skilled labour without the need for an on-site crane [4].
- maintenance-free pre-galvanized cold-formed steel sections that do not require painting to prevent rusting [4].
- Slender and efficient structures may be created in a wide range of forms e.g. portals, trusses, arches, etc [5].



*Figure 1.1: Cold-formed steel portal frame (photograph courtesy of CSB) [3].*

Cold-formed, thin-walled construction used to be limited to applications where weight savings were of primary concern, such as the aircraft and automotive industries. However, following improvements in manufacturing techniques, corrosion protection, product availability, understanding of the structural response and sophistication of design codes for cold-formed sections, light-gauge construction has become increasingly widespread [6]. The use of thin, cold-formed material brings about a number of special design problems that are not generally encountered when using ordinary hot-rolled sections [6]. These include:

- non-uniform distribution of material properties due to cold working
- rounded corners and the calculation of geometric properties
- local buckling
- distortional buckling
- torsional and flexural torsional buckling
- shear lag
- flange curling
- web crushing, crippling and buckling



## 1.2 Cold-formed Steel Sections

Cold-formed steel (CFS) sections are structural elements made by shaping thin steel sheets, strips, or plates at room temperature through processes such as rolling, pressing, or stamping. Unlike hot-rolled steel, cold-formed steel is not heated during its manufacturing, which enables precise shaping and dimensional accuracy while enhancing its mechanical properties like strength and stiffness [7].

### 1.2.1 Manufacturing

Cold-formed members are typically manufactured using one of the following processes:

- Roll forming;

Roll forming consists of feeding a continuous steel strip through a series of opposing rolls to progressively deform the steel plastically to form the desired shape. Each pair of rolls produces a fixed amount of deformation in a sequence of type shown in Figure 1.2a. Each pair of opposing rolls is called a stage as shown in Figure 1.2. In general, the more complex the cross-sectional shape, the greater the number of stages required. In the case of cold-formed rectangular hollow sections, the rolls initially form the section into a circular section and a weld is applied between the opposing edges of the strip before final rolling (called sizing) into a square or rectangular shape [5].

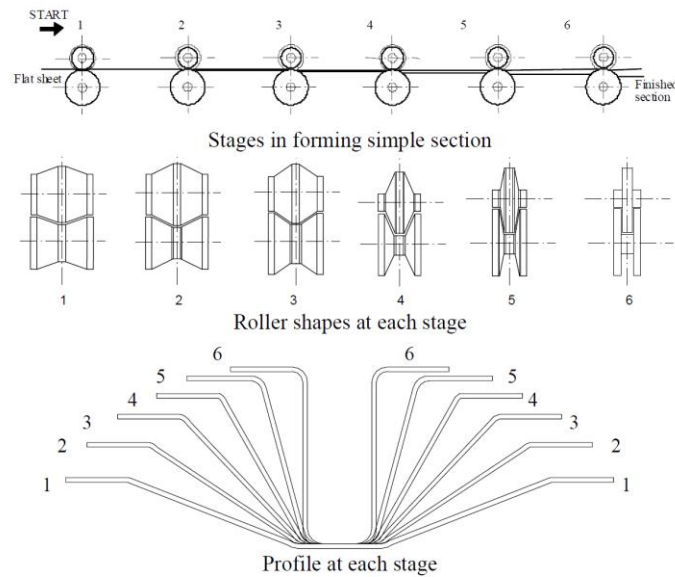


Figure 1.2: Stages in roll forming a simple section (Rhodes, 1991) [5].

A significant limitation of roll forming is the time taken to change rolls for different size sections. Consequently, adjustable rolls are often used, which allows a rapid change to a different section width or depth. Figure 1.3 shows an industrial roll forming line [5].

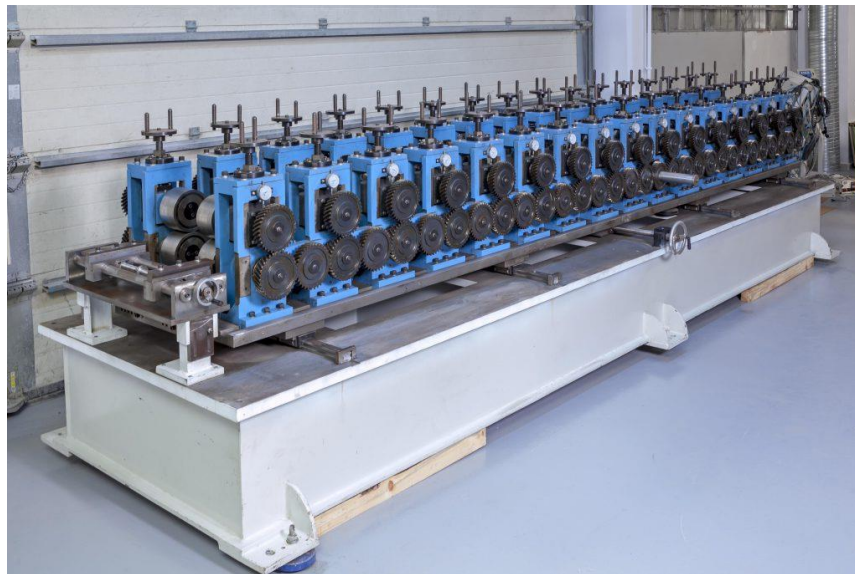


Figure 1.3: Roll Form Machines.

- press braking;

Press braking is widely utilized for manufacturing cold-formed steel sections due to its capability to produce a wide variety of cross-sectional forms. In this process, a strip of steel

is pressed between shaped dies to achieve the desired profile shape (Figure 1.4). Each bend in the section is typically formed separately, allowing for precise control over the geometry. A typical brake press is illustrated in Figure 1.5 [5].

While press braking offers flexibility in creating custom profiles, it has limitations. The process is generally restricted to sections with lengths under 5 meters, although some industrial presses can produce members up to 8 meters long. Additionally, the geometry of the sections is constrained by the capabilities of the press and the material's properties. Despite these limitations, press braking remains an essential process in the fabrication of cold-formed steel members, especially for prototypes and small-batch production [5].

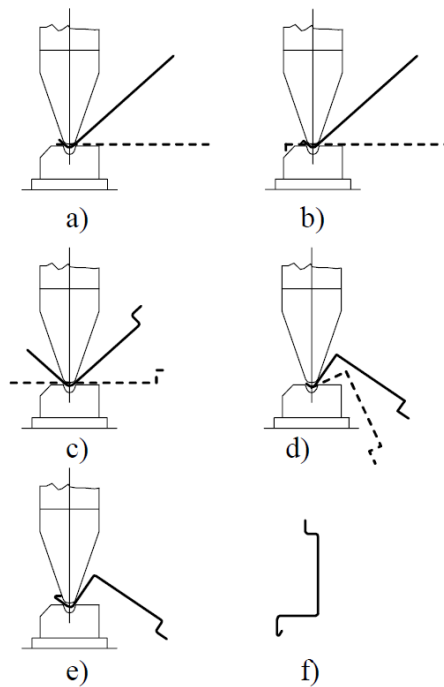


Figure 1.4: Forming steps in press braking process [5].



Figure 1.5: Industrial brake press [5].

- Folding;

Folding is the simplest process, in which specimens of short lengths, and of simple geometry are produced from a sheet of material by folding a series of bends (Figure 1.6). This process has very limited applications [5].

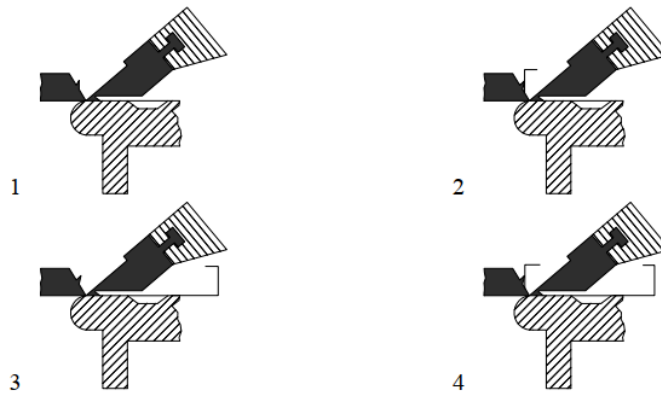


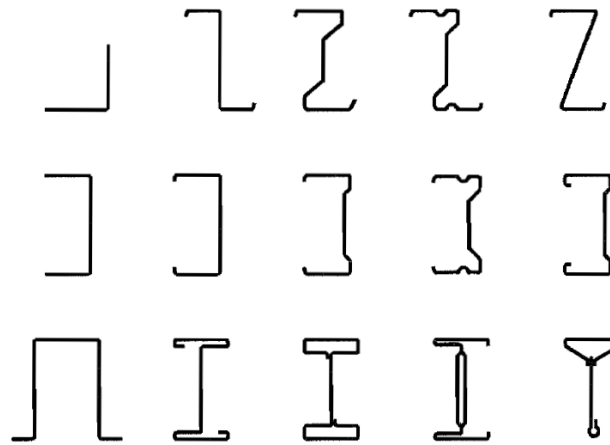
Figure 1.6: Forming of folding [5].

### 1.2.2 Form of Cold-formed Steel Sections

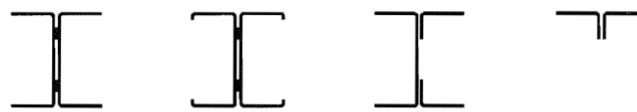
Cold-formed members and profiled sheets have within the permitted tolerances a constant nominal thickness over their entire length and may have either a uniform cross section or a tapering cross section along their length [8].

The cross-sections of cold-formed members and profiled sheets essentially comprise a number of plane elements joined by curved elements [8].

Typical forms of sections for cold-formed members are shown in figure 1.7.



a) Single open sections



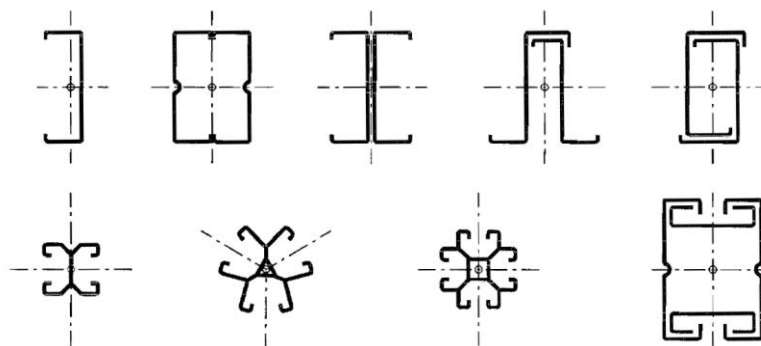
b) Open built-up sections



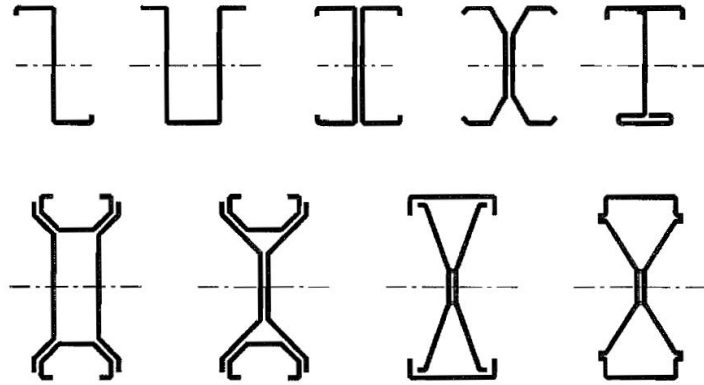
c) Closed built-up sections

Figure 1.7: Typical forms of sections for cold-formed members [8].

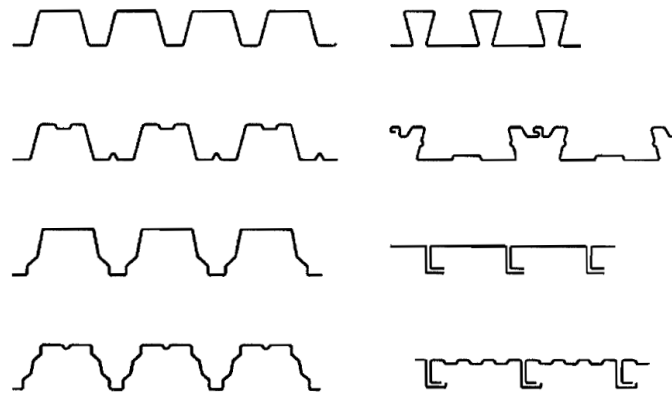
Examples of cross-sections for cold-formed members and sheets are illustrated in figure 1.8.



a) Compression members and tension members



*b) Beams and other members subject to bending*



*c) Profiled sheets and liner trays*

*Figure 1.8: Examples of cold-formed members and profiled sheets [8].*

Cross sections of cold-formed members and sheets may either be unstiffened or incorporate longitudinal stiffeners in their webs or flanges, or in both. Typical forms of stiffeners for cold-formed members and sheets are shown in figure 1.9.



*a) Folds and bends*

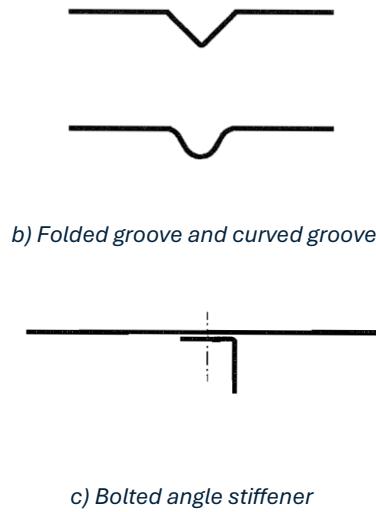


Figure 1.9: Typical forms of stiffeners for cold-formed members and sheeting [8].

Longitudinal flange stiffeners may be either edge stiffeners or intermediate stiffeners.

Typical edge stiffeners are shown in figure 1.10.



Figure 1.10: Typical edge stiffeners [8].

Typical intermediate longitudinal stiffeners are illustrated in figure 1.11.

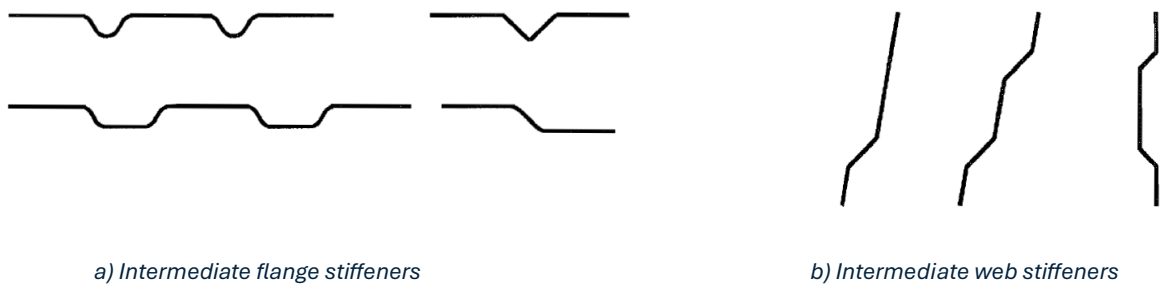


Figure 1.11: Typical intermediate longitudinal stiffeners [8].

### 1.2.3 Materials

All steels used for cold-formed members and profiled sheets should be suitable for cold-forming and welding, if needed. Steels used for members and sheets to be galvanized should also be suitable for galvanizing [8].

The nominal values of material properties given in this Section should be adopted as characteristic values in design calculations [8].

This part of EN 1993 covers the design of cold formed members and profiled sheets fabricated from steel grades material conforming to the steel listed in table 1.

*Table 1: (a) Nominal values of basic yield strength  $f_{yb}$  and ultimate tensile strength  $f_u$  [8]*

| Type of steel  | Standard         | Grade    | $f_{yb}$ N/mm <sup>2</sup> | $f_u$ N/mm <sup>2</sup> |
|--|------------------|----------|----------------------------|-------------------------|
| Hot rolled products of non-alloy structural steels. Part 2: Technical delivery conditions for non alloy structural steels                              | EN 10025: Part 2 | S 235    | 235                        | 360                     |
|  |                  | S 275    | 275                        | 430                     |
|  |                  | S 355    | 355                        | 510                     |
| Hot-rolled products of structural steels. Part 3: Technical delivery conditions for normalized/normalized rolled weldable fine grain structural steels | EN 10025: Part 3 | S 275 N  | 275                        | 370                     |
|  |                  | S 355 N  | 355                        | 470                     |
|  |                  | S 420 N  | 420                        | 520                     |
|  |                  | S 460 N  | 460                        | 550                     |
|  |                  | S 275 NL | 275                        | 370                     |
|  |                  | S 355 NL | 355                        | 470                     |
|  |                  | S 420 NL | 420                        | 520                     |
| Hot-rolled products of structural steels. Part 4: Technical delivery conditions for thermomechanical rolled weldable fine grain structural steels      | EN 10025: Part 4 | S 460 NL | 460                        | 550                     |
|  |                  | S 275 M  | 275                        | 360                     |
|  |                  | S 355 M  | 355                        | 450                     |
|  |                  | S 420 M  | 420                        | 500                     |
|  |                  | S 460 M  | 460                        | 530                     |
|  |                  | S 275 ML | 275                        | 360                     |
|  |                  | S 355 ML | 355                        | 450                     |
|  |                  | S 420 ML | 420                        | 500                     |
|  |                  | S 460 ML | 460                        | 530                     |

NOTE 1: For steel strip less than 3 mm thick conforming to EN 10025, if the width of the original strip is greater than or equal to 600 mm, the characteristic values may be given in the National Annex. Values equal to 0,9 times those given in Table 1 are recommended [8].

NOTE 2: For other steel materials and products see the National Annex. Examples for steel grades that may conform to the requirements of this standard are given in Table 2 [8].



Table 2: (b) Nominal values of basic yield strength  $f_{yb}$  and ultimate tensile strength  $f_u$  [8]

| Type of steel  | Standard         | Grade     | $f_{yb}$ N/mm <sup>2</sup> | $f_u$ N/mm <sup>2</sup> |
|--|------------------|-----------|----------------------------|-------------------------|
| Cold reduced steel sheet of structural quality   | ISO 4997         | CR 220    | 220                        | 300                     |
|  |                  | CR 250    | 250                        | 330                     |
|  |                  | CR 320    | 320                        | 400                     |
| Continuous hot dip zinc coated carbon steel sheet of structural quality  | EN 10326         | S220GD+Z  | 220                        | 300                     |
|  |                  | S250GD+Z  | 250                        | 330                     |
|  |                  | S280GD+Z  | 280                        | 360                     |
|  |                  | S320GD+Z  | 320                        | 390                     |
|  |                  | S350GD+Z  | 350                        | 420                     |
| Hot-rolled flat products made of high yield strength steels for cold forming. Part 2: Delivery conditions for thermomechanically rolled steels | EN 10149: Part 2 | S 315 MC  | 315                        | 390                     |
|  |                  | S 355 MC  | 355                        | 430                     |
|  |                  | S 420 MC  | 420                        | 480                     |
|  |                  | S 460 MC  | 460                        | 520                     |
|  |                  | S 500 MC  | 500                        | 550                     |
|  |                  | S 550 MC  | 550                        | 600                     |
|  |                  | S 600 MC  | 600                        | 650                     |
|  |                  | S 650 MC  | 650                        | 700                     |
|  | EN 10149: Part 3 | S 260 NC  | 260                        | 370                     |
|  |                  | S 315 NC  | 315                        | 430                     |
|  |                  | S 355 NC  | 355                        | 470                     |
|  |                  | S 420 NC  | 420                        | 530                     |
| Cold-rolled flat products made of high yield strength micro-alloyed steels for cold forming  | EN 10268         | H240LA    | 240                        | 340                     |
|  |                  | H280LA    | 280                        | 370                     |
|  |                  | H320LA    | 320                        | 400                     |
|  |                  | H360LA    | 360                        | 430                     |
|  |                  | H400LA    | 400                        | 460                     |
| Continuously hot-dip coated strip and sheet of steels with higher yield strength for cold forming  | EN 10292         | H260LAD   | 240 2)                     | 340 2)                  |
|  |                  | H300LAD   | 280 2)                     | 370 2)                  |
|  |                  | H340LAD   | 320 2)                     | 400 2)                  |
|  |                  | H380LAD   | 360 2)                     | 430 2)                  |
|  |                  | H420LAD   | 400 2)                     | 460 2)                  |
| Continuously hot-dipped zinc-aluminium (ZA) coated steel strip and sheet   | EN 10326         | S220GD+ZA | 220                        | 300                     |
|  |                  | S250GD+ZA | 250                        | 330                     |
|  |                  | S280GD+ZA | 280                        | 360                     |
|  |                  | S320GD+ZA | 320                        | 390                     |
|  |                  | S350GD+ZA | 350                        | 420                     |
| Continuously hot-dipped aluminium-zinc (AZ) coated steel strip and sheet   | EN 10326         | S220GD+AZ | 220                        | 300                     |
|  |                  | S250GD+AZ | 250                        | 330                     |
|  |                  | S280GD+AZ | 280                        | 360                     |
|  |                  | S320GD+AZ | 320                        | 390                     |
|  |                  | S350GD+AZ | 350                        | 420                     |
| Continuously hot-dipped zinc coated strip and sheet of mild steel for cold forming   | EN 10327         | DX51D+Z   | 140 1)                     | 270 1)                  |
|  |                  | DX52D+Z   | 140 1)                     | 270 1)                  |
|  |                  | DX53D+Z   | 140 1)                     | 270 1)                  |

1) Minimum values of the yield strength and ultimate tensile strength are not given in the standard. For all steel grades a minimum value of  $140 \text{ N/mm}^2$  for yield strength and  $270 \text{ N/mm}^2$  for ultimate tensile strength may be assumed [8].

2) The yield strength values given in the names of the materials correspond to transversal tension. The values for longitudinal are given in the table [8].

## 1.3 Design Standards

This part provides an overview of the design codes and standards for cold-formed steel (CFS) structures across various countries. We will examine the key principles, methodologies, and applications of standards such as Eurocode 3 (Europe), AISI S100 (North America), AS/NZS 4600 (Australia and New Zealand), IS 801 (India), and GB 50018 (China). Each section will outline the unique aspects of these codes, offering a clear understanding of how they address regional engineering, safety, and construction requirements while adhering to the global fundamentals of CFS design.

- Europe
  - Standard: Eurocode 3 (EN 1993-1-3: Design of Steel Structures – Part 1-3)
    - Focuses on thin-walled steel members and sheeting.
    - Includes rules for buckling resistance (local, global, and distortional).
    - Specifies methods for effective cross-sectional properties considering local instability.
    - Incorporates detailed guidance on lightweight steel framing and trapezoidal sheeting.
    - Incorporates provisions for fasteners like bolts, screws, and rivets.
    - National Annexes adjust parameters like safety factors to suit specific countries.
- North America
  - Standard: AISI S100 (North American Specification for the Design of Cold-Formed Steel Structural Members)
    - Governs the design of cold-formed steel members in buildings and other structures.
    - Covers both Allowable Stress Design (ASD) and Load and Resistance Factor Design (LRFD).
    - Emphasizes effective width and direct strength methods to account for local, distortional, and global buckling.
    - Incorporates provisions for connections, bracing, and fastener design.
    - Applies to the USA, Canada, and Mexico with regional adaptations.

- Supplementary Standards:
  - AISI S240: Cold-formed steel framing standards.
  - CSA S136: Canadian adaptation aligned with AISI S100.
- Australia and New Zealand
  - Standard: AS/NZS 4600 (Cold-Formed Steel Structures Standard)
    - Covers structural elements and systems in buildings and other structures.
    - Allows for both Limit State Design (LSD) and Working Stress Design (WSD).
    - Uses effective width and direct strength methods for section design.
    - Includes provisions for bracing, connections, and corrosion protection.
    - Encourages the use of advanced analysis methods for complex structures.
- India
  - Standard: IS 801 (Indian Standard: Code of Practice for Use of Cold-Formed Light Gauge Steel Structural Members in General Building Construction)
    - Focuses on light-gauge steel structures for building applications.
    - Specifies methods for computing effective widths under local buckling.
    - Emphasizes structural detailing and fastener design for reliability.
    - Provides additional design rules for earthquake-prone regions.
- China
  - Standard: GB 50018 (Technical Code for Cold-Formed Thin-Wall Steel Structures)
    - Provides guidelines for design, fabrication, and construction of cold-formed steel structures.
    - Includes rules for effective cross-sections, stability analysis, and serviceability.
    - Incorporates load combinations and safety factors suited to China's specific requirements.
- Japan
  - Standard: JIS G 3350 (General Requirements for Light Gauge Steel Members)
    - Emphasizes seismic resilience of cold-formed steel structures.
    - Provides methods for addressing local and global instability.

- Focuses on material specifications and connection design.
- United Kingdom
  - Standard: BS EN 1993-1-3 (Eurocode 3 Adaptation)
    - National Annex adjusts safety factors and material properties for local use.
    - Extensively used for light steel framing systems and building envelopes.
- South Africa
  - Standard: SANS 10162-2 (The Structural Use of Steel – Part 2: Cold-Formed Steel Structures)
    - Aligns closely with North American standards.
    - Focuses on effective section properties and buckling considerations.

*Table 3: Comparison of Key Aspects Across Standards*

| Aspect               | North America (AISI)        | Europe (Eurocode 3)         | Australia/NZ (AS/NZS)       | India (IS 801) | China (GB 50018)       |
|----------------------|-----------------------------|-----------------------------|-----------------------------|----------------|------------------------|
| Design Methods       | ASD, LRFD                   | Limit States                | LSD, WSD                    | WSD            | LSD                    |
| Buckling Modes       | Local, distortional, global | Local, distortional, global | Local, distortional, global | Local          | Local, global          |
| Corrosion Resistance | Coating specs included      | Optional                    | Mandatory                   | Optional       | Coating specs included |
| Connections          | Detailed provisions         | Comprehensive               | Comprehensive               | Moderate       | Detailed provisions    |

## 1.4 Connections and Joints

Connections in cold-formed steel structures are used for [5]:

- connecting steel sheets to supporting structure (thin-to-thick), e.g. roof sheeting to purlins, cladding sheeting to side-rails etc.;
- interconnecting two or more sheets (thin-to-thin), e.g. seam fastening of sheeting;
- assembling bar members (thin-to-thin or thick-to-thick), e.g. for framed structures, trusses etc.

In comparison with hot-rolled sections, the behaviour of connections in cold-formed steel elements is influenced by the reduced stiffness of thin walls. Therefore, additional effects are, for example, the tilting of the fastener in hole bearing failure under the shear distortion of the sheet when the fastener is loaded in tension and the sheet is pulled over the head of the fastener. This is the reason why specific technologies and related design procedures, either by calculation or calculation assisted by testing, have been developed for cold-formed steel structures [5].

Welds, bolts, screws, rivets, and other special devices such as metal stitching and adhesives are generally used for cold-formed steel connections [8]

- Rivets

While hot rivets have little application in cold-formed steel construction, cold rivets find considerable use, particularly in special forms such as blind rivets (for application from one side only), tubular rivets (to increase bearing area), high shear rivets, and explosive rivets. For the design of connections using cold rivets, the provisions for bolted connections may be used as a general guide, except that the shear strength of rivets may be quite different from that of bolts. Additional design information on the strength of rivets should be obtained from manufacturers or from tests [9].

- Special Devices

Special devices include: (1) metal stitching, achieved by tools that are special developments of the common office stapler, and (2) connecting by means of special clinching tools that draw the sheets into interlocking projections. Most of these connections are proprietary devices for which information on strength of connections must be obtained from manufacturers or from tests carried out by or for the user [9].

- Welded Connections

Welds used for cold-formed steel construction may be classified as fusion welds (or arc welds) and resistance welds. Fusion welding is used for connecting cold-formed steel members to each other as well as connecting such members to heavy, hot-rolled steel framing (such as floor panels to beams of the steel frame). It is used in groove welds, arc spot welds, fillet welds, and flare-groove welds [9].

- Groove Welds in Butt Joints

Groove or butt welds may be difficult to produce in thin sheet and are therefore not as common as fillet, spot and slot welds.

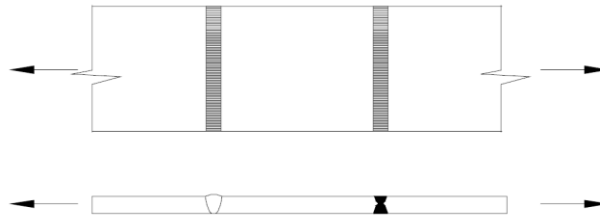


Figure 1.12: Groove welds in butt joints.

- Arc Spot Welds

Arc spot welds (puddle welds) used for connecting thin sheets, and are similar to plug welds used for relatively thicker plates. The difference between plug welds and arc spot welds is that the former are made with pre-punched holes, but no pre-punched holes are required for the latter. Instead, a hole is burned in the top sheet by the arc and then filled with weld metal to fuse it to the bottom sheet or a framing member [9].

- Arc spot welds should not be designed to transmit any forces other than in shear [8].
- Arc spot welds should not be used through connected parts or sheets with a total thickness  $\sum t$  of more than 4 mm.
- Arc spot welds should have an interface diameter  $d_s$  of not less than 10 mm.
- If the connected part or sheet is less than 0,7 mm thick, a weld washer should be used, (see figure 1.13)

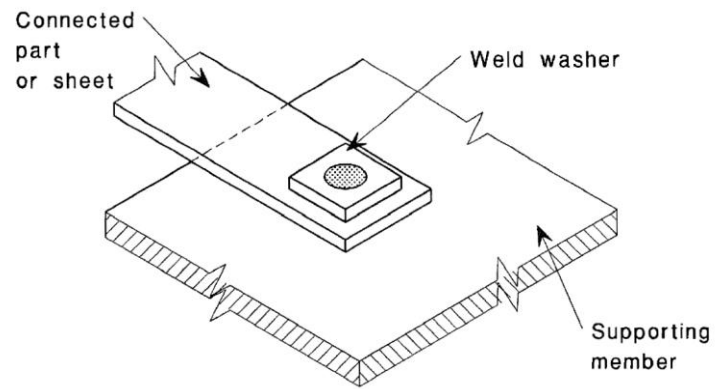
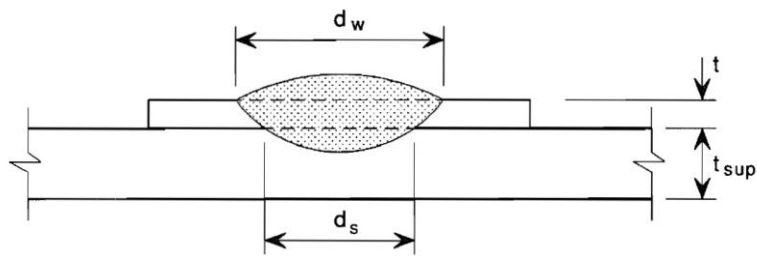
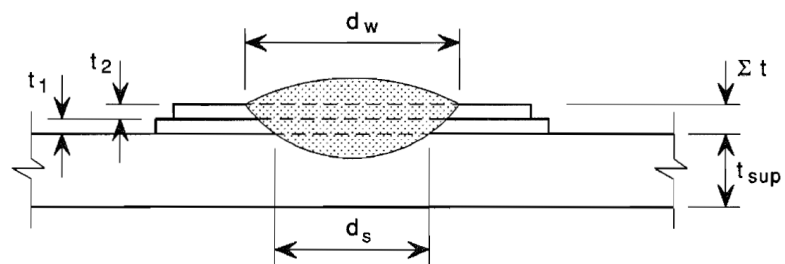


Figure 1.13: Arc spot weld with weld washer [8].

- Arc spot welds should have adequate end and distances as given in the code.

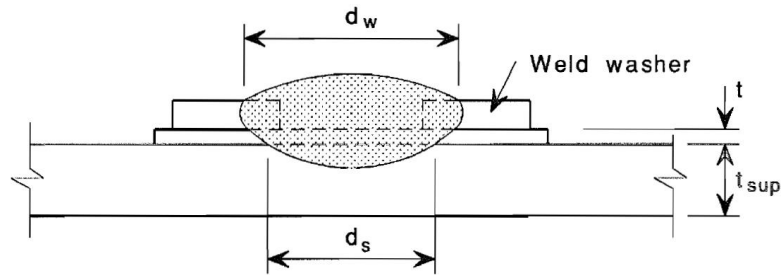


a) Single connected sheet ( $\sum t = t$ )



b) Two connected sheets ( $\sum t = t_1 + t_2$ )





c) Single connected sheet with weld washer  
Figure 1.14: Arc spot welds [8].

### Arc Seam Welds

Arc seam welds shall apply only to the following joints [9]:

- Sheet to thicker supporting member in the flat position.
- Sheet to sheet in the horizontal or flat position.

The general behavior of arc seam welds is similar to that of arc spot welds.

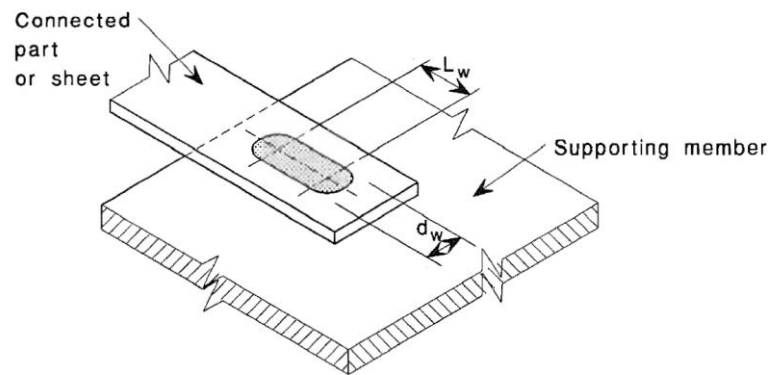


Figure 1.15: Arc Seam Weld (Elongated arc spot weld) [8].

### ○ Fillet Welds

For fillet welds in lap joint specimens, research conducted by Peköz and McGuire (1979) observed the following [9]:

- The dimension of the weld leg at the sheet edge ( $w_1$ ) is generally equal to the sheet thickness, while the other leg ( $w_2$ ) is typically two to three times longer than  $w_1$ .

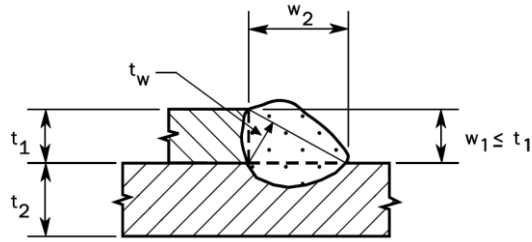


Figure 1.16: Fillet Welds-Lap Joint [9].

- In such connections, the fillet weld throat is commonly larger than that of conventional fillet welds of the same size, such as the T-Joint shown below.

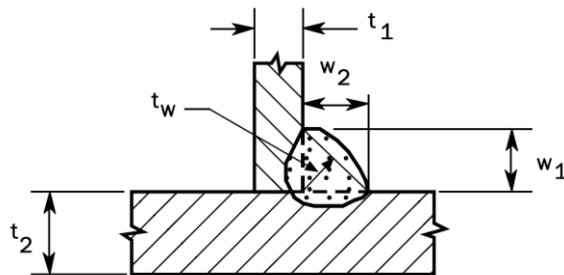
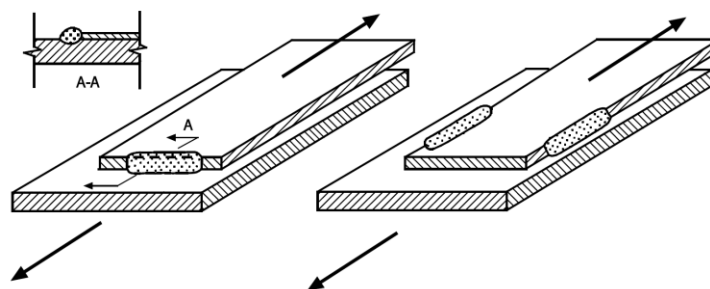


Figure 1.17: Fillet Welds-T-Joint [9].

- Ultimate failure in fillet-welded joints usually occurs by tearing of the plate adjacent to the weld.



a) Transverse Fillet Sheet Tear

b) Longitudinal Fillet Sheet Tear

Figure 1.18: Fillet Weld Failure Modes [9].

- If a combination of end fillets and side fillets is used in the same connection, its total resistance should be taken as equal to the sum of the resistances of

the end fillets and the side fillets. The position of the centroid and realistic assumption of the distribution of forces should be taken into account [8].

- The effective length  $L_w$  of a fillet weld should be taken as the overall length of the full-size fillet, including end returns. Provided that the weld is full size throughout this length, no reduction in effective length need be made for either the start or termination of the weld.
- Fillet welds with effective lengths less than 8 times the thickness of the thinner connected part should not be designed to transmit any forces.

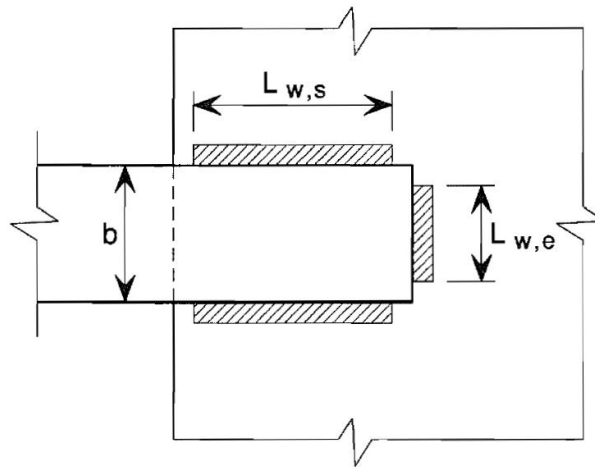


Figure 1.19: Fillet welded lap connection [8].

#### ○ Flare-Groove Welds

Flare groove welds shall apply to welding of joints in any position, either sheet to sheet for flare V-groove welds, sheet to sheet for flare bevel groove welds, or sheet to thicker steel member for flare bevel groove welds [9]. Flare bevel grooved welds and flare V-groove welds are used to produce built-up sections [5].

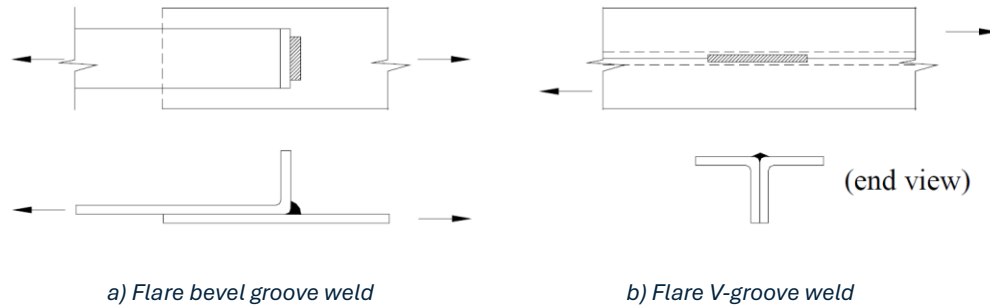


Figure 1.20: types of flare groove welds.

The primary mode of failure in cold-formed steel sections welded by flare groove welds, whether loaded transversely or longitudinally, is sheet tearing along the contour of the weld [9].

- For thicker sections, the effective throats of the welds may be less than the thickness of the channel, making weld failure critical.
- In 2001, the specification was revised to mandate weld strength checks for plate thicknesses greater than 0.10 inches (2.54 mm).

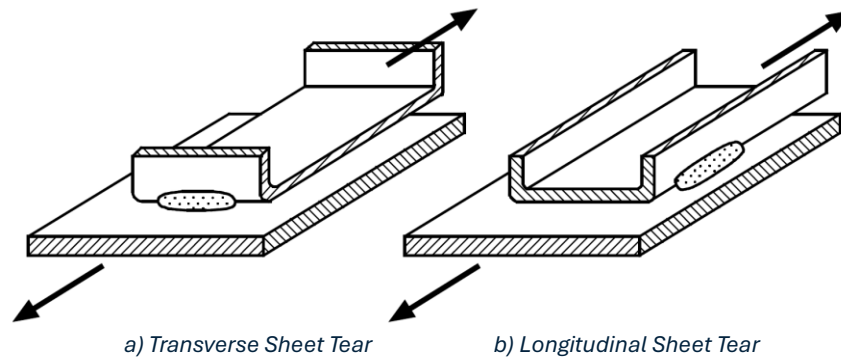


Figure 1.21: Flare Groove Weld Failure Modes [9].

- Bolted Connections

Bolted connections are normally used as shear, tension or moment resistant connections in cold-formed steel framing. Tests have revealed the following basic types of failure for thin steel bolted connections working in shear and tension [5]:

- Failure modes in shear:
  - Shearing of the bolt: rupture (Figure 1.22a) or crushing (Figure 1.22b);
  - Bearing (yield) and/or piling of thinner material (Figure 1.22c). When both materials are thin, yielding of both sheets may occur together with bolt tilting (Figure 1.22d);
  - Tearing of the sheet in the net sections (Figure 1.22e);

- End failure by shearing of thin material (Figure 1.22f);

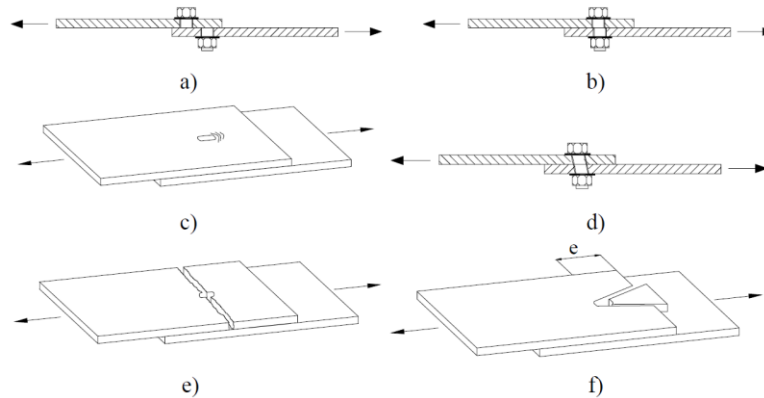


Figure 1.22: Failure modes of bolted connections in shear.

- Failure modes in tension:

- Tension failure or rupture of bolt (Figure 1.23a);
- Pull-through failure (Figure 1.23b).

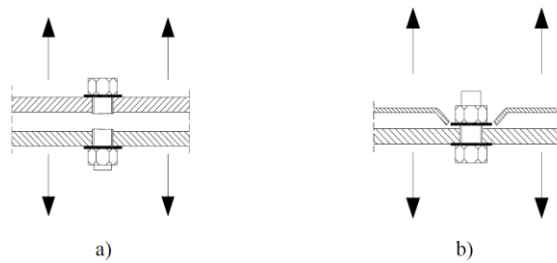


Figure 1.23: Failure modes for bolted connections in tension.

- Screw Connections

The two main types of screws are self-tapping and self-drilling screws. Most screws will be combined with washers to improve the load bearing capacity of the fastening or to make the fastening self-sealing as shown in Figure 1.24.

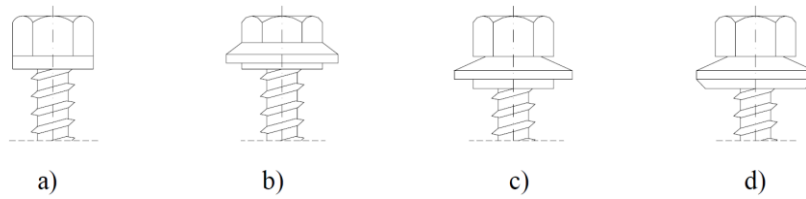


Figure 1.24: Washers for self-tapping/self-drilling screws: a) metal washers; b) elastomeric washers; c), d) elastomeric bonded or vulcanized to metal washers.

Self-tapping screws tap their counterthread in a prepared hole. They can be classified as thread-forming and thread-cutting.

Figure 1.25 shows the thread types for thread-forming screws (Yu *et al*,1993). Type A is used for fastening thin sheets to thin sheets. Type B is used for fixing to steel bases of thicknesses greater than 2 mm. Type C is generally used for fixing to thin steel bases up to 4 mm thick.

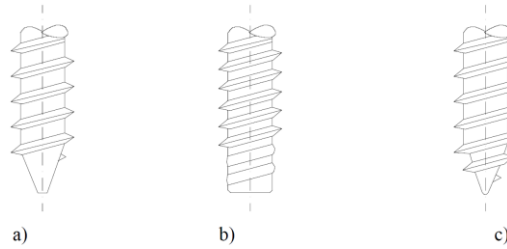


Figure 1.25: Thread types for thread-forming screws.

Thread-cutting screws are used for fastening to thicker metal bases, but their resistance to loosening is typically lower than that of thread-forming screws. Figure 1.26 shows examples of threads and points of thread-cutting screws.

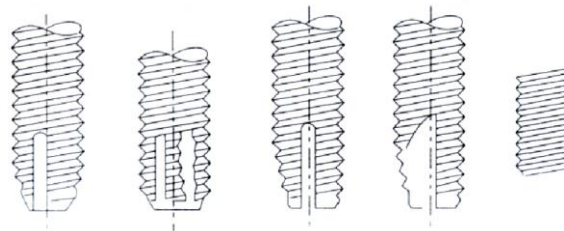


Figure 1.26: Threads and points of thread-cutting screws.

Some application examples of self-drilling screws are shown in the Figure 1.27.

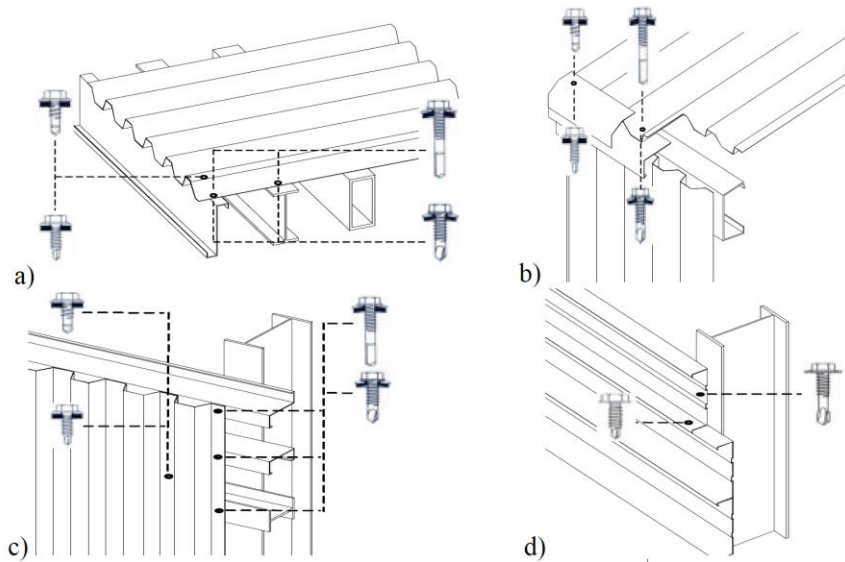


Figure 1.27: (a) fastenings of roof sheeting on purlins; (b) fastening of sheeting at an eave detail; (c) fastening of wall sheeting on side rails; (d) fastenings of wall cassettes on stanchions.

## 1.5 Applications

Cold-formed steel (CFS) was originally a product of the 19th century, but it began to gain mainstream recognition in 1946 with the publication of the first edition of the *AISI Specification for the Design of Cold-Formed Steel Structural Members*. Since then, CFS has continually evolved, leaving its mark on architecture by offering building owners innovative design options that were previously unattainable due to the lack of established design codes and standards [9].

Today, CFS stands as a critical material in modern construction, renowned for its precision, strength, and versatility. With its exceptional strength-to-weight ratio and dimensional accuracy, CFS is highly adaptable and reliable, making it a key choice for a wide range of structural and non-structural applications in residential, commercial, and industrial projects. As a sustainable building material, it supports innovative and efficient designs while meeting high standards for durability and environmental responsibility. In the following, we'll explore its diverse applications, highlighting its role in meeting the demands of today's construction needs [10].

CFS framing can add lightweight height to an existing building. A building that exemplifies this concept is the Piatt Place in Pittsburgh, Pennsylvania (Figure 1.28). The use of cold-formed steel (CFS) enabled us to significantly reduce the additional weight imposed on the foundation and footing, allowing the existing structural framing to remain in use. This approach not only preserved

the integrity of the original structure but also made the project economically viable by minimizing material and construction costs [10].



*Figure 1.28: Renovated Piatt Place [10].*

In the design of the seven-story Embassy Suites hotel in Columbus, Ohio, cold-formed steel (CFS) framing was used for both the interior and exterior load-bearing and non-load-bearing walls, and floor and roof joists. This distinctive structural design hinged upon CFS's strength. Thicker studs were used on the lower floors, while thinner studs were used on each subsequent, upper-level floor where the loads were lessened [10].

Victory Hall at the University of North Texas in Denton transitioned its structural design from concrete to cold-formed steel (CFS) framing. This change resulted in significant savings in material costs, labor, and construction time, enabling the project to remain on schedule and meet its targeted timeline efficiently [10].





*Figure 1.29: CFS-framed structure of Victory Hall at the University of North Texas [9].*

CFS trusses, including those made of proprietary shapes and C-studs, are made of light-gauge steel forms. They are pre-engineered with the help of software programs and can be customized into roof shapes and layouts for a variety of applications. They can also be prefabricated, which can reduce on-site labor and construction timelines [10].



*Figure 1.30: CFS truss [10].*

Compared to conventional framing systems, CFS trusses offer significant advantages [10];

- Faster shell completion time, enabling faster interior buildout
- Smaller-dimension trusses in lieu of beams and columns
- Flexibility in spatial layout and location of infrastructure elements
- Increased durability and resiliency because CFS is noncombustible

- Reduced installation time due to fewer pieces and lighter weight
- Easier, streamlined installation with reduced waste
- Resilient to termite damage and dry rot
- Components are customized and exact, without inconsistencies such as knots

CFS truss roof or floor systems can also be assembled on the ground and lifted onto the structure (called “rafting”) as shown below [10];



*Figure 1.31: Individual roof trusses [10].*



*Figure 1.32: Roof trusses are lifted into place, completing the steel framing of a Cantiro home in Edmonton [10].*



CFS trusses provide a reliable and efficient solution for long-span structures, balancing strength, durability, and sustainability while meeting the architectural and functional requirements of modern construction [10].



*Figure 1.33: steel floor trusses allow for long spans [9].*

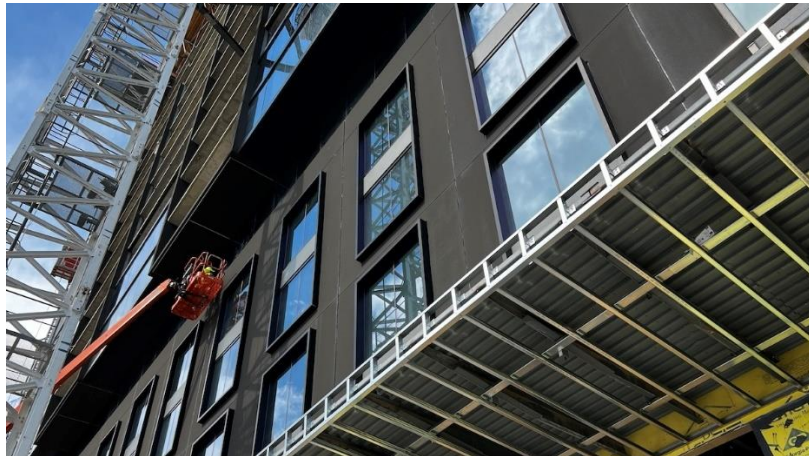
Engineers must account for factors such as wind loads, snow loads, and seismic forces when designing CFS trusses for long spans. Additionally, hybrid systems that combine CFS with hot-rolled steel may be used to optimize performance in extremely demanding applications [10].

#### Cold-Formed Steel (CFS) Studs;

CFS studs serve as a framing system for curtain walls in commercial buildings, supporting glass, aluminum, or other facade materials [10].

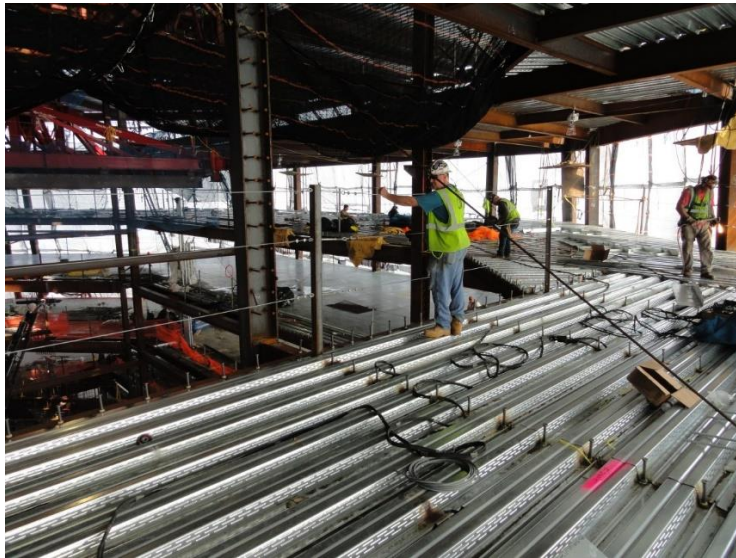


*Figure 1.34: Prefab CFS exterior panels [10].*



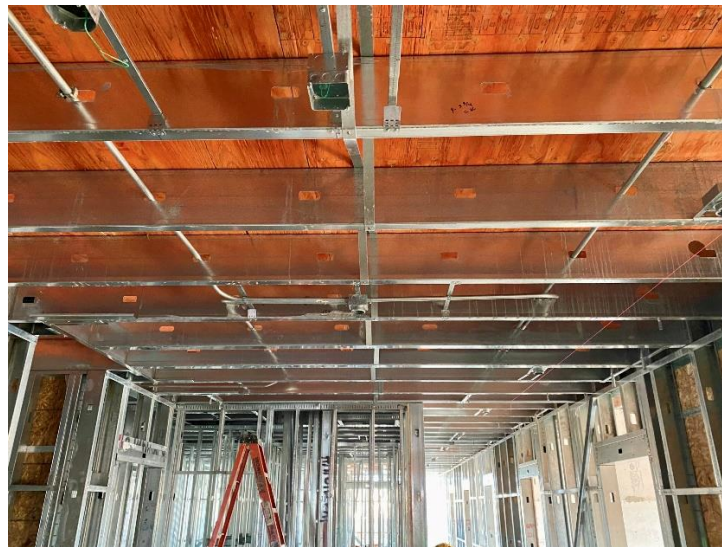
*Figure 1.35: Prefab's exterior finished panels [10].*

Decking Support: In multi-story construction, CFS studs provide a stable framework for concrete or composite decking [10].



*Figure 1.36: Cold-Formed Steel Deck [9].*

Joists and Rafters: CFS studs are used as lightweight, high-strength joists and rafters in roof and floor assemblies [10].



*Figure 1.37: The University of Hawaii Atherton Hall project features cold-formed steel (CFS) framing for a rehabilitation project [10].*



## Chapter 2. Literature Review

### 2.1 Cold Formed Steel Bolted Moment Frames

AISI S400-15 Chapter E4 is the design standard for CFS-SBMF (Cold Formed Steel-Special Bolted Moment Frames) systems. This type of one-story framing system features C-section beams connected to hollow structural section columns by bearing-type high-strength bolts and is commonly used in industrial platform construction. Example detailing of this system is shown in Figure 2.38 [12].

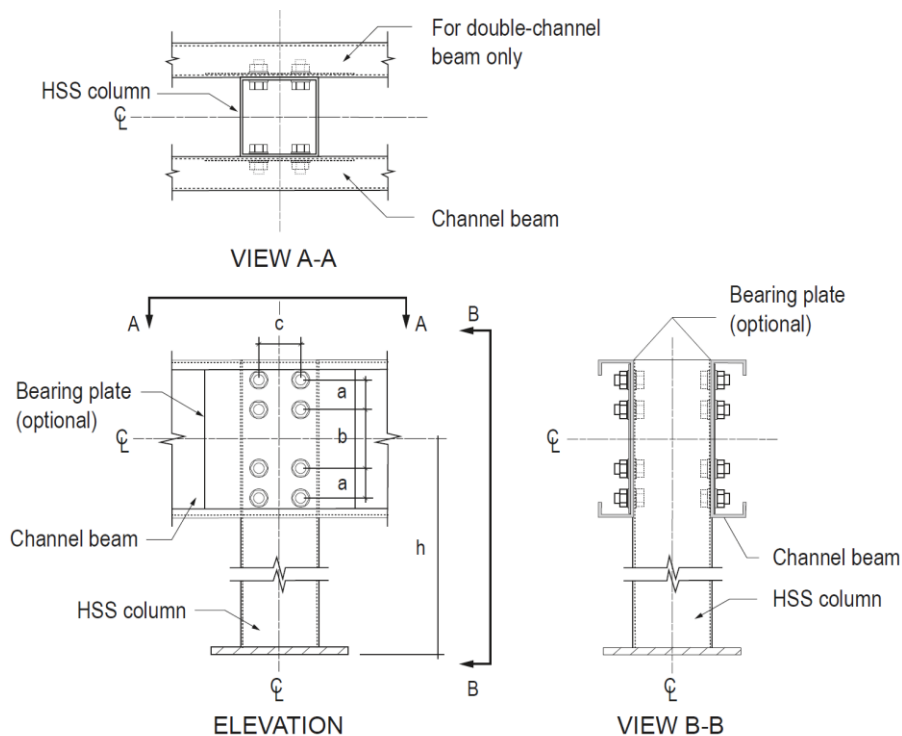


Figure 2.38: CFS-SBMF connections [12].

CFS-SBMFs withstand inelastic deformations through friction and bearing at their bolted connections. Beams, columns, and connections shall satisfy the requirements of S400-15 [11] and shall be limited to one-story structures no greater than 35 feet (10.7 m) in height [11,12].

The CFS-SBMF shall engage all columns supporting the roof or floor above. A single beam size and column with the same bolted moment connection detail shall be used for each frame. Because of these limitations this system is mostly used for industrial single-level mezzanines and cannot be used for multi-level construction. The advantage of this system is that the field construction is

fast and does not require welding. These systems lend themselves to uses that are repetitive and regular in column spacing [12].

The design of CFS-SBMFs require that connections be configured such that a ductile limit state in the connection, such as localized yielding around the fastener or bearing deformation, controls the available strength. Test results for this system show that specimens had an inter-story drift capacity significantly larger than 0.04 radians. The cyclic behavior was characterized by a linear response, a slip range, and a significant hardening response because of bearing at bolt holes [12].

The strong column-weak beam design philosophy associated with structural steel moment frames is not appropriate for this system. Rather than relying upon yielding of the frame beam, the CFS-SBMF relies on inelastic action through bolt slip and bearing in the connection as a ductile yielding mechanism. Beams and columns are protected to remain elastic by capacity design principles. Drift calculations should include not only deformations due to member deflections but also deformations in the connections. Connection stiffness can be modeled using empirical data available on tested assemblies or reasonable extrapolations of such data to account for connection geometry [12].

CFS seismic design does not have to imply 100 percent application of CFS. A number of integrated solutions show excellent possibilities. For example, consider a CFS-framed shear wall: to achieve higher capacity chord studs, well detailed hot-rolled HSS sections may replace the CFS chord studs. This replacement has already been used with success and shows excellent potential in the right situation. This solution may potentially be investigated as a formal CFS framing SFRS. Concrete composite construction possibilities also exist for CFS-framed shear walls. Investigations of this type have not been common in North America but are popular in research performed in some other countries (e.g., Feng et al. 2010) [12].

In multi-story construction, an efficient system may use reinforced concrete or masonry walls around the elevator or stair cores with all remaining wall and floor framing completed with CFS. The LFRS would be a mixture of an existing CFS SFRS system and the elevator/stair core systems. Such mixed or dual systems are allowed in ASCE 7 today, but efficient performance and connection details are largely uninvestigated. These integrated systems have the potential to improve the economy of this form of construction [12].

A common energy dissipating mechanism in CFS SFRS is related to bearing and damage at fastener locations. These may be steel-to-steel, wood-to-steel, or other material-to-steel connections. Details vary across a wide range of steel thickness, fastener and head size, and configuration [12].

Fundamental to the behavior of thin-walled cold-formed steel members are the stiffness reductions that may occur because of local, distortional, and global buckling under load. These reductions must be captured within designs and models if the full system created by cold-formed steel members is to be assessed. Using existing test data, a new method was developed for determining the stiffness reduction and backbone moment-rotation and/or moment-curvature response under local and distortional buckling (Ayhan and Schafer 2012). Recent testing with carefully selected members and boundary conditions for the study of local, distortional, and global cyclic response of cold-formed steel members loaded axially (Padilla-Llano et al. 2014) and flexurally (Padilla-Llano et al. 2016) have also been completed. The results highlight the energy dissipation capabilities and post-buckling strength and stiffness of CFS members. These results can form the basis for development of seismic force-resisting systems that incorporate complete cold-formed steel member response, as opposed to current systems that largely seek to use alternative mechanisms to resist seismic demands independently from the members, such as bearing in wood or steel connections, or yielding of straps [12].

In a study conducted by a group of researchers in 2011, a new approach was introduced to enhance the ductile capacity of cold-formed steel (CFS) beams, allowing seismic energy to be dissipated by the beams rather than relying on the limited ductile capacity of CFS frame joints. As earthquake-resistant design primarily requires the ductility of moment-resisting frames (MRFs) to be provided by the beams, while columns and connection elements are expected to remain elastic, it became evident that improving the ductility of CFS beams was crucial for their application in seismic regions [13].

To address this challenge, the study carried out an analytical investigation aimed at delaying local failures in both CFS beam and column sections, as well as enhancing the ductility, strength, and



stiffness of CFS beam–column connections. The study then proposed new forms of CFS beam–column moment-resisting connections, which are presented in the following [13].

Furthermore, the use of curved elements was considered a significant advancement in the stiffening of thin plate elements. Specifically, the width-to-thickness ratios were reduced by shortening the flat portion of the flange, as illustrated in Figure 2.39 [13].

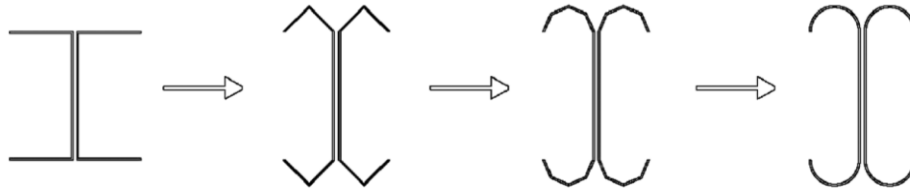


Figure 2.39: Stiffening evolution of flat elements toward curved elements [13].

The bent elements were found to support each other by generating in-plane stiffness when out-of-plane deformations (local buckling) occurred. This arching action effectively delayed local buckling, thereby enhancing the overall stability of the structure. Moreover, Curved flange beam sections provide several advantages over flat flange sections.

In addition to increased buckling strength, they exhibit higher ductility due to the reduction in cold work effects during the forming process, as sharper corners in flat flange sections tend to increase cold work effects. Moreover, curved flange sections generally demonstrate enhanced bending strength, including both the plastic moment ( $M_p$ ) and the yielding moment ( $M_y$ ), even for sections with the same cross-sectional area. This improvement in bending strength is observed across most curved flange angles, even without considering local buckling effects.

The diamond column sections (Fig. 2.40(a)) were selected for the beam–column connections to generate in-plane bending moment action in the column walls, thereby providing resistance against potential out-of-plane forces exerted by the beams, as illustrated in Fig. 2.41.

In the bolted beam–column connections (Fig. 2.40(b)), the bolts were required to provide a sufficient lever arm to withstand the bending moments transferred from the beams to the lips of the columns. To ensure structural integrity and enhanced performance, the connection was designed with specific objectives. It was engineered to integrate all faces of the columns and beams, ensuring in-plane action in the columns rather than the forces normal to their faces, which are typically observed in conventional beam–column connections. Additionally, the

design strengthens the beams near the column faces, effectively shifting potential plastic hinges away from that region—an approach widely adopted for post-Northridge moment-resisting frame (MRF) connections. Furthermore, panel zone actions are resisted using through plates inside the columns, eliminating the need for stiffeners and continuity plates that are commonly required in traditional MRF connections.

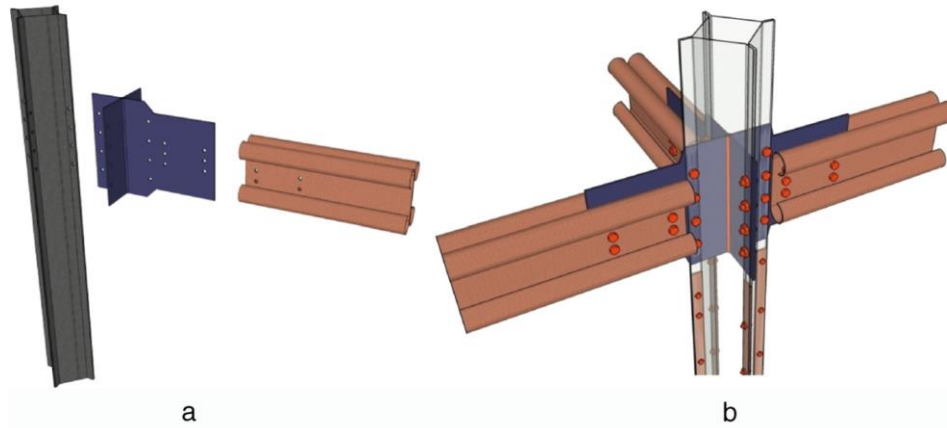


Figure 2.40: CFS beam–column connections: (a) Diamond column, cross through plates and curved flange beam. (b) Assembled moment resistant connections [13].

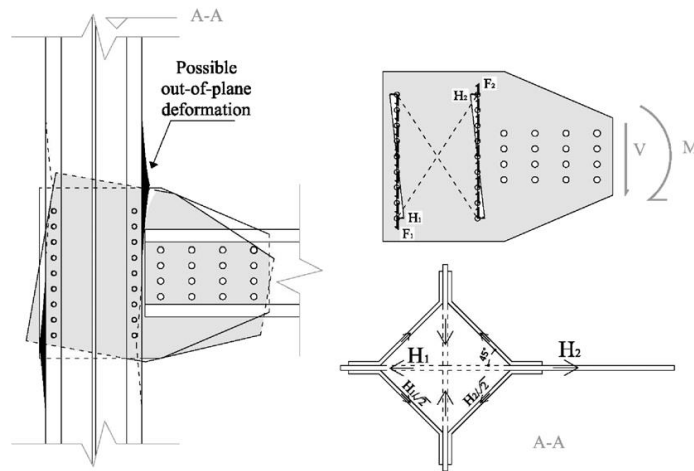


Figure 2.41: In-plane action of the column walls with through plate connection [13].

Increasing the bolt-group length cannot always be efficient for MR beam-to-column connections since it increases the moment demand on the column. Moreover, this approach can make frame erection more difficult. Therefore, the effect of different configurations of out-of-plane stiffeners were examined on postponing the premature web buckling of the beam (Fig. 2.42). These included stiffening the flanges in the connection region by horizontal plates and angles, stiffening the webs

by long horizontal plates and vertical plates tied to the webs and finally a combination of vertical plates tied to entire section and horizontal plates between them.

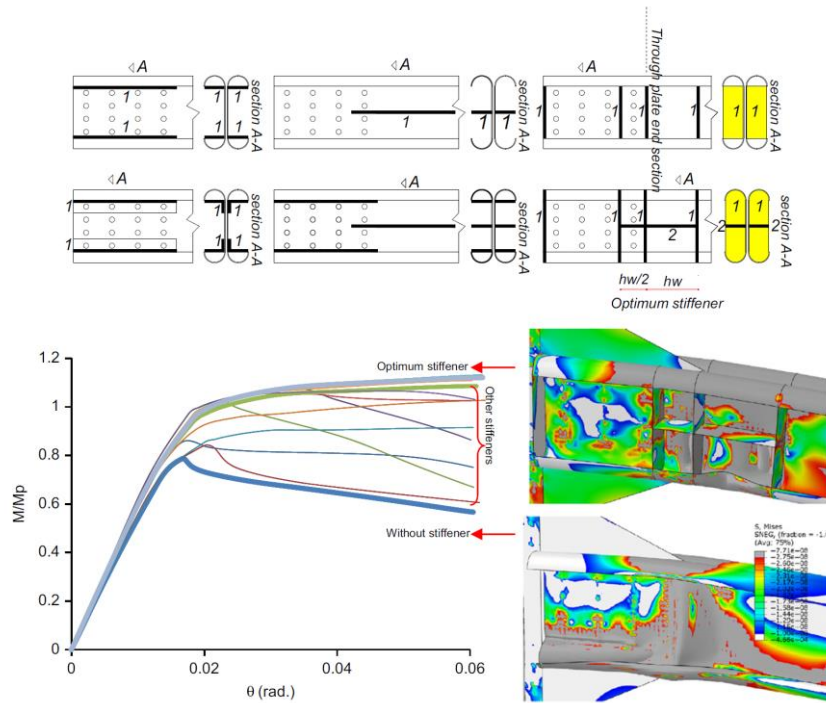


Figure 2.42: Different out-of-plane stiffener configurations for the CFS beam–column connections,  $M$ – $\theta$  curves and local buckling deformation of beam without stiffener and beam with optimum stiffener.

The moment–rotation curve of the best of the examined connections (see Fig. 2.42, optimum stiffener) showed a significant increase in both strength (40%) and ductility (100%) in comparison with the connection without stiffeners (Fig. 42). The optimum stiffener configuration delayed the local buckling in the web thus maintaining the flange stiffness and postponing the web-flange local buckling interaction.

In this Study, two types of analyses had been performed for beam sections [13]:

- Nonlinear elastic buckling analysis using linear perturbation procedure BUCKLE to capture modal buckling loads and shapes.
- Nonlinear inelastic post-buckling analysis using the standard RIKS arc-length method, which takes into account stiffness softening due to buckling.

The finite element analysis (FEA) of the proposed moment-resisting connections revealed that cold-formed sections possess sufficient energy dissipation capacity, a crucial factor in the seismic design of moment-resisting frames (MRFs). However, this capability was dependent on the use of appropriate beam sections, such as curved flange sections, which effectively mitigated width/thickness ratio limitations and delayed local buckling failures. Additionally, through-plate connections between cold-formed beams and columns demonstrated adequate strength and ductility, provided they were properly detailed and stiffened. This detailing ensured the formation of plasticity in the beams, thereby improving the overall seismic performance and resilience of the frame [13].

As far as the development of thin-walled cold-formed steel (CFS) sections as energy-dissipative elements for seismic moment-resisting multi-storey frame buildings was concerned, it was investigated through Finite Element (FE) analysis and experimental work. Studies were conducted at two structural levels: individual elements and beam-column connection, aiming to evaluate the performance, ductility, and strength of CFS sections under seismic conditions [14].

At the element level, various CFS beam designs were analyzed to enhance their seismic performance. The research showed that increasing the number of flange bends improved both the elastic and inelastic behavior of beams. Beams with curved flanges, which were designed to have an infinite number of bends, exhibited the highest strength, stiffness, and ductility (figure 2.43). This improvement was attributed to the arching action of the bent flange elements, which helped delay local buckling and increase the overall resilience of the structure.

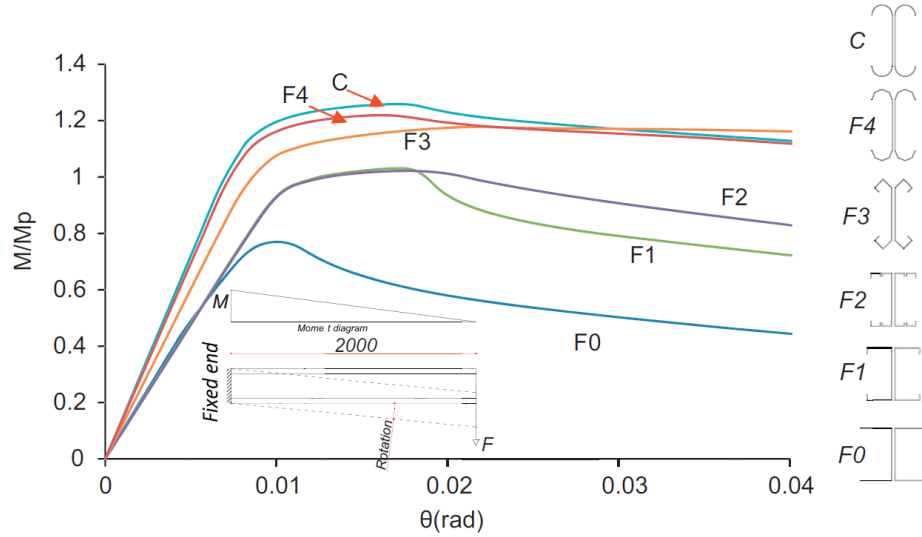


Figure 2.43 :Moment–rotation curves of the beams.

At the beam-to-column connection level, analytical and experimental investigations conducted in 2012 further explored different configurations of CFS beam-to-column connections using through plates, employing numerical analysis and experimental verification to assess their effectiveness in the development of thin-walled CFS sections as energy-dissipative elements for moment-resisting multi-storey buildings in seismic regions [14].

The beam-to-column connection configurations of the test Specimens A1, A2 and A3 used in the experimental investigation are presented in Table 2.1.

Table 4: The specimens configurations [14].

| Specimens | Connection stiffeners        | Connection type |
|-----------|------------------------------|-----------------|
| A1        | Without stiffeners           | Slip-critical   |
| A2        | Partial (minimum) stiffeners | Slip-critical   |
| A3        | Full (optimum) stiffeners    | Slip-critical   |

The connection with full set of stiffeners (used for Specimen A3) was the configuration that provided the highest resistance and ductility in the FE simulations (optimum stiffener) and the connection with partial stiffeners (used for Specimen A2) was the configuration with the minimum stiffeners. The connection without stiffeners (Specimen A1) was used for benchmarking and comparison purposes.

Numerical simulations revealed that conventional web-bolted connections without out-of-plane stiffeners suffered from premature web buckling, leading to an early loss of strength. To counteract this, a minimum of two pairs of vertical stiffeners were incorporated into the connection region. These stiffeners effectively delayed web and flange buckling, thereby increasing moment strength and ductility. The investigation was further supported by experimental beam-to-column connection tests, which verified the numerical predictions.

Experimental tests demonstrated that the use of the minimum (partial) and the optimum (full) configuration of out-of-plane stiffeners for the beams in the connections improved the moment strength by 28% and 35%, the ductility by 50% and 75% and the hysteretic energy dissipation capacity by 30% and 90%, respectively, compared with the connection without stiffeners.

FE analysis at the connection level further validated these findings. The moment-rotation ( $M-\theta$ ) behavior and local buckling deformations obtained in the tests showed good agreement with numerical predictions. However, for more precise modeling, adjustments incorporating actual specimen dimensions, imperfections in the beams, material properties from tensile tests, and connection slip-bearing actions under cyclic loading were suggested.

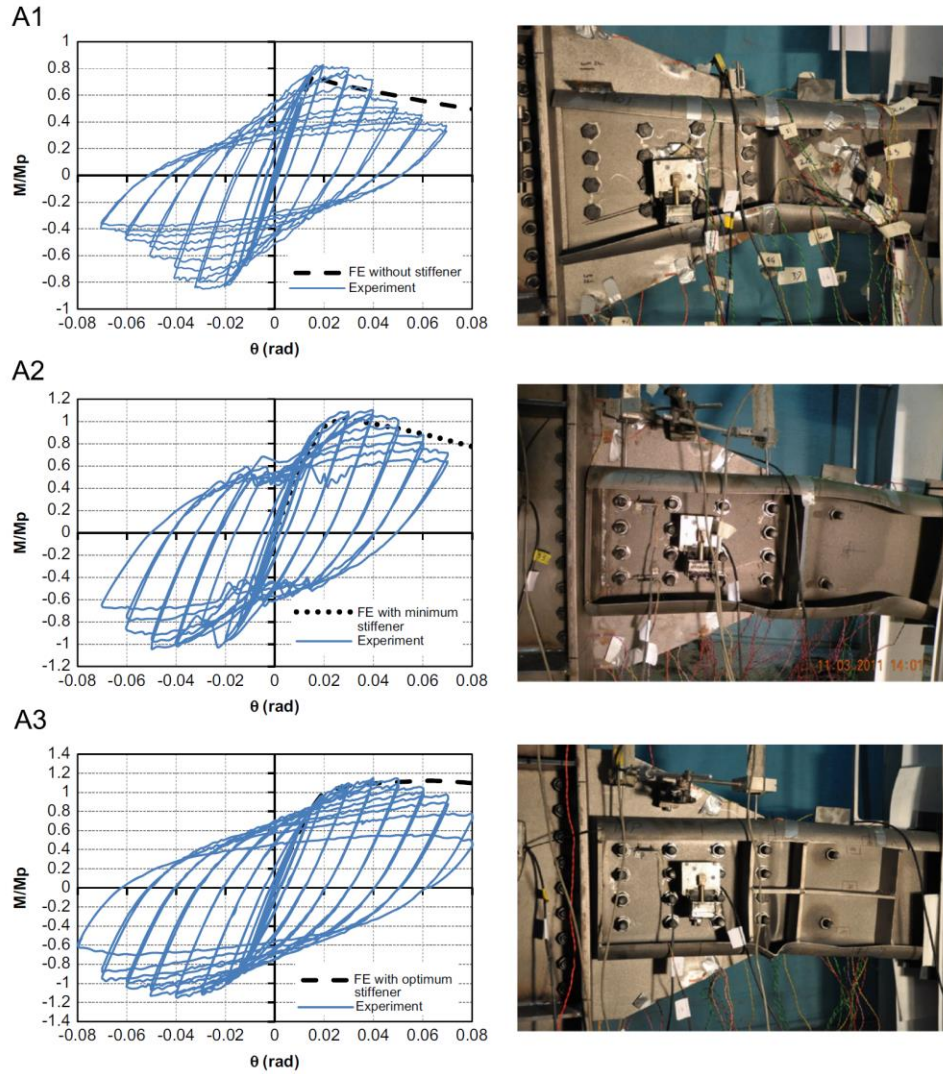


Figure 2.44 :  $M/M_p - \theta$  hysteretic curves and local buckling deformation of Specimens A1-3  
And envelope  $M/M_p - \theta$  curves of FE predictions.

The research demonstrates that thin-walled cold-formed steel (CFS) elements can serve as effective dissipative components in moment frames for highly seismic regions. This investigation was conducted at two structural levels: the element level, focusing on the performance of individual CFS members, and the connection level, evaluating their integration and effectiveness in moment-resisting connections.

The research underscored the importance of optimizing CFS beams and their connections to enhance their earthquake resistance. The findings demonstrated that properly designed CFS elements could function as dissipative components in seismic regions. The integration of stiffeners



into beam-column connections significantly improved strength, ductility, and energy dissipation, making CFS moment frames a viable alternative for earthquake-resistant structures.

The study concluded that cold-formed steel could be effectively utilized in seismic design if proper measures were taken to improve ductility and prevent premature local buckling, contributing to the advancement of CFS structures in seismic engineering and offering innovative solutions for multi-storey buildings in earthquake-prone areas.

In another study in 2012, The experimentation focused on the investigation of the concept of CFS thin-walled curved flange sections as seismic energy dissipative elements for moment frame multi-story buildings using full and minimum sets of out-of-plane stiffeners. It also aims to examine if curved flange CFS sections can produce full plastic moment ( $M_p$ ) sustained at large rotations similar to Class 1 cross sections in Eurocode 3 and larger than 0.04 rad required for special moment frames in AISC Seismic Provision. The tests were performed on six bolted beam-to-column connections, divided in two specimen types with different thickness (A) 3 mm, and (B) 4 mm, with three different out-of-plane stiffener configurations (in the connection region) (A1, A2, A3, and B1, B2, B3) were used in the experimental investigation (Table 1) [15].

*Table 5: The specimens configurations [15]*

| Specimens | Beam thickness (mm) | Connection stiffeners        | Connection type |
|-----------|---------------------|------------------------------|-----------------|
| A1        | 3                   | No stiffeners                | Slip-critical   |
| A2        | 3                   | Partial (minimum) stiffeners | Slip-critical   |
| A3        | 3                   | Full (optimum) stiffeners    | Slip-critical   |
| B1        | 4                   | No stiffeners                | Slip-critical   |
| B2        | 4                   | Partial (minimum) stiffeners | Slip-critical   |
| B3        | 4                   | Full (optimum) stiffeners    | Slip-critical   |

The experimental setup employed a reaction frame with notable components designed to support realistic loading conditions. Instruments such as strain gauges, inclinometers, and Linear Variable Differential Transformers (LVDTs) were strategically placed to measure displacements, rotations, and strain at critical locations throughout the tests (figure 2.2) [15].



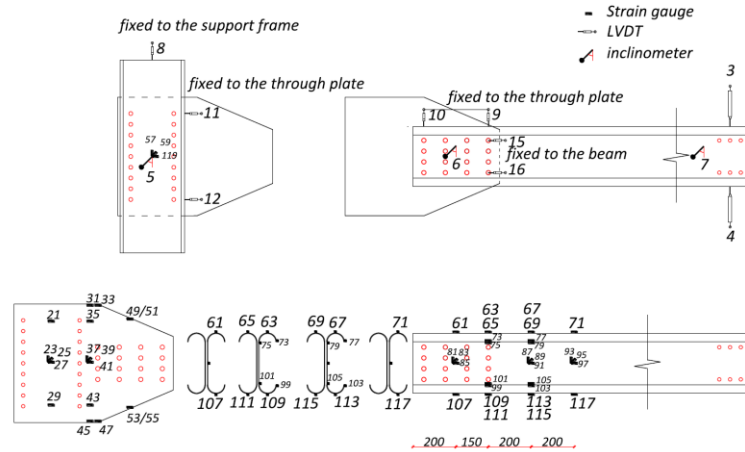


Figure 2.45: Instrumentation sketches of the specimens [15].

The test results demonstrated that vertical and horizontal stiffeners effectively restrained web and flange buckling, preventing local buckling deformations and ensuring stable connection behavior. Maximum recorded rotations reached 0.005 rad without sudden slip, confirming the connection's stability. Specimens equipped with stiffeners exhibited significant improvements in hysteretic performance, with ductility increasing by up to 75%, moment capacity enhanced by 35%, and hysteretic energy dissipation capacity improving by up to 240%. The hysteretic response remained stable, as plastic strains were delayed until large rotations mobilized bearing actions in the connections. In terms of buckling behavior, Specimen B1 experienced web buckling at 0.05 rad, progressing to failure through extensive web and flange buckling at 0.08 rad. Strain distributions confirmed localized buckling failures in critical sections. Slip resistance calculations, based on pretensioning forces, indicated that Specimen A exceeded expectations, while Specimen B approached the required resistance limits. Instrumentation insights from strain gauges revealed a clear correlation between strain and rotation, highlighting the occurrence of plastic strain locking due to extensive flange buckling. The study emphasized the crucial role of connection design in enhancing the seismic resilience of cold-formed steel structures. The use of stiffeners significantly affects the overall behavior, contributing to improved ductility, strength, and energy dissipation. The findings indicate that appropriately designed CFS connections can be effectively utilized in earthquake-prone areas. The results also demonstrate the importance of understanding the interaction between various types of buckling and their impact on structural integrity during seismic events [15].

Another study conducted by the same research group in 2013 further investigated the cyclic moment connection behavior of Cold-formed steel (CFS), particularly in seismic applications. This research presented a comprehensive analysis of bolted moment connections under cyclic loading conditions. Specifically, it focused on finite element (FE) modeling while incorporating the effects of connection slip [16]. As a result, it provided a deeper understanding of moment-rotation behavior and failure mechanisms, ultimately contributing to improvements in seismic performance and structural resilience.

The authors utilized an extensive finite element (FE) modeling approach with ABAQUS software to simulate the hysteretic behavior of bolted cold-formed steel (CFS) moment connections under cyclic loading. A key aspect of the methodology was the simulation of bolt slip, which introduced nonlinearities in the moment-rotation response, requiring advanced modeling techniques. Two approaches were explored: a detailed model incorporating bolt geometry and frictional resistance and a simplified model using connector elements to approximate slip behavior, enhancing computational efficiency for cyclic analysis. A major contribution of the study was the development of a simplified cyclic slip model with reduced slip resistance load, which effectively captured the hysteretic response of connections dominated by bolt slip while maintaining computational efficiency. Additionally, the modeling incorporated geometrical imperfections typical of CFS components and material properties obtained from tensile coupon tests, ensuring that the simulations closely mirrored the actual behavior of structural elements. Then results from the FE models were validated against experimental data, confirming the accuracy of the simulations. By analyzing both experimental and finite element (FE) simulation results, the study identified two distinct categories of specimens based on their dominant response mechanisms. The first category included specimens governed by beam flexural deformations (A1–A3, B1), where plastic deformations primarily occurred within the beams, with only minor contributions from bolt slip. The FE models accurately replicated the moment-rotation response and failure modes observed in experiments, though slight discrepancies arose due to the exclusion of localized slip within the simplified models. The second category comprised specimens governed by connection slip (B2, B3), where significant slip at the bolt interfaces influenced the overall moment-rotation behavior. The FE models incorporating slip-bearing actions closely matched experimental results,

though minor deviations were attributed to unmodeled hole elongations and material uncertainties [16].

An important factor in the study was the necessity of implementing a modification factor ( $\alpha$ ) to account for the stabilizing effects of reduced slip resistance, which was observed experimentally. This factor proved essential in improving the correlation between FE simulations and test data, particularly for connections experiencing pronounced bolt slip (figure 2.46).

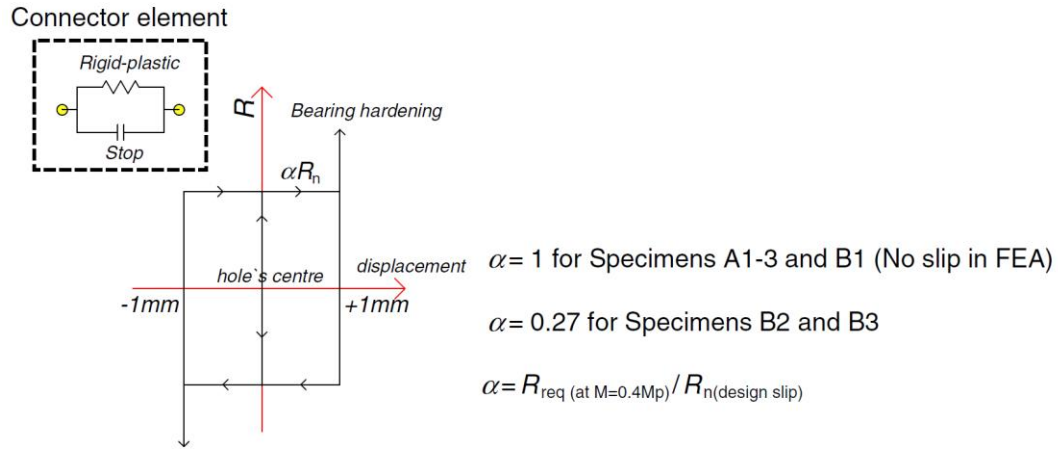


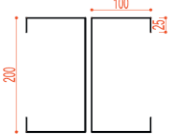

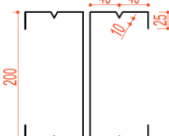

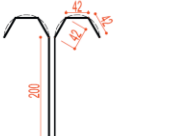

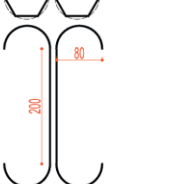
Figure 2.46: Simplified FE model for slip-bearing action of the bolts.

The research provided key insights into the cyclic behavior of bolted cold-formed steel (CFS) moment connections. The moment-rotation behavior analysis revealed that beam-deformation-dominated connections exhibited a linear response until failure, while slip-dominated connections displayed nonlinear behavior, significantly impacting load-carrying capacity. Slip initiation was observed at approximately 40% of the nominal plastic moment, after which the moment-rotation response deviated from linearity, demonstrating enhanced energy dissipation and delaying overall connection failure. The study's updated FE models accurately captured nonlinear hysteretic behavior and failure deformations, successfully predicting both stable and unstable slip phases, emphasizing the importance of incorporating slip effects in design and analysis. Moreover, the findings confirmed that slip-capable connections effectively dissipate seismic energy, a critical characteristic for structures in earthquake-prone regions, reducing the risk of premature failure during seismic events [16].

The findings from this study have significant design implications for cold-formed steel (CFS) connections. It is recommended that design guidelines explicitly incorporate connection slip considerations, ensuring that design methods account for slip resistance and the nonlinear behavior observed under cyclic loading conditions. Additionally, recognizing the role of slip in seismic energy dissipation enables the development of more resilient structures, enhancing their performance against seismic forces. This improved understanding contributes to better performance predictions and increased structural safety, making it a crucial factor in the seismic design of CFS moment connections. In summary, this study provided valuable insights into the cyclic behavior of bolted cold-formed steel moment connections. Through detailed finite element modeling and experimental validation, significant relationships between slip behavior, moment-rotation characteristics, and energy dissipation were established. This work contributed to the growing body of knowledge aimed at improving the resilience of CFS structures against seismic events. By emphasizing the need to account for slip in design practices, the study prompts structural engineers to adopt more sophisticated approaches to ensure the safety and efficacy of CFS connections [16].

A study conducted in 2019 by a group of researchers aimed to evaluate the seismic performance of CFS bolted beam-to-column connections equipped with a friction-slip mechanism. The intent was to identify effective design configurations through extensive analytical studies and finite element modeling. Finite Element (FE) models validated through experiment were developed in ABAQUS to simulate the hysteretic behavior of CFS connections. The study methodically varied bolt configurations, cross-sectional shapes, and slip resistance to analyze their influence on key performance indicators such as moment capacity, energy dissipation, damping coefficient, and ductility [17].

Table 6: Different channel types and bolt configurations [17].

| Channel type     |   | Bolt configuration |   |
|------------------|---|--------------------|---|
| Flat-flange      |  | Square             |  |
| Stiffened-flange |  | Diamond            |  |
| Folded-flange    |  | Circle             |  |
| Curved-flange    |  |                    |   |

The results of the study highlighted the significant impact of the bolting friction-slip mechanism on the hysteretic behavior of cold-formed steel (CFS) moment connections. The incorporation of this mechanism altered the moment-rotation response, effectively reducing stress concentrations and delaying failure. Connections utilizing the friction-slip mechanism exhibited substantial improvements in energy dissipation capacity, with increases of up to 200% for class 3–4 CFS beam cross-sections and 50% for class 1–2. The influence of bolt configuration was also notable, as the conventional square bolt arrangement resulted in up to 25% higher energy dissipation in class 3–4 beams, while the diamond bolt configuration provided up to 70% higher dissipation for class 1–2 elements. Furthermore, the cross-sectional shape played a crucial role, with stiffened-flange and folded-flange sections demonstrating the highest energy dissipation capacity, regardless of whether the friction-slip mechanism was incorporated [17].

The findings underscored the importance of selecting appropriate design parameters in enhancing seismic performance. The friction-slip mechanism acted as a critical design choice that transformed the behavior of CFS connections under cyclic loading, making them more resilient in seismic events. Despite the promising results, it was noted that conventional CFS bolted moment connections often did not meet the AISC requirements for intermediate and special moment

frames, emphasizing the necessity for optimized configurations that exploited the advantages of friction-slip mechanisms [17].

Furthermore, the research validated the effectiveness of friction-slip mechanisms in improving energy dissipation and overall ductility of CFS bolted connections. This study contributed to the development of more efficient and resilient design solutions for CFS frames in seismic-prone areas, which were essential for enhancing the structural integrity and safety of buildings [17].

In 2020, To improve the seismic performance of CFS bolted-moment connections, a study conducted a parametric analysis using an experimentally validated finite element (FE) model developed in ABAQUS. The model accounted for material nonlinearity, geometrical imperfections, and bolt-bearing behavior. The study aimed to identify optimal design parameters, such as bolt arrangement, cross-sectional shape, and gusset plate thickness, to enhance the ductility and energy dissipation capacity of CFS connections [18].

The FE model had been developed to simulate the cyclic behavior of CFS bolted connections. It utilized a connector element to model the bearing behavior of bolts against steel plates (figure 2.47). The study incorporated geometrical imperfections based on experimental data and applied cyclic loading following the AISC 341-16 standard. Validation against experimental results confirmed the accuracy of the FE model, as it successfully replicated the moment-rotation hysteresis behavior and failure modes observed in physical tests [18].

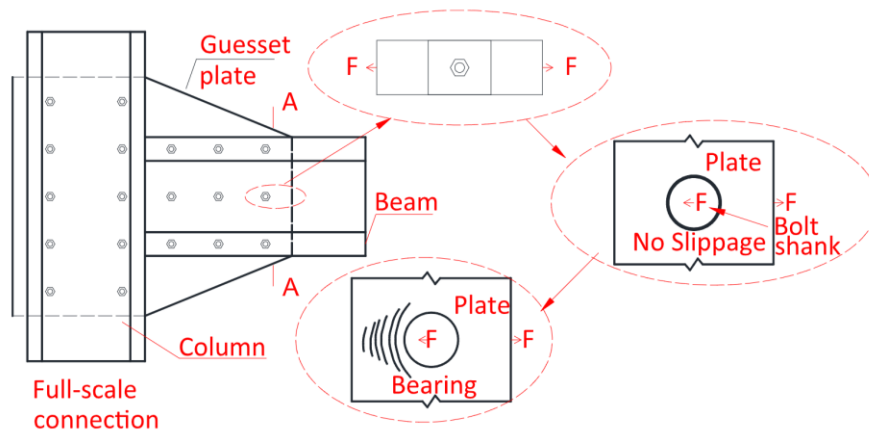


Figure 2.47: Bearing behavior of a single bolt against steel plate used in CFS bolted-moment connection [18].

The study examined four different cross-sectional geometries; flat-flange, stiffened-flat, folded-flange, and curved-flange sections (figure 2.48), to evaluate their structural performance. Among these, folded-flange sections exhibited the highest ductility, surpassing flat sections by up to 55%. Curved-flange sections were found to effectively delay local buckling, though they posed manufacturing challenges. Additionally, the findings indicated that the moment capacity of connections was more significantly influenced by bolt arrangement and beam slenderness than by the cross-sectional shape itself.

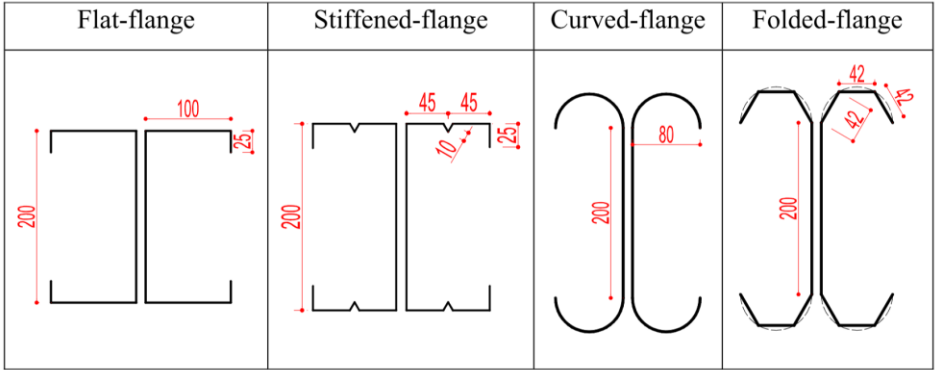


Figure 2.48: Details of the back-to-back beam cross-sectional dimensions (in mm),  $L = 2000\text{ mm}$ .

The study analyzed three bolt configurations; square, diamond, and circular arrangements (figure 2.49), to assess their impact on moment capacity, ductility, and energy dissipation. The square bolt arrangement provided the highest moment capacity, increasing it by up to 32%. In contrast, the diamond and circular configurations significantly enhanced ductility (up to 100%) and energy dissipation (up to 250%), demonstrating superior performance in cyclic loading conditions. However, the optimal bolt configuration depended on the cross-sectional classification of the cold-formed steel (CFS) beam, highlighting the importance of tailored connection detailing for structural efficiency.

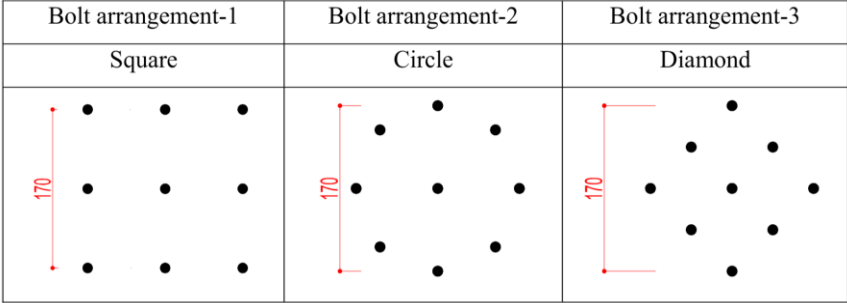


Figure 2.49: Different bolt arrangements.

The study classified sections based on Eurocode 3 standards (figure 2.50) and identified significant differences in their structural performance. Class 1 and 2 sections, characterized by lower slenderness, demonstrated superior ductility and energy dissipation, making them well-suited for seismic applications. In contrast, Class 3 and 4 sections, which have higher slenderness, were prone to premature local buckling, rendering them unsuitable for seismic conditions. Additionally, connections with Class 1 sections exhibited up to three times higher plastic rotation capacity, highlighting their enhanced ability to undergo large deformations without failure.

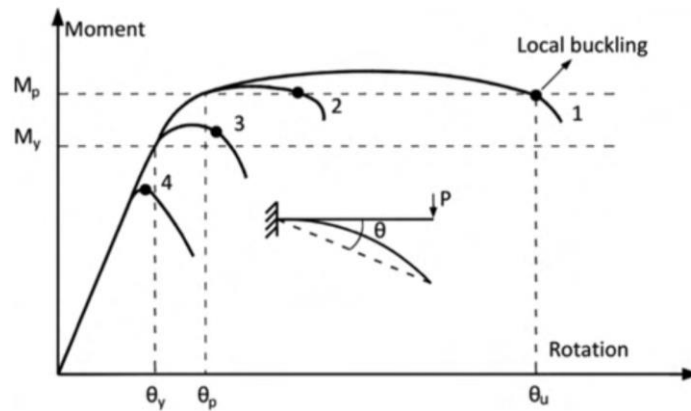


Figure 2.50: Cross-sectional classification based on moment-rotation curves.

The study highlighted the critical role of gusset plate thickness in connection performance. When gusset plates were thinner than or equal to the CFS beam thickness, premature failure occurred in the gusset plate. However, slightly increasing the gusset plate thickness helped prevent early failure and enhanced moment capacity. Regarding seismic suitability, the study evaluated CFS bolted-moment connections based on AISC requirements, finding that connections with Class 1 and 2 beam sections met the criteria for Special Moment Frames (SMFs), while Class 4 beam sections were deemed unsuitable for seismic applications. Additionally, the study introduced an energy-based FEMA bilinear model to characterize the cyclic behavior of connections.

In terms of damping and energy dissipation, the equivalent viscous damping coefficient was found to be highest in connections with Class 1 and 2 beams. Folded flange beam sections exhibited up to 250% higher energy dissipation compared to conventional flat sections, demonstrating their superior seismic performance. Moreover, the use of circular and diamond



bolt configurations significantly improved damping performance, particularly in connections with lower slenderness ratios.

In conclusion, the research established foundational insights into the design of CFS bolted-moment connections, particularly emphasizing the benefits of using folded flange shapes and innovative bolt arrangements. By addressing critical design factors such as cross-section classification, gusset plate thickness, and damping characteristics, the study provided significant contributions to the field of earthquake-resistant construction. The findings highlighted the potential for optimizing CFS connections, thereby enhancing safety and performance in seismic-prone areas [18].

As traditional Web-Connected (W-C) bolted connections often suffered from premature local buckling due to thin-walled sections, reducing their seismic resilience, two new connection configurations—Flange-Connected (F-C) and Web-and-Flange-Connected (WF-C)—were developed and evaluated in a research work in 2022. These configurations improved load transfer mechanisms by engaging both flanges and webs. Optimized seismic design recommendations were proposed through Finite Element (FE) modeling and parametric studies. In this study, Finite Element Modeling (FE) in ABAQUS was conducted, incorporating nonlinear stress-strain relationships to define material properties. Geometric imperfections were considered to account for local and distortional buckling effects. The discrete fastener method was used for bolt modeling, capturing both bearing and friction interactions. Boundary conditions were set by restraining column bases and providing beam lateral bracing to replicate seismic conditions. Experimental validation was performed by comparing results from cyclic loading tests on W-C connections with FE simulations. A good correlation was found in terms of moment capacity, stiffness, and failure modes. The primary failure mode observed was local buckling of the beam near the gusset plate [19].

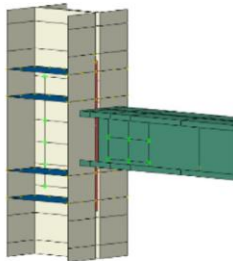
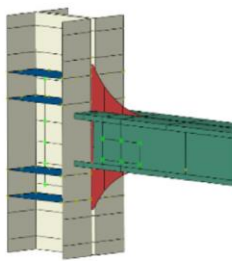
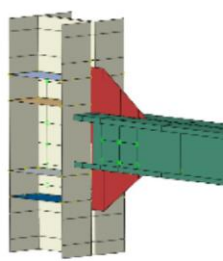
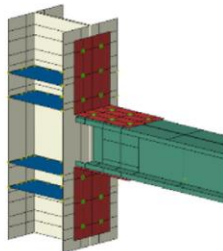
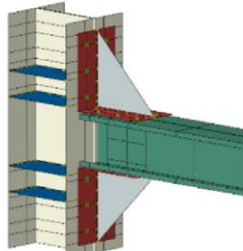
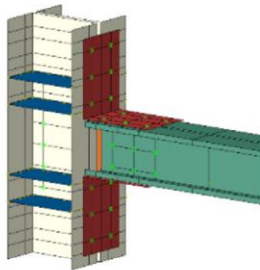
Web-Connected (W-C) connections (table 7) were analyzed with different gusset plate shapes, including T-shaped plates, which caused abrupt transitions and stress concentrations, rounded T-shaped plates, which improved stress distribution, and chamfered plates, which demonstrated the best performance. Findings indicated that chamfered and rounded T-shaped plates provided higher moment resistance and ductility. Thin gusset plates failed prematurely, while thicker plates improved overall performance. According to Eurocode 3 (EC3), connections were classified as either Semi-Rigid (S-R) or Rigid (R). Beams with a thickness

of  $\leq 2$  mm were generally categorized as Semi-Rigid, whereas thicker beams ( $\geq 4$  mm) resulted in Rigid connections [19].

Flange-Connected (F-C) connections (table 7) were developed using top and seat angles, either stiffened or unstiffened. Unstiffened angles acted as pin connections, making them unsuitable for seismic applications, while stiffened angles improved rigidity and met Special Moment Frame (SMF) requirements when designed with adequate thickness. Performance evaluations showed that for Class 3 and 4 beams, using angles with four times the beam thickness provided the best balance of strength, stiffness, and ductility, whereas for Class 1 and 2 beams, angles with twice the beam thickness were optimal [19].

Web-and-Flange-Connected (WF-C) connections (table 7) combined a T-shaped gusset plate with unstiffened angles, ensuring more uniform load transfer than W-C or F-C connections. These configurations shifted failure modes from beam buckling to gusset plate yielding, which enhanced energy dissipation. Performance assessments revealed that for all beam classes, gusset plates with twice the beam thickness provided high ductility and moment capacity. Additionally, these connections developed over 90% of the beam's flexural capacity [19].

Table 7: 3D graphical representations of different connection types [19].

| Web-connected (W-C)   |   |   |
|---|---|---|
| T-shape   | Rounded T-shape   | Chamfered shape   |
|    |    |  |
| Flange-connected (F-C)  |   |   |
| Unstiffened top and seat angles   | Stiffened top and seat angles   |   |
|    |  |   |
| Web and flange-connected (WF-C)   |   |   |
| T-shaped gusset plate and unstiffened top and seat angles                           |   |   |
|  |   |   |

The seismic performance of different connection types was evaluated through cyclic behavior analysis, where hysteretic moment–rotation curves revealed that W-C connections experienced abrupt stiffness degradation after reaching peak moment, F-C connections exhibited softening before ultimate rotation, and WF-C connections maintained stable hysteretic behavior, making them ideal for seismic applications. Ductility assessments showed that WF-C and F-C connections provided higher ductility than W-C connections, particularly for Class 3 and 4 beams. In terms of energy dissipation, WF-C connections performed best due to the interaction between the web and flange, while W-C connections suffered from early local buckling, limiting their energy absorption [19].

Based on the findings, design recommendations were proposed for seismic applications. W-C connections with rounded T-shaped gusset plates were deemed suitable for low to moderate seismic regions, while WF-C and well-designed F-C connections were recommended for high-seismic regions. F-C connections with thick stiffened angles improved rigidity but reduced rotational capacity, whereas WF-C connections offered the best balance of strength, stiffness, and seismic performance [19].

This study demonstrated that WF-C and F-C configurations significantly enhanced moment capacity, ductility, and energy dissipation in cold-formed steel (CFS) moment-resisting connections. WF-C connections outperformed both W-C and F-C connections in seismic conditions [19].

## Chapter 3. Methodology

### 3.1 Introduction

Due to the time-consuming and costly nature of experimental studies on the behavior of bolted cold-formed steel (CFS) moment connections, numerical methods serve as a suitable alternative for predicting the behavior of these structures. The finite element method, compared to experimental methods, offers additional advantages, including access to more unknowns in terms of stresses, deformations, and required curves. Furthermore, its superiority over other numerical methods lies in the fact that parameter variations in this method have significantly fewer limitations. Therefore, the effect of various parameters on the structure can be examined. However, this does not mean that definitive answers can be obtained solely through the finite element method; rather, it can be considered complementary to experimental methods.

In recent years, due to significant advancements in finite element simulation software, it has become possible to easily simulate experimental studies in commonly used software such as ANSYS, LS-DYNA 3D, and ABAQUS.

### 3.2 Finite Element Method

The finite element method is a numerical method for solving problems of engineering and mathematical physics. Typical problem areas of interest in engineering and mathematical physics that are solvable by use of the finite element method include structural analysis, heat transfer, fluid flow, mass transport, and electromagnetic potential [20].

For physical systems involving complicated geometries, loadings, and material properties, it is generally not possible to obtain analytical mathematical solutions to simulate the response of the physical system. Analytical solutions are those given by a mathematical expression that yields the values of the desired unknown quantities at any location in a body (here total structure or physical system of interest) and are thus valid for an infinite number of locations in the body. These analytical solutions generally require the solution of ordinary or partial differential equations, typically created by engineers, physicists, and mathematicians to eliminate the need for the creation and testing of numerous prototype designs, which may be quite costly. Because of the complicated geometries, loadings, and material properties, the solution to these differential

equations is usually not obtainable. Hence, we need to rely on numerical methods, such as the finite element method, that can approximate the solution to these equations [20].

The finite element method (FEM) is a powerful tool for the numerical solution of a wide range of geometric problems. Its applications extend across various fields, including stress and deformation analysis for structures such as buildings, bridges, aircraft, and automobiles, as well as solving problems related to heat transfer, magnetic fields, seepage, and fluid flow. In the finite element method, a continuous domain is divided into smaller, simpler geometric components known as *finite elements*. This process is called *meshing*, and the common points where these elements connect are referred to as *nodes*. The material properties and internal stresses are defined in terms of the unknown displacements at the element corners. Based on the arrangement of the elements, their equations are assembled, and by incorporating external forces and boundary conditions at the nodes, the equilibrium equations for the entire system are obtained. These equations relate the nodal forces to the nodal displacements, with their coefficients representing the geometric and elastic properties of the finite elements. By solving these equations, the nodal displacements are determined, leading to the calculation of internal stresses. Below are various examples illustrating the meshing of continuous domains [21].

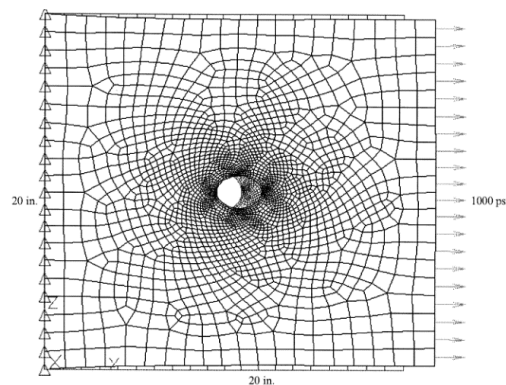


Figure 3.51: plate with a hole, showing the deformation of the plate overlaid on its undeformed state. The plate is fixed along the left edge and subjected to a tensile stress of 1000 psi along the right edge. The maximum horizontal displacement is  $7.046 \times 10^{-4}$  in

### 3.3 Abaqus Software

Abaqus is one of the most powerful finite element simulation software, capable of handling a wide range of analyses, from simple to highly advanced, with remarkable efficiency. Due to its user-

friendly interface compared to other similar software, it has attracted a large number of users in recent years. Abaqus offers the capability to analyze steel structures, reinforced concrete structures, fluid tank simulations considering fluid-structure interaction, concrete and earth dams, as well as temperature-dependent creep analysis, heat transfer simulations (both static linear/nonlinear and dynamic linear/nonlinear), and computational fluid dynamics (CFD) simulations.

Abaqus software consists of three main products: Abaqus/Standard, Abaqus/Explicit, and Abaqus/CFD. In addition to these core modules, it includes a variety of complementary products designed for specialized applications.

- **Abaqus/Standard**

Abaqus/Standard is the core product of the software, offering capabilities for linear and nonlinear static and thermal analyses, among others.

- **Abaqus/Explicit**

Abaqus/Explicit is a module specialized for dynamic linear and nonlinear analyses, such as explosion and impact simulations. It is also highly suitable for complex nonlinear problems, including contact condition changes in forming processes.

- **Abaqus/CFD**

Abaqus/CFD is designed for computational fluid dynamics (CFD) simulations and can handle a wide range of incompressible fluid flow problems, including laminar and turbulent flows, thermal convection flows, and mesh deformation problems

- **3.3.4 Abaqus/CAE**

Abaqus/CAE is the most comprehensive module of the software, featuring a graphical interface that allows users to efficiently create models, import geometries from other modeling software, assign material properties, define loads and boundary conditions, and generate high-quality meshes. It includes powerful mesh generation and model validation tools. Abaqus/CAE also enables real-time analysis visualization at every stage of the simulation. Upon completion of the analysis, the results can be viewed in a graphical format using the Visualization module.

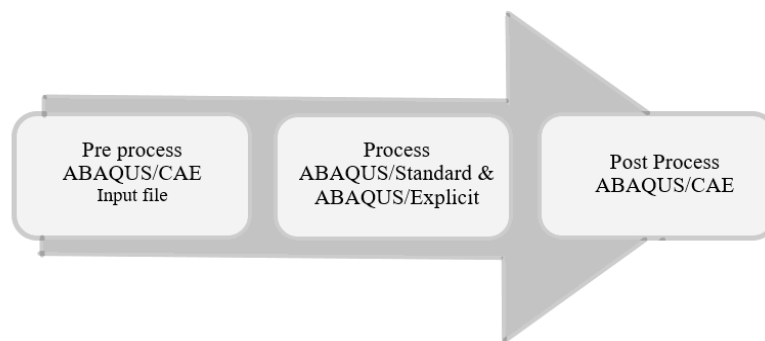
## 3.4 Introduction to Abaqus

Abaqus/CAE consists of multiple modules, each representing a logical aspect of the modeling process. For example, different modules are used to define the model geometry, assign material

properties, and generate the finite element mesh. The modeling and execution process progresses by transitioning from one module to another. Once the model is complete, Abaqus/CAE generates a text-based input file, which contains all the modeling instructions specified in different modules. This input file is then read by Abaqus/Standard or Abaqus/Explicit, where the computational analysis is performed in the processing stage. It is important to note that the analysis progress can be monitored at each stage. After the processing phase, the results are visualized in the post-processing stage using the Visualization module.

### 3.5 Basic Principles of Abaqus

A complete analysis in Abaqus/CAE typically consists of the following three distinct stages, which are schematically illustrated in the figure below.



*Figure 3.52: General Workflow of Abaqus Software*

- **Pre-processing Stage (Pre-Process)**

In this stage, the physical model of the problem is created, and an input file is prepared. This model is typically built graphically in Abaqus/CAE or other preprocessing software. Additionally, the Abaqus input file can be generated and directly imported into the simulation stage using scripting or programming.

- **Simulation Stage (Process)**

The simulation process involves computing the numerical problem defined in the pre-processing stage. This step analyzes the model and transfers the results to the post-processing stage. Depending on the complexity of the model and the computational power of the system, the processing time can range from a few milliseconds to several days. The



analysis duration is highly dependent on the computing power of the processor used for the simulation.

- **Post-processing Stage (Post-Process)**

In this stage, the results obtained from the simulation, including displacements, stresses, and other key variables, are evaluated. The Visualization module in Abaqus/CAE provides various tools for result interpretation, including color contour plots, animations, and deformed shape plots. Additionally, Cartesian plots and graphs can be generated within this module.

## 3.6 Modeling Stages

To perform the simulation of a process, Abaqus/CAE provides separate functional modules that allow users to execute the three main stages of a finite element analysis (FEA), as discussed in the previous section. The finite element simulation process in Abaqus/CAE consists of the following steps:

1. Part Module – Creating the geometric model of components.
2. Property Module – Defining material properties.
3. Assembly Module – Assembling different parts of the model.
4. Step Module – Defining and configuring analysis steps.
5. Interaction Module – Defining contact and interactions between surfaces.
6. Load Module – Applying loads and boundary conditions.
7. Mesh Module – Meshing the finite element model.
8. Job Module – Running the analysis.
9. Visualization Module – Displaying graphical output of the finite element results.

The following sections provide detailed explanations of each of these steps.

### 3.6.1 Creating the Geometric Model (Part Module)

In Abaqus/CAE, the Part module is used to create the geometric model of components. This module provides various tools to sketch, name, modify, and edit individual parts that make up the

model. Each part is initially created in a local coordinate system, and later, in the Assembly module, these parts are positioned within a global coordinate system to construct the final model.

The components of a cold-formed steel beam-to-column bolted connection consist of five parts, which are created in this module and modeled as shell elements for efficient finite element analysis:

1. Column (2 UNP 300 channels)
2. Column stiffeners (8 plates of size  $300 \times 150 \times 10$  mm, providing additional rigidity to the column section)
3. Through plate
4. Beam stiffeners (a combination of out-of-plane vertical and horizontal stiffeners, depending on the type of connection and model)
5. Curved flange beam (back-to-back channel configuration)

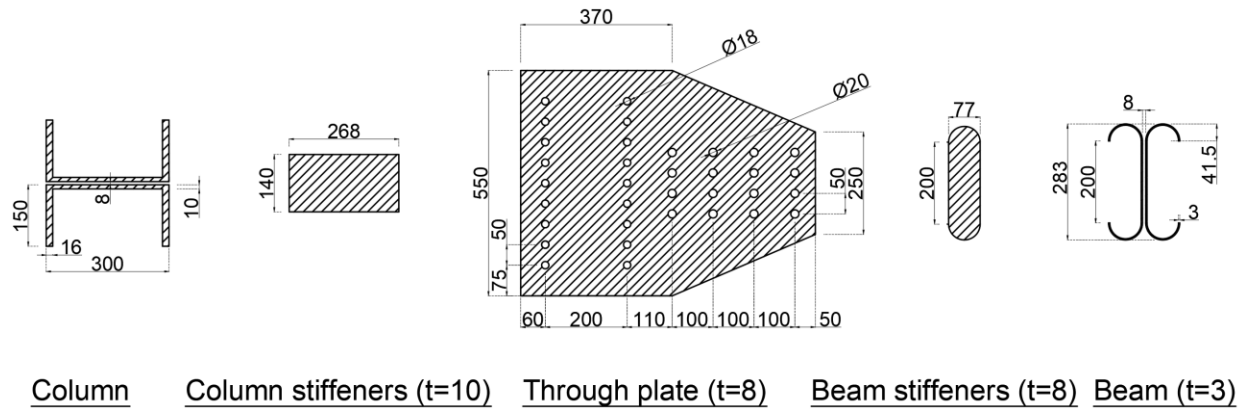
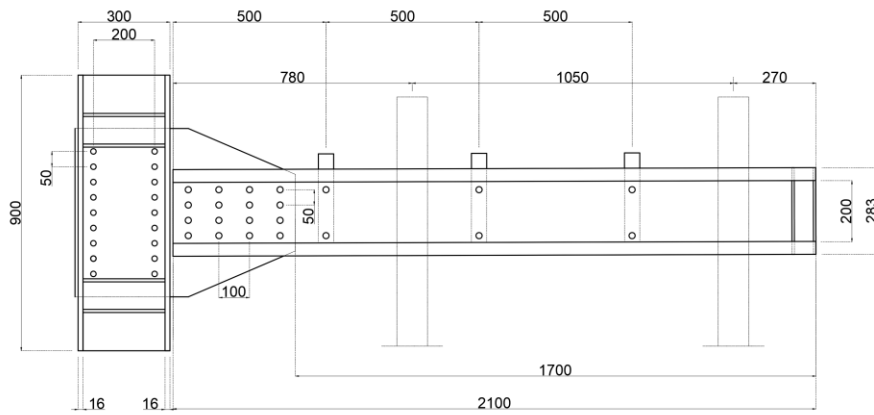
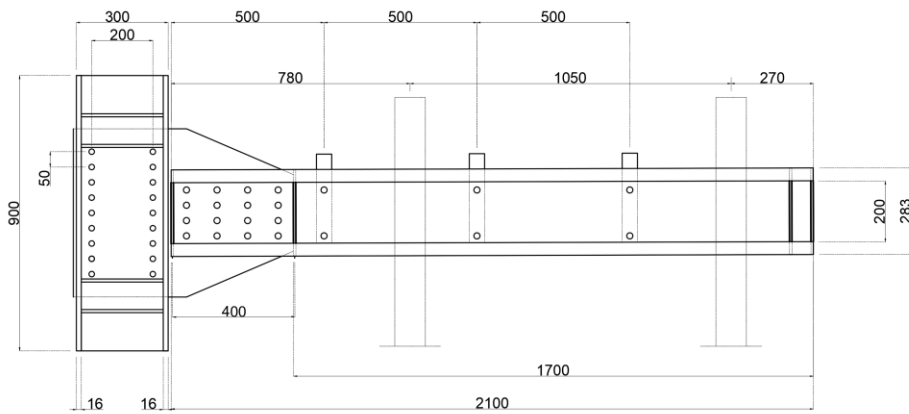


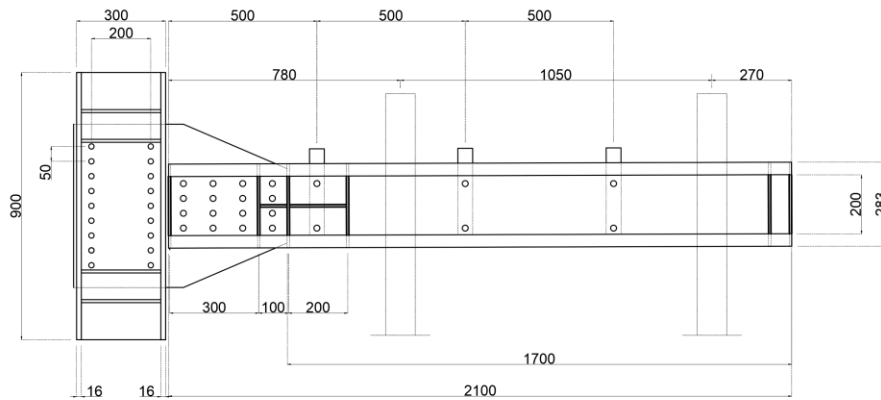
Figure 3.53: Model parts



Model A1



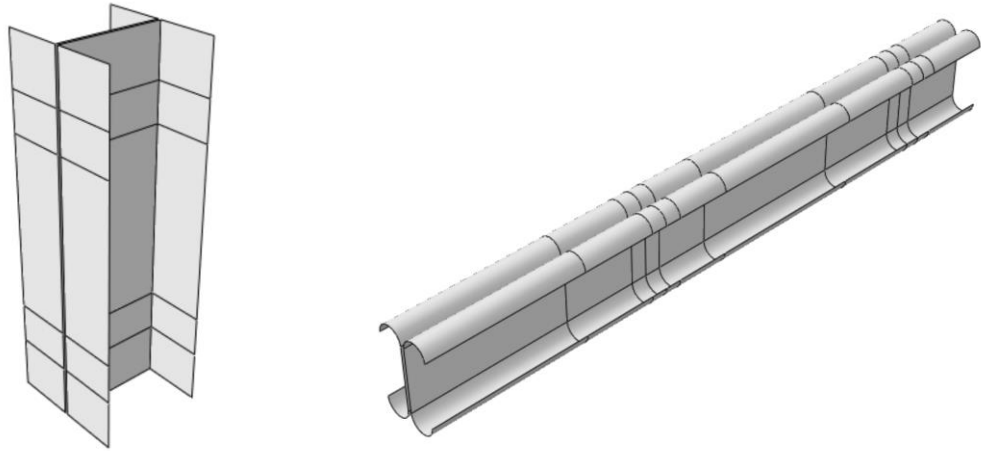
Model A2



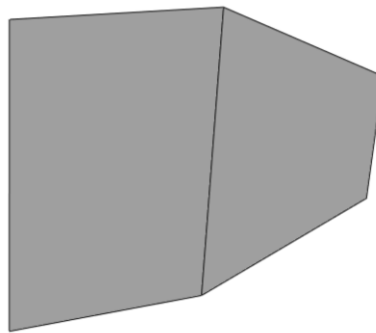
Model A3

*Figure 3.54: Models A1, A2 and A3*

Each component is modeled using shell elements to accurately capture structural behavior while optimizing computational efficiency. Shell modeling allows for a realistic representation of thin-walled sections commonly used in cold-formed steel structures, facilitating detailed stress and deformation analysis in Abaqus/CAE.



*Figure 3.55: CFS column and curved flange beam parts*



*Figure 3.56: through-plate part*

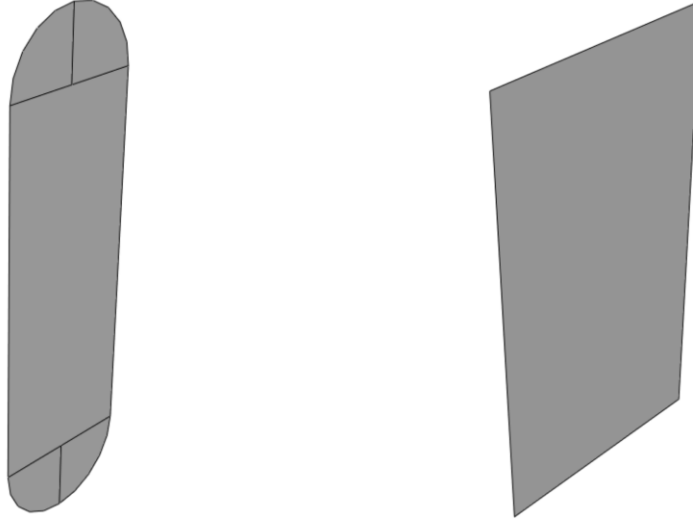


Figure 3.57: beam and column stiffeners parts

### 3.6.2 Defining Material Properties (Property Module)

**CFS Components:** The nonlinear stress–strain relationships of the CFS beam and the gusset plate materials were incorporated in ABAQUS [22] utilizing a two-stage material model proposed by Heidarali and Nethercot [23], fitted to the results of coupon tests reported by Sabbagh et al. [24]. In a first stage, the stress–strain behaviour was defined up to the 0.2% proof stress ( $\sigma_{0.2}$ ) using Eq. (1), initially proposed by Ramberg and Osgood [25] and later modified by Hill [26]. A straight line with a slope  $E = \frac{E_0}{100}$  was used in the second stage, as expressed by Eq. (2). In Eqs. (1) and (2),  $\varepsilon_{0.2}$  is the strain corresponding to the  $\sigma_{0.2}$  proof stress,  $E_0$  stands for the elastic modulus and  $n$  is a constant parameter that is used to determine the roundness of the stress-strain curve, which was assumed equal to 10, as recommended by Rasmussen [27].

$$\varepsilon = \frac{\sigma}{E_0} + 0.002 \left( \frac{\sigma}{\sigma_{0.2}} \right)^n, \quad \sigma \leq \sigma_{0.2} \quad (1)$$

$$\varepsilon = \varepsilon_{0.2} + \frac{\sigma - \sigma_{0.2}}{E}, \quad \sigma \geq \sigma_{0.2} \quad (2)$$

In the next step the engineering strains and stresses were converted to true strains  $\varepsilon_{true}$  and stresses  $\sigma_{true}$  to account for the reduced area due to necking in the tensile coupon tests and hence,  $\varepsilon_{ln}^{plastic}$  is the true plastic strain.

$$\sigma_{true} = \sigma_{engineering} * (1 + \varepsilon_{engineering}) \quad (3)$$

$$\varepsilon_{true} = \ln(1 + \varepsilon_{engineering}) \quad (4)$$

$$\varepsilon_{ln}^{plastic} = \ln(1 + \varepsilon_{engineering}) - \frac{\sigma_{true}}{E_{modulus}} \quad (5)$$

Then the linear kinematic hardening rule available in ABAQUS was adopted to simulate the hardening behaviour of the material [28]. The (engineering) material properties of the connection components are summarized in the Table below:

Table 8: material properties for beam and gusset plate

| Element      | $\sigma_{0.2}(MPa)$ | $f_u(MPa)$ |
|--------------|---------------------|------------|
| Beam         | 313                 | 479        |
| Gusset Plate | 353                 | 516        |

For the column and all the stiffeners, a yield strength of  $F_y = 240 \text{ Mpa}$  and an ultimate tensile strength of  $F_u = 370 \text{ Mpa}$  were considered. Also, elastic modulus of  $E_0 = 210 \text{ GPa}$ , Poisson ratio of  $\nu = 0.3$  and the ultimate strain 0.08 were utilized for the FE models.

### 3.6.3 Assembling Different Parts (Assembly Module)

After completing the creation of the model components in the Part module and assigning materials in the Property module, the next step is to assemble the parts and transfer all component instances from the local coordinate system to the global coordinate system. The assembly process may include one or multiple parts, depending on the type of analysis. The figure below illustrates all the components properly positioned in their final assembled state.

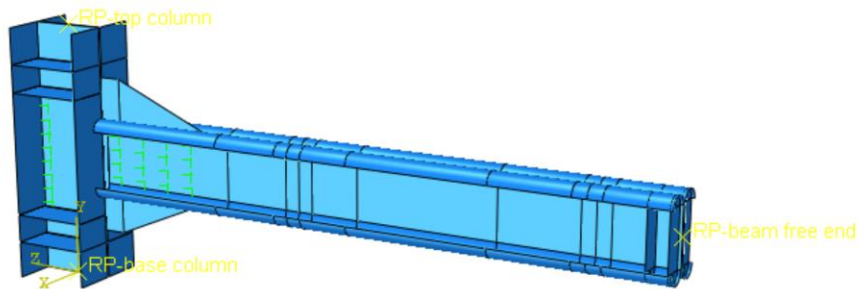


Figure 3.58: Assembled parts for FE model A1

### 3.6.4 Creating and Configuring Analysis Steps (Step Module)

The Step module is used to create and configure analysis steps and define the required output results. In general, this module is utilized for tasks such as:

- Creating a Step for performing different types of analyses
- Specifying the desired output results from an analysis
- Defining analysis controls

In this study, Static general analysis is used, which can be performed either linearly or nonlinearly. The required output results from this analysis are displacement and force. These outputs are assigned to specific sets, and within this module, they are defined under the History Output section, which is used for generating graphical representations of the results.

### 3.6.5 Defining Surface Interactions (Interaction Module)

In this thesis, the interaction in the analyzed samples was modeled using General Contact (Standard). Tangential Behavior was defined with a penalty method as the friction formulation, isotropic directionality, and a friction coefficient of 0.25. For Normal Behavior, the "Hard Contact" model was applied as the pressure-overclosure definition to avoid penetration of the surfaces into each other.

The interaction between the beam and stiffeners was established using a tie constraint, where the beam surface was designated as the main surface, and the stiffener edges in contact with the beam surface were assigned as the secondary surface. A similar approach was implemented for the column and stiffeners, considering the column surface as the main surface, while the stiffener edges in contact with the column surface were treated as the secondary surface.

To ensure the proper interaction of structural components, a kinematic coupling constraint was defined for the top and bottom section nodes of the column and the free end section nodes of the beam (where the external load was applied), coupling these nodes to the Reference Point (RP) located at mid-height of the webs. Additionally, the webs of the back-to-back channels of the beam were connected at three different locations, spaced 500 mm apart, using tie constraints to simulate the bolts outside the connection zone, ensuring structural integrity and alignment.

For the bolted connections, two fastener groups were defined to model the interactions between the column and gusset plate as well as the beam and gusset plate. This modelling technique creates





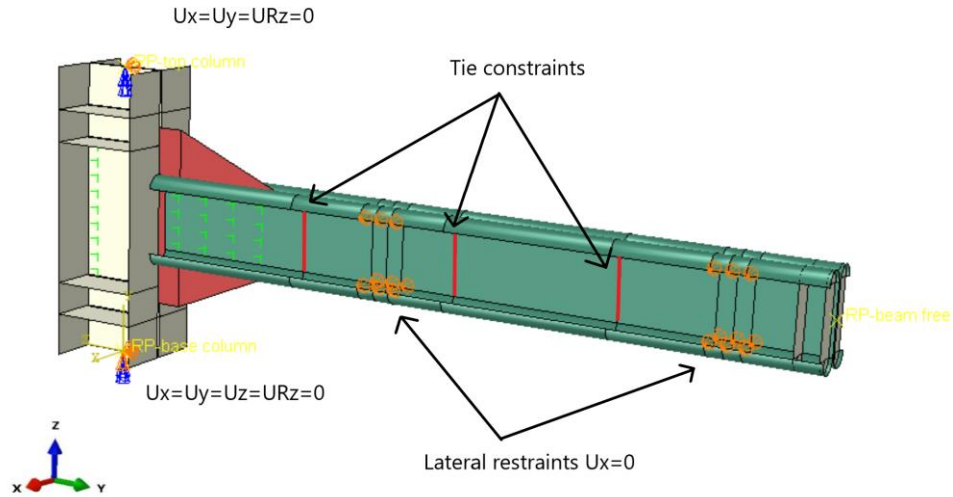


Figure 3.60: Boundary conditions of the FE models.

The FE models of the connections were loaded using a displacement-controlled approach under cyclic conditions at the free end of the beam section. While a cyclic analyses the loading protocol presented in section S6.2 of the AISC 341-16 [29] provisions (as used in the corresponding experiments) was adopted. This protocol includes the following steps (figure 3.61):

- (1) 6 cycles at  $\theta = 0.00375$  rad
- (2) 6 cycles at  $\theta = 0.00500$  rad
- (3) 6 cycles at  $\theta = 0.00750$  rad
- (4) 4 cycles at  $\theta = 0.010$  rad
- (5) 2 cycles at  $\theta = 0.015$  rad
- (6) 2 cycles at  $\theta = 0.02$  rad
- (7) 2 cycles at  $\theta = 0.03$  rad
- (8) 2 cycles at  $\theta = 0.04$  rad
- (9) Continue loading in increments of  $\theta = 0.01$  rad, applying two cycles of loading in each step.

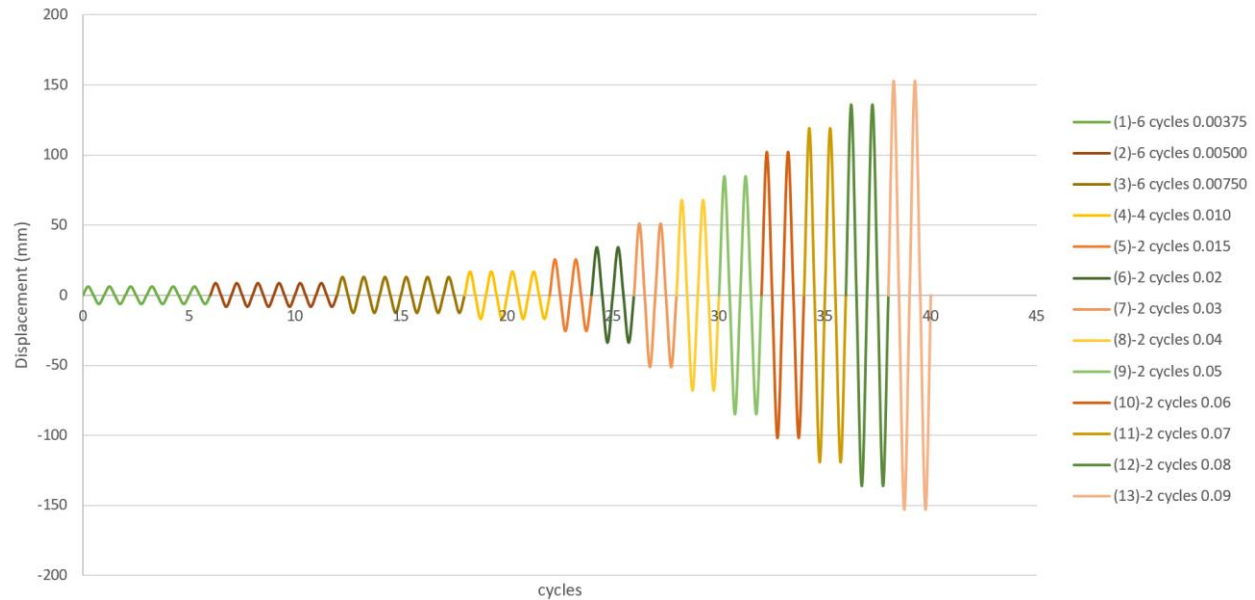


Figure 3.61: Cyclic loading protocol adopted from AISC 341-16 [43].

### 3.6.7 Finite Element Meshing (Mesh Module)

The Mesh Module is used for generating the finite element mesh in the model. ABAQUS provides various types of finite elements, which are utilized to construct specialized models. Before meshing, the appropriate element type must be determined. Given the importance of meshing techniques and element selection, the user must have sufficient knowledge of finite elements.

Therefore, this section first presents the characteristics of an element along with theoretical explanations, followed by an overview of how these concepts are implemented within the Mesh environment. ABAQUS supports a wide range of elements, offering significant flexibility to users for modeling and analyzing various types of problems. In the following, five key characteristics of an element that define its behavior are introduced.

Each finite element possesses the following five key characteristics:

1. **Element Family:** The figure below illustrates different element families commonly used in stress analysis problems. One of the main differences between elements from different families is their geometric shape.

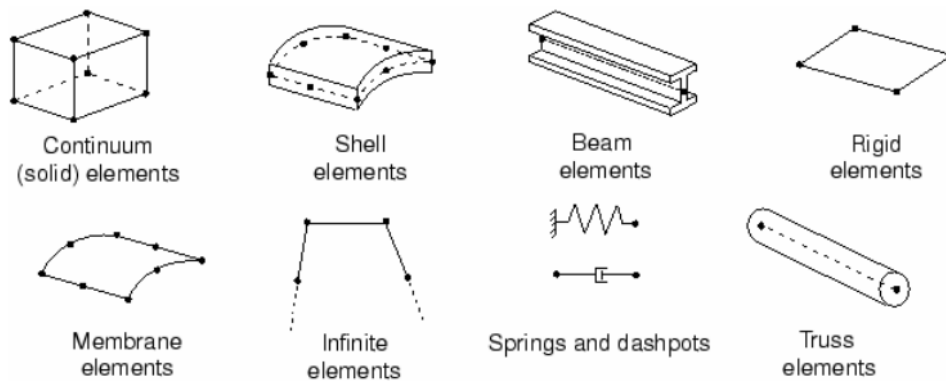
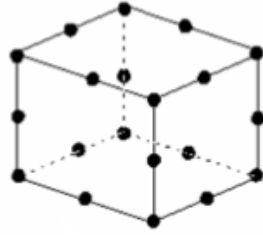


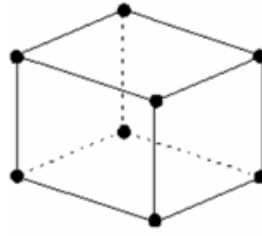
Figure 3.62: Element Groups in ABAQUS/CAE

2. Degrees of Freedom (DOF): The degrees of freedom are the primary variables calculated during analysis and are directly related to the element family. In a stress-displacement model, the primary degrees of freedom are the nodal displacements. For Shell and Beam elements, rotational degrees of freedom at the nodes are also included.
3. Number of Nodes and Interpolation Order: Displacements, rotations, temperature, and other degrees of freedom are computed only at the element nodes. At any other point inside the element, these values must be interpolated from the nodal values. The interpolation order is generally determined by the number of nodes per element:
  - Linear (First-Order) Elements: Elements with nodes only at the corners, such as C3D8, use linear interpolation in each direction. These are referred to as linear or first-order elements.
  - Quadratic (Second-Order) Elements: Elements with mid-edge nodes, such as C3D20, use parabolic interpolation and are known as quadratic or second-order elements.



(20-node brick, C3D20)

Figure 3.63: Quadratic (Parabolic) Element



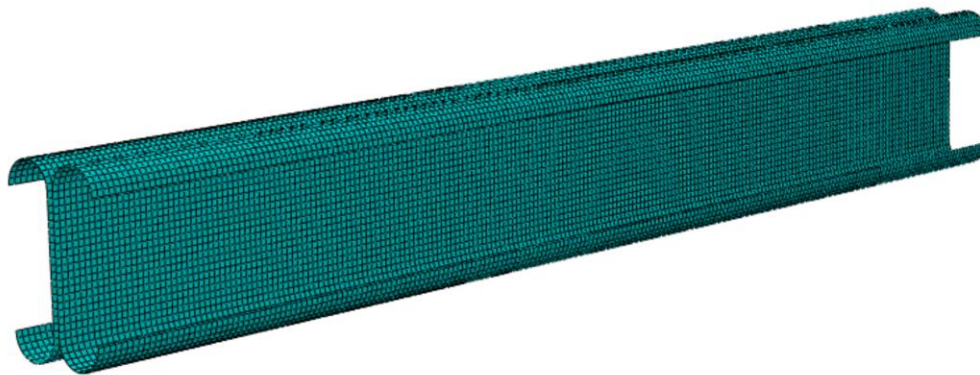
(8-node brick, C3D8)

Figure 3.64: Linear Element

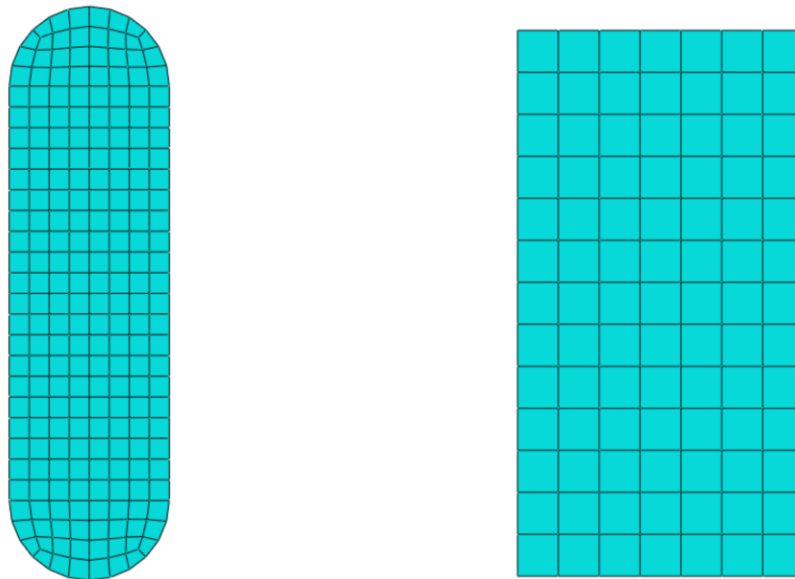
4. Element Formulation: The formulation of an element is based on the mathematical theory governing its behavior. All elements used in stress-displacement analysis employ either Lagrangian formulation or control mass formulation. In Lagrangian formulation, the material inside the element remains within the element throughout the analysis and cannot flow beyond its boundaries. In contrast, the Eulerian formulation, or control volume approach, keeps the element fixed in space while material flows through it.
5. Numerical Integration: ABAQUS uses numerical methods for integrating various quantities over the element volume. The Gaussian quadrature method is employed to evaluate material behavior at integration points within an element.

The optimal mesh size is determined based on a validated model of specimen behavior, using a trial-and-error approach, where mesh size and element count are adjusted to achieve accuracy.

The S4R general-purpose finite element available in ABAQUS was employed to model all connection components. This four-noded shell element has six degrees of freedom per node. It can account for nonlinear material properties and finite membrane strains and features hourglass control and reduced integration. Following a mesh sensitivity analysis, a mesh size of  $10 \times 10$  mm was selected for beam, beam-stiffeners and through-plate and a mesh size of  $20 \times 20$  mm was selected for column and column-stiffeners, to guarantee adequate numerical accuracy while keeping the computational time within acceptable limits.



*Figure 3.65: Mesh configuration for beam*



*Figure 3.66: Mesh configuration for beam and column stiffeners*

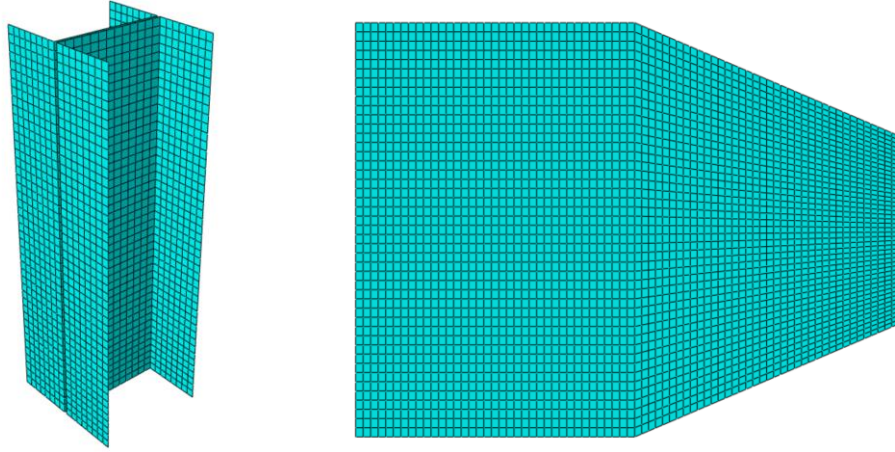


Figure 3.67: Mesh configuration for column and throughplate



Figure 3.68: Mesh of assembled components

### 3.7 Validation of Numerical Simulations Against Experimental Results

In this study, to assess the reliability of the numerical model, three numerical models were validated against the corresponding experimental specimens as reported in [15], focusing on the moment–rotation ( $M$ – $\theta$ ) behavior under cyclic loading conditions. The results are presented in terms of the normalized moment ( $M/M_p$ ) plotted against the applied rotation ( $\theta$ ). Here,  $M_p$  represents the nominal plastic moment of the beam sections, calculated as 67 kN.m for all specimens (A1, A2, A3), based on a nominal yield stress of  $f_y = 275 \text{ Mpa}$ .

### Model A1:

As illustrated, the FEA model (red line) shows strong agreement with the experimental hysteresis response (black line) in terms of overall shape, strength envelope, and cyclic behavior. The numerical model successfully captures the stiffness degradation, and energy dissipation pattern across successive cycles. While slight deviations are present, particularly in the post-peak unloading branches, these are likely attributed to local imperfections, connection slip present in the experimental setup but not explicitly modeled in the simulation. Overall, the comparison validates the reliability of the finite element model for simulating cyclic behavior of the back-to-back cold-formed steel joint.

# A1

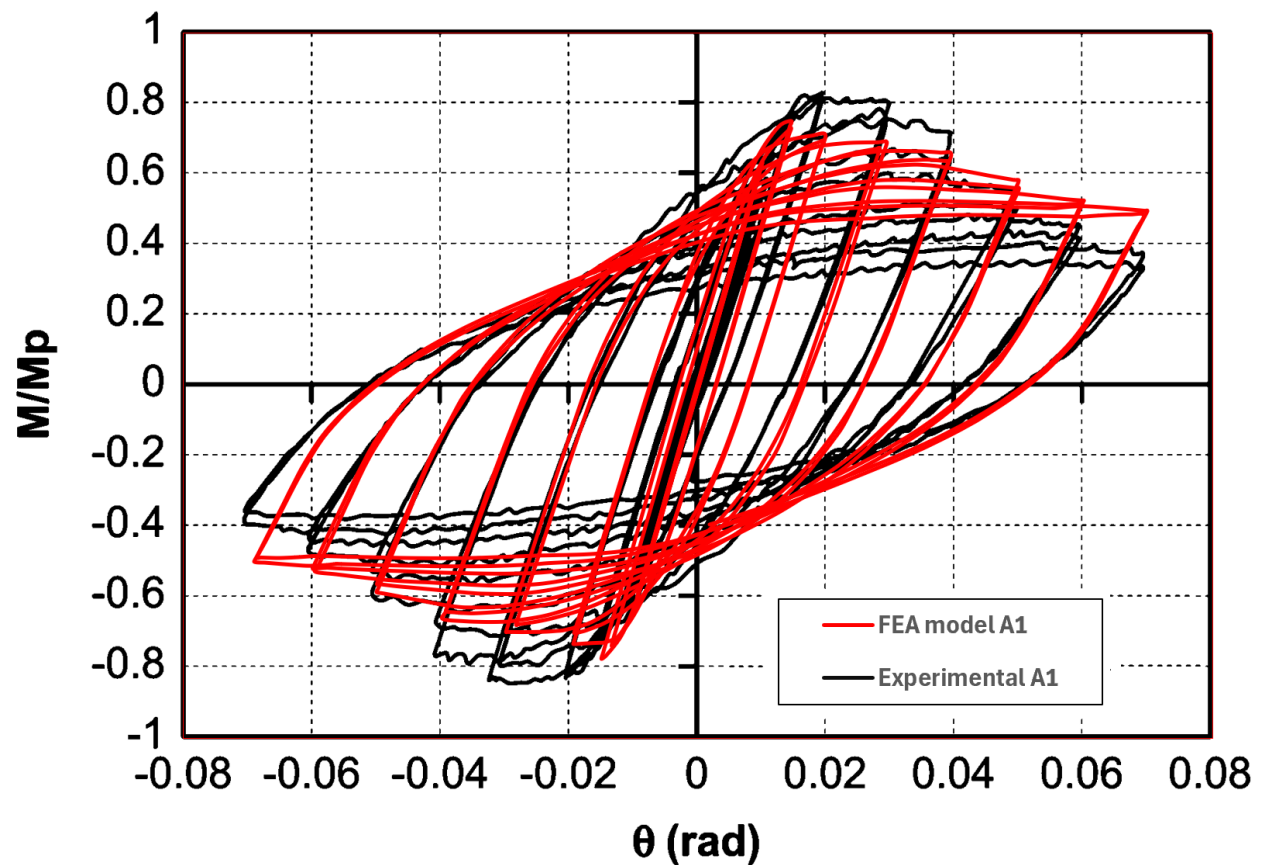


Figure 3.69: Moment–Rotation comparison ( $M/M_p$  vs.  $\theta$ ) between FEA and experimental result for Model A1 under cyclic loading [15].

To verify local effects and failure mechanisms, the von Mises stress distribution and the actual deformed specimen are shown side by side in Figure 3.70. As we can see photograph of



experimental specimen A1 post-testing. Evidence of yielding and local buckling corresponds well with FEA predictions.

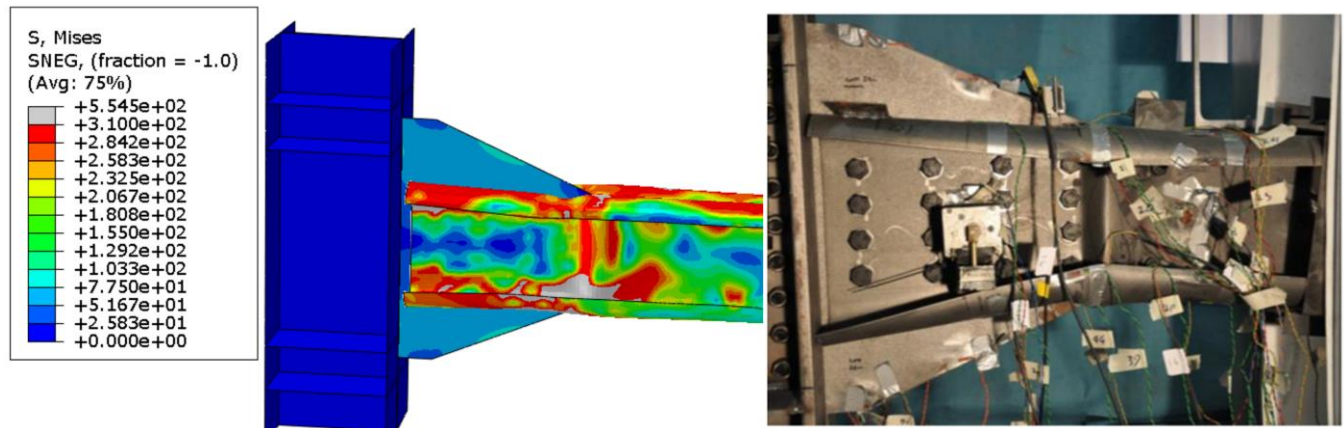


Figure 3.70: Left – Von Mises stress field (MPa) from FEA simulation of Model A1 at peak load. Right – Photograph of specimen A1 after cyclic testing, showing deformations in predicted regions.

### Model A2:

The finite element model (red line) demonstrates good agreement with the experimental results (black line), capturing key aspects of the cyclic hysteresis, including strength development, unloading paths, and stiffness degradation. The cyclic loops follow a similar shape, with minor differences observed in the pinching behavior and unloading branches at higher deformation levels. These may be attributed to factors such as connection slip, local imperfections, or simplifications in the contact modeling.



A2

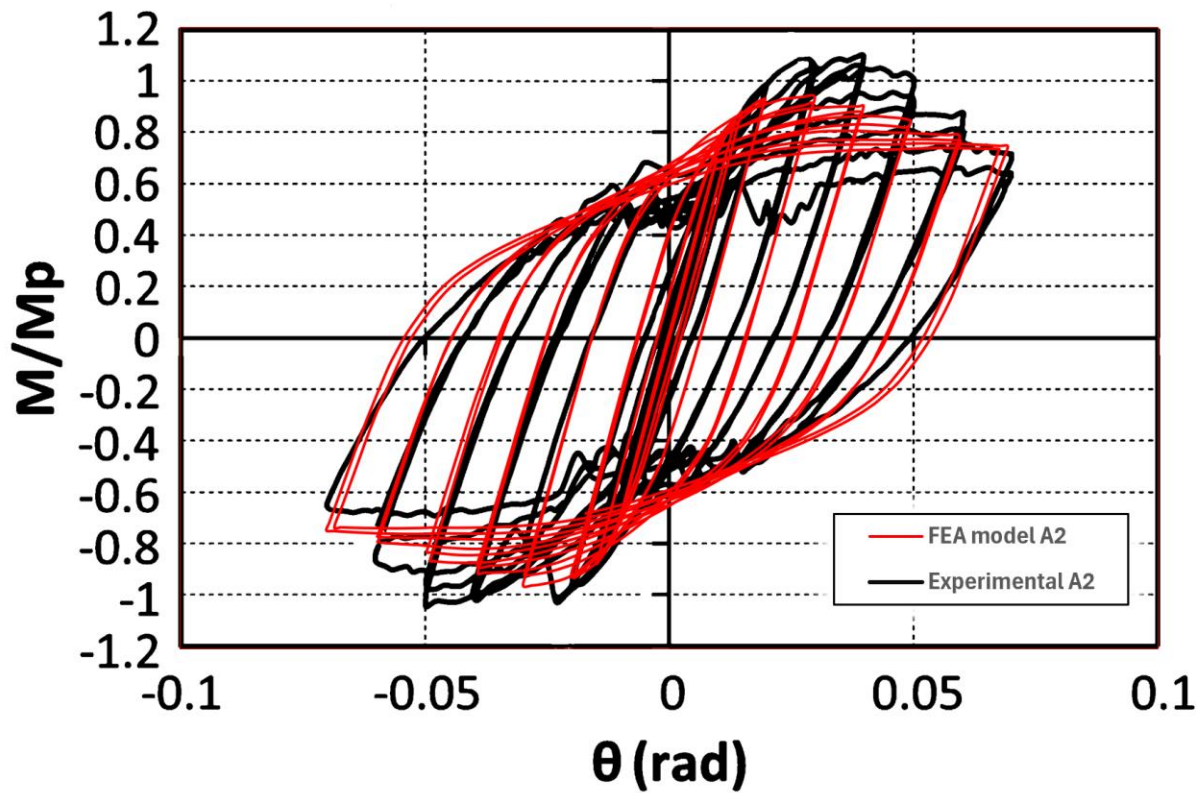


Figure 3.71: Moment–Rotation comparison ( $M/M_p$  vs.  $\theta$ ) between FEA and experimental result for Model A2 under cyclic loading [15].

As we can see in Figure 3.72, the FEA simulation highlights critical stress zones along the beam–stiffness interface and flanges, with values approaching or exceeding the yield limit. The experimental image confirms plastic deformation and local buckling in these regions, providing strong evidence of the model’s predictive capability.

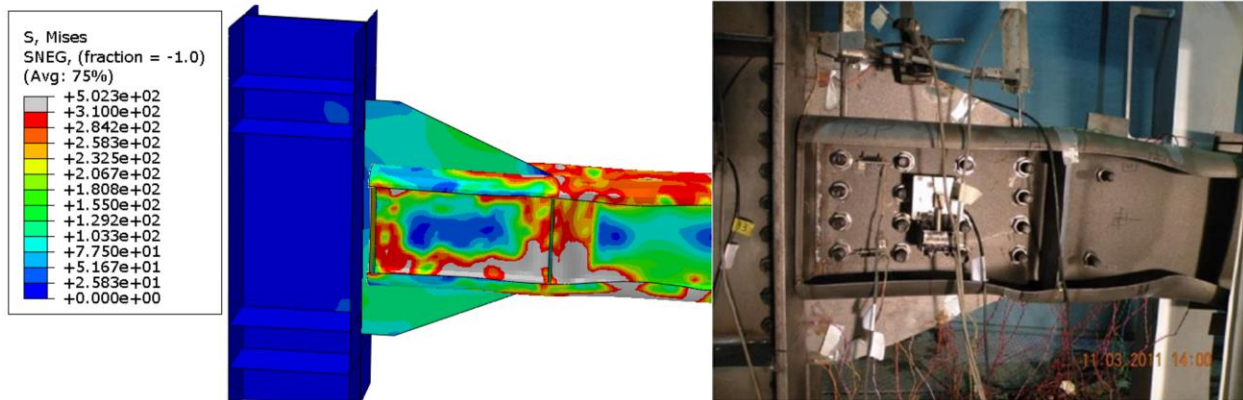


Figure 3.72: Left – Von Mises stress field (MPa) from FEA simulation of Model A2 at peak load. Right – Photograph of specimen A2 after cyclic testing, showing deformations in predicted regions.

### Model A3:

The numerical results (red line) closely match the experimental hysteresis loops (black line), successfully replicating the cyclic stiffness degradation. The model also reproduces the ultimate moment capacity and ductility observed during testing, with acceptable divergence occurring primarily in the late cycles under large deformations.

A3

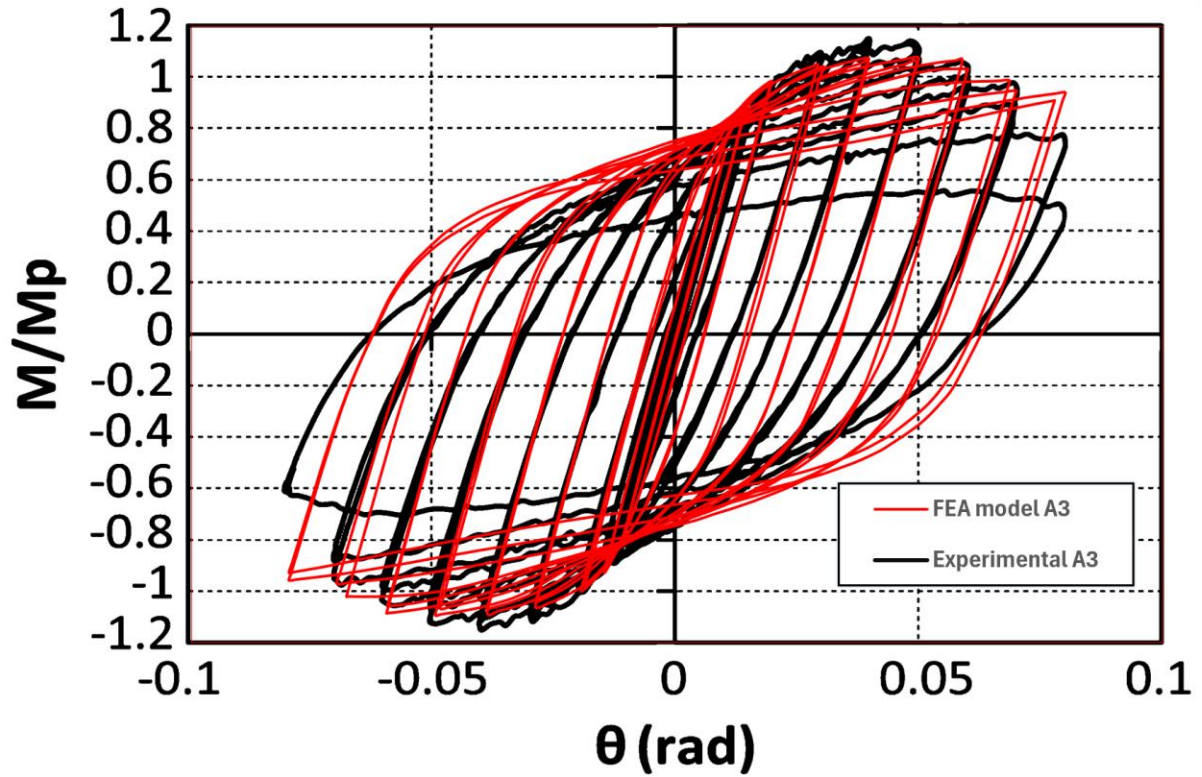


Figure 3.73: Moment–Rotation comparison ( $M/M_p$  vs.  $\theta$ ) between FEA and experimental result for Model A3 under cyclic loading [15].

To evaluate local effects and damage mechanisms, Figure 3.74 presents the von Mises stress distribution from the FEA model at peak loading (left), alongside the photograph of the tested specimen A3 (right). High stress concentrations are visible near the web stiffeners and the joint

interface, which corresponds to the regions where plastic deformation and local buckling developed in the physical specimen. This visual and numerical agreement validates the model's ability to capture both global and local response characteristics

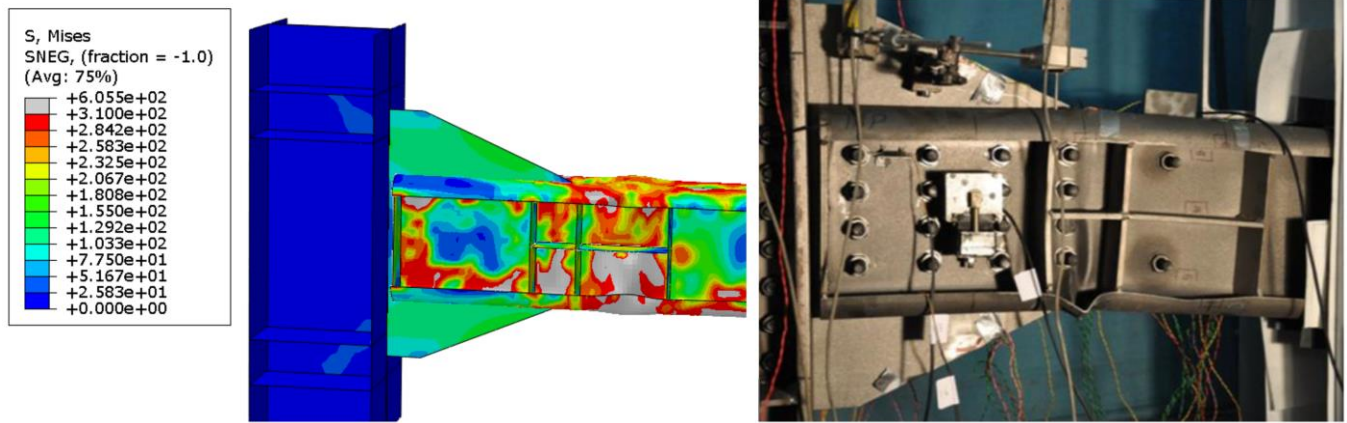


Figure 3.74: Left – Von Mises stress field (MPa) from FEA simulation of Model A3 at peak load. Right – Photograph of specimen A3 after cyclic testing, showing deformations in predicted regions.

## Chapter 4. Modeling of Plain Concrete

### 4.1 Elasto-Plastic Modeling of Concrete

This chapter presents the implementation details of two elasto-plastic models for concrete: the Concrete Damaged Plasticity (CDP) model and the Drucker-Prager model. The study is purely numerical, focusing on evaluating and comparing these models in representing concrete stiffness in connections. Since no experimental calibration of material parameters is performed, all parameters are either sourced from relevant literature or selected within a statistically reasonable range.

The Concrete Damaged Plasticity (CDP) model is chosen for its ability to accurately capture the nonlinear behavior of concrete, particularly tensile cracking and compressive crushing. By incorporating both plasticity and damage mechanics, the model provides a realistic representation of concrete degradation under monotonic and cyclic loading. It defines separate damage parameters for tension and compression, making it well-suited for simulating structural elements subject to progressive cracking, stiffness degradation, and irreversible strain effects.

In contrast, the Drucker-Prager model is selected for its ability to represent general plasticity in concrete when confinement effects are negligible. While primarily used for pressure-dependent materials such as soils and rocks, it can also model plastic yielding in concrete under certain conditions. However, unlike the CDP model, the Drucker-Prager formulation does not explicitly account for tensile cracking and stiffness degradation, making it less suitable for applications where tensile failure and post-peak softening are significant.

### 4.2 The Concrete Damaged Plasticity

The Concrete Damaged Plasticity (CDP) model is a continuum, plasticity-based, damage model for concrete that developed by Lubliner et al [38] and later, some modification was introduced by Lee J [39]. It assumes that the main two failure mechanisms are tensile cracking and compressive crushing of the concrete material. The evolution of the yield (or failure) surface is controlled by two hardening variables,  $\varepsilon_t^{pl}$  and  $\varepsilon_c^{pl}$  linked to failure mechanisms under tension and compression loading, respectively. We refer to  $\varepsilon_t^{pl}$  and  $\varepsilon_c^{pl}$  as tensile and compressive equivalent plastic

strains, respectively. The model assumes that the uniaxial tensile and compressive response of concrete is characterized by damaged plasticity.

as shown in figure 4.75 the unloaded response of concrete specimen seems to be weakened because the elastic stiffness of the material appears to be damaged or degraded. The degradation of the elastic stiffness on the strain softening branch of the stress-strain curve is characterized by two damage variables,  $d_t$  and  $d_c$ , which can take values from zero to one. Zero represents the undamaged material where one represents total loss of strength (Abaqus User Manual, 2008).  $E_0$  is the initial (undamaged) elastic stiffness of the material and  $\varepsilon_c^{pl}$ ,  $\varepsilon_t^{pl}$ ,  $\varepsilon_c^{in}$ ,  $\varepsilon_t^{in}$  are compressive plastic strain, tensile plastic strain, compressive inelastic strain and tensile inelastic strain respectively. The stress-strain relations under uniaxial tension and compression are taken into account in equations below, respectively.

$$\sigma_t = (1 - d_t) \cdot E_0 \cdot (\varepsilon_t - \varepsilon_t^{pl}) \quad (1)$$

$$\sigma_c = (1 - d_c) \cdot E_0 \cdot (\varepsilon_c - \varepsilon_c^{pl}) \quad (2)$$

Interface behavior between rebar and concrete is modeled by implementing tension stiffening in the concrete modeling to simulate load transfer across the cracks through the rebar. Tension stiffening also allows to model strain-softening behavior for cracked concrete. Thus it is necessary to define Tension stiffening in CDP model. ABAQUS allows us to specify Tension Stiffening by post failure stress-strain relation or by applying a fracture energy cracking criterion (Abaqus User Manual, 2008). Interface behavior between rebar and concrete is modeled by implementing tension stiffening in the concrete modeling to simulate load transfer across the cracks through the rebar. Tension stiffening also allows to model strain-softening behavior for cracked concrete. Thus it is necessary to define Tension stiffening in CDP model. ABAQUS allows us to specify Tension Stiffening by post failure stress-strain relation or by applying a fracture energy cracking criterion (Abaqus User Manual, 2008).

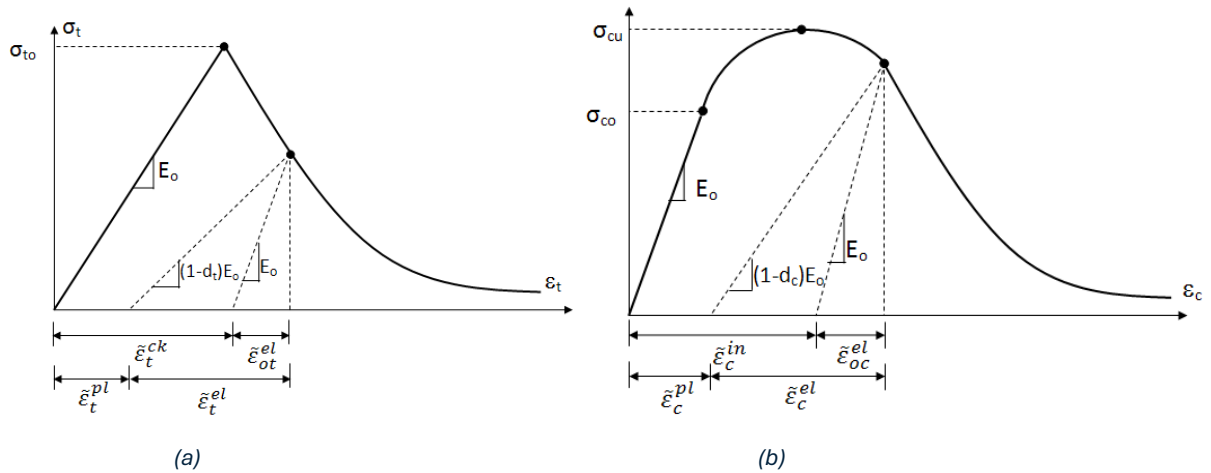


Figure 4.75: Response of concrete to uniaxial loading in tension (a) and compression (b).

The post-failure behavior for direct straining is modeled with tension stiffening, which allows you to define the strain-softening behavior for cracked concrete. This behavior also allows for the effects of the reinforcement interaction with concrete to be simulated in a simple manner. Tension stiffening is required in the concrete damaged plasticity model. You can specify tension stiffening by means of a post-failure stress-strain relation or by applying a fracture energy cracking criterion.

In cases with little or no reinforcement, the specification of a post-failure stress-strain relation introduces mesh sensitivity in the results, in the sense that the finite element predictions do not converge to a unique solution as the mesh is refined because mesh refinement leads to narrower crack bands. This problem typically occurs if cracking failure occurs only at localized regions in the structure and mesh refinement does not result in the formation of additional cracks. If cracking failure is distributed evenly (either due to the effect of rebar or due to the presence of stabilizing elastic material, as in the case of plate bending), mesh sensitivity is less of a concern.

To overcome this unreasonable mesh sensitivity problem Hillerborg's (1976) fracture energy approach can be used instead of post failure stress-strain relation (Hillerborg et al., 1976). In this approach; the amount of energy (GF) which is required to open a unit area of crack is assumed as a material property. Thus, concrete's brittle behavior is defined by stress-displacement response rather than a stress-strain response. Specifying the post failure stress versus corresponding crack-ing displacement is enough to describe this approach as shown in Fig. 4.75 (a-b) (Abaqus User Manual, 2008).



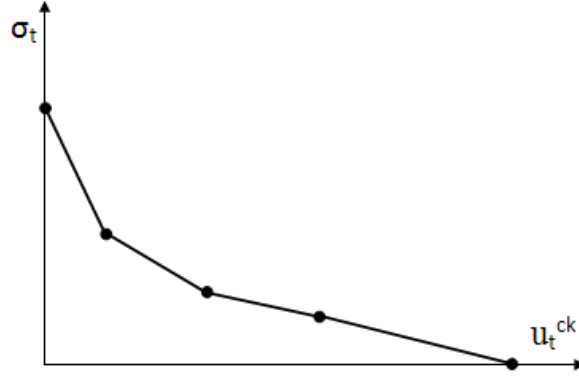


Figure 4.76: Post-failure stress-displacement curve

As an alternative, GF can be implemented directly as a material property. However, in this case, a linear loss of strength after cracking is assumed (Fig. 4.77).

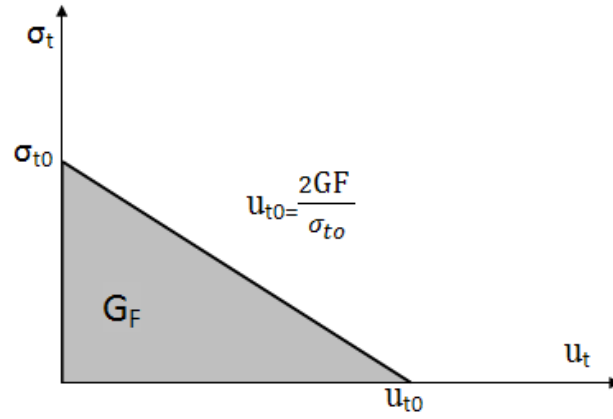


Figure 4.77: Post-failure stress-fracture energy curve

From CDP perspective, ABAQUS automatically calculates both plastic displacement values using the Eq. (1) and Eq. (2).

$$u_t^{pl} = \varepsilon_t^{ck} - \frac{d_t}{(1-d_t)} \frac{\sigma_t l_0}{E_0} \quad (3)$$

$$u_c^{pl} = \varepsilon_c^{ck} - \frac{d_c}{(1-d_c)} \frac{\sigma_c}{E_0} \quad (4)$$

From these equations “effective” tensile and compressive cohesion stresses ( $\bar{\sigma}_t, \bar{\sigma}_c$ ) can be defined as:

$$\bar{\sigma}_t = \frac{\sigma_t}{(1-d_t)} = E_0 (\varepsilon_t - \varepsilon_t^{pl}) \quad (5)$$

$$\bar{\sigma}_c = \frac{\sigma_c}{(1-d_c)} = E_0 (\varepsilon_c - \varepsilon_c^{pl}) \quad (6)$$

The effective cohesion stresses determines the size of the yield (or failure) surface (see Fig. 4.78).



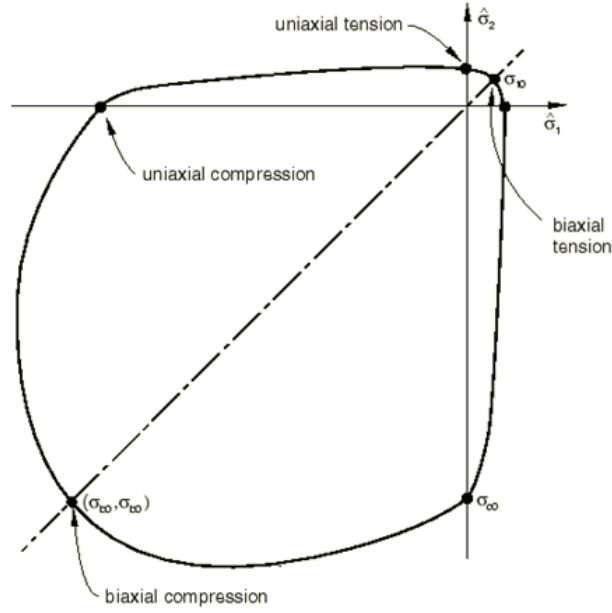


Figure 4.78: Yield surface in plane stress.

Under uniaxial cyclic loading conditions, the degradation mechanisms are quite complex, involving the opening and closing of previously formed micro-cracks, as well as their interaction. Experimentally, it is observed that there is some recovery of the elastic stiffness as the load changes sign during a uniaxial cyclic test. The stiffness recovery effect, also known as the “unilateral effect,” is an important aspect of the concrete behavior under cyclic loading. The effect is usually more pronounced as the load changes from tension to compression, causing tensile cracks to close, which results in the recovery of the compressive stiffness.

The concrete damaged plasticity model assumes that the reduction of the elastic modulus is given in terms of a scalar degradation variable  $d$  as

$$E = (1 - d)E_0 \quad (7)$$

where  $E_0$  is the initial (undamaged) modulus of the material. This expression holds both in the tensile ( $\sigma_{11} > 0$ ) and the compressive ( $\sigma_{11} < 0$ ) sides of the cycle. The stiffness degradation variable,  $d$ , is a function of the stress state and the uniaxial damage variables,  $d_t$  and  $d_c$ . For the uniaxial cyclic conditions ABAQUS assumes that

$$(1 - d) = (1 - s_t d_c)(1 - s_c d_t) \quad (8)$$

where  $s_t$  and  $s_c$  are functions of the stress state that are introduced to model stiffness recovery effects associated with stress reversals. They are defined according to

$$s_t = 1 - \omega_t r^*(\sigma_{11}); \quad 0 \leq \omega_t \leq 1 \quad (9)$$

$$s_c = 1 - \omega_c (1 - r^*(\sigma_{11})); \quad 0 \leq \omega_c \leq 1 \quad (10)$$

Where,

$$r^*(\sigma_{11}) = H(\sigma_{11}) = \begin{cases} 1 & \text{if } \sigma_{11} > 0 \\ 0 & \text{if } \sigma_{11} < 0 \end{cases} \quad (11)$$

The weight factors  $\omega_t$  and  $\omega_c$ , which are assumed to be material properties, control the recovery of the tensile and compressive stiffness upon load reversal (figure 4.79).

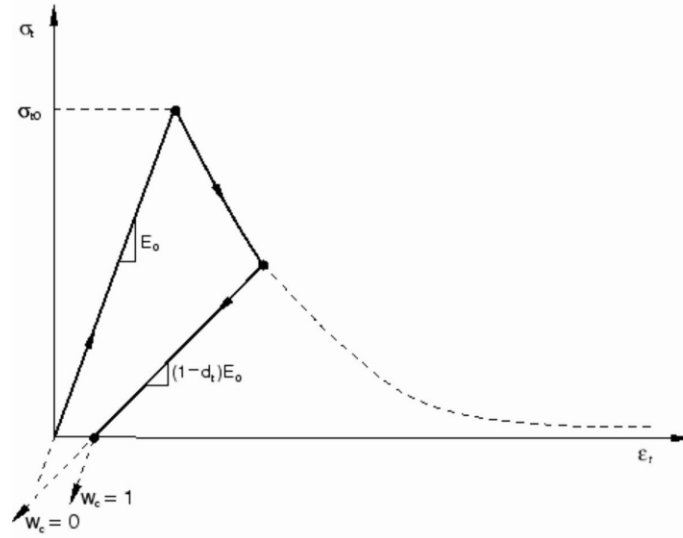


Figure 4.79: Illustration of the effect of the compression stiffness recovery parameter  $\omega_c$

The experimental observation in most quasi-brittle materials, including concrete, is that the compressive stiffness is recovered upon crack closure as the load changes from tension to compression. On the other hand, the tensile stiffness is not recovered as the load changes from compression to tension once crushing micro-cracks have developed. This behavior, which corresponds to  $\omega_t = 0$  and  $\omega_c = 1$ , is the default used by ABAQUS (figure 4.80).

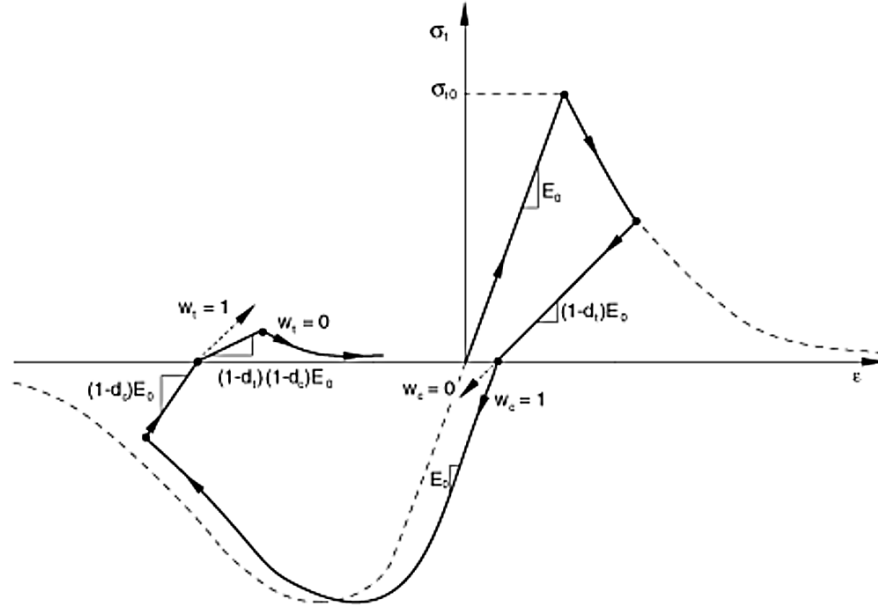


Figure 4.80: Uniaxial load cycle (tension-compression-tension)

In this study, the Simplified Damage Plasticity Model for Concrete was adopted to represent tensile and compressive damage behavior under loading. The evolution of material degradation was described using scalar damage variables for tension and compression, defined by the following expressions [40]:

$$d_t = 1 - \frac{\sigma_t}{\sigma_{t0}} \quad (12)$$

$$d_c = 1 - \frac{\sigma_c}{\sigma_{cu}} \quad (13)$$

These formulations allow for a simplified yet effective representation of stiffness degradation in concrete elements under cyclic or progressive loading, making them suitable for nonlinear finite element analysis in the context of fully bonded infill behavior.

### 4.3 The Drucker-Prager Model

The yielding part of the confined stress–strain curve for concrete, which is the part after the proportional limit stress, is treated using the Drucker–Prager yield criterion model available in the ABAQUS material library. The model is used to define yield surface and flow potential parameters for materials subjected to triaxial compressive stresses. Two parameters DRUCKER PRAGER and DRUCKER PRAGER HARDENING are used to define the yield stage of the concrete. The

linear Drucker–Prager yield criterion  $G$  (Fig. 4.81) is used with associated flow and the isotropic rule to model the yield surface of concrete, which is expressed as [33][34][35].

$$G = t - p \tan \beta - d = 0 \quad (14)$$

$$p = \frac{-(\sigma_1 + \sigma_2 + \sigma_3)}{3} \quad (15)$$

$$d = \left(1 - \frac{\tan \beta}{3}\right) f'_{cc} \quad (16)$$

$$t = \frac{q}{2} \left[ 1 + \frac{1}{k} - \left(1 - \frac{1}{k}\right) \left(\frac{r}{q}\right)^3 \right] \quad (17)$$

$$r = \left[ \frac{9}{2} (S_1^3 + S_2^3 + S_3^3) \right]^{\frac{1}{3}} \quad (18)$$

and  $S_1$ ,  $S_2$ , and  $S_3$  are principal stress deviators. The material angle of friction ( $\beta$ ) and the ratio of flow stress in triaxial tension to that in compression ( $K$ ) are determined from experimental data.  $K=1$  and  $\beta = 20^\circ$  are used.

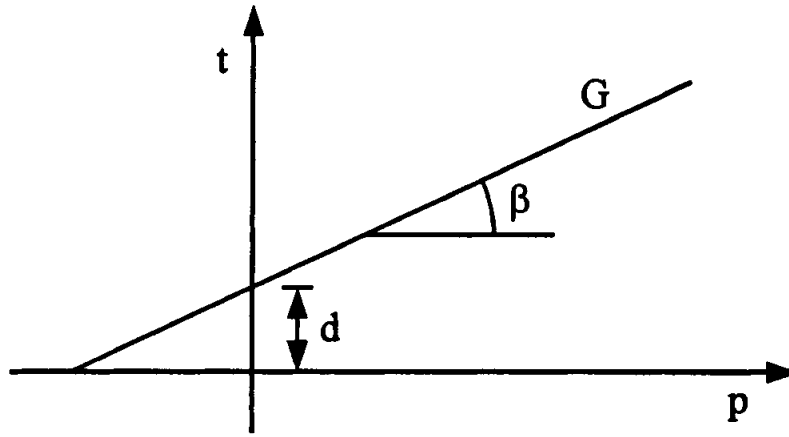


Figure 4.81: Linear Drucker-Prager yield criterion for concrete [30]

The flow stress ratio ( $\gamma$  or  $k$ ) defines the deviation shape of the stress plane and, similarly, the confinement angle of concrete. When the deviation plane is nearly triangular, the confinement degree is lower, whereas when the plane is more circular, a higher confinement level is considered. This parameter is calculated from the following relationships, where  $J_2$  represents the second invariant of the deviatoric stress tensor. In this formulation, the parameter  $\gamma$  is typically defined between 1 and 2.3, but some researchers suggest a maximum value of 0.8.

$$\gamma = \frac{3(1-\rho)}{2\rho+3} \quad (19)$$

$$\rho = \frac{(\sqrt{J_2})_{TM}}{(\sqrt{J_2})_{CM}} \quad (20)$$

The figure 4.82 represents a yield surface in principal stress space ( $S_1, S_2, S_3$ ). The equation shown describes a pressure-sensitive yield criterion, which is directly related to confinement effects in materials like concrete, soil, and rock. When  $K=1.0$  (curve a), the yield surface becomes spherical, similar to the von Mises criterion, which assumes no pressure dependence. When  $K=0.8$  (curve b) accounts for pressure-dependent yielding, meaning confinement significantly increases the material strength. When concrete confinement is negligible, we use  $K=1$  since pressure effects are minimal.

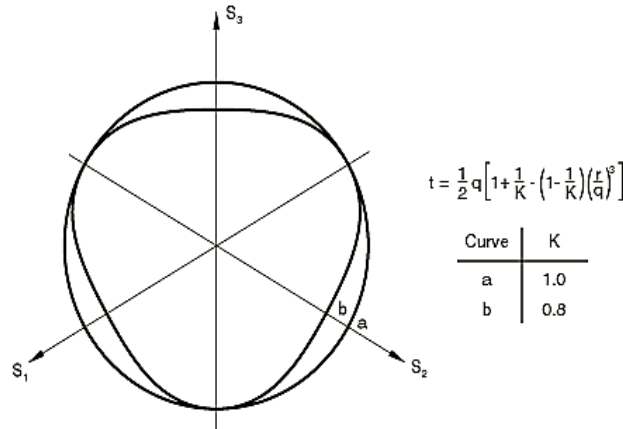


Figure 4.82: stress plane deviation shape for different values of  $K$

The dilation angle ( $\psi$ ) represents the plastic volumetric expansion angle, which occurs due to shear deformation in the post-elastic phase. If  $\psi = 0$ , the material undergoes no volumetric change during shear. In reality, the dilation angle defines the relationship between volumetric strain and shear strain as given by the following equation:

$$\psi = \frac{-(\delta\varepsilon_v)}{(\delta\gamma)} \quad (21)$$

Based on the findings of Vermeer de Borst, hydrostatic pressure-dependent materials such as soil, rock, and concrete exhibit dilation angles greater than their internal friction angle and typically

ranges between  $0^\circ$  and  $20^\circ$  (e.g., for normal concrete is  $12^\circ$ ). The smaller the dilation angle, the brittle the material behaves, whereas larger dilation angles indicate a more ductile behavior similar to shape-adaptive materials.

#### 4.4 Uniaxial Compressive Behavior

concrete-filled steel sections with a small value of the width to thickness ratio provide remarkable confinement for the concrete and the concrete strength is considerably improved and the confined concrete model can be taken as the concrete model. Fig. 4.83 shows equivalent uniaxial presentations for the stress–strain curves of unconfined and confined concrete, where  $f_c$  is the unconfined concrete cylinder compressive strength which is equal to  $0.8f_{cu}$  and  $f_{cu}$  is the unconfined concrete cube compressive strength. The value of  $\varepsilon_c$  is usually around the range of 0.002 to 0.003. A representative value suggested by ACI Committee 318 (1999) and used in the analysis is  $\varepsilon_c$  equal to 0.003. The confined concrete compressive strength  $f_{cc}$  and the corresponding confined strain  $\varepsilon_{cc}$  can be determined from Eqs. (20) and (21), respectively, proposed by Mander et al [28].

$$f_{cc} = f_c + k_1 f_l \quad (22)$$

$$\varepsilon_{cc} = \varepsilon_c \left( 1 + k_2 \frac{f_l}{f_c} \right) \quad (23)$$

$k_1$  is an effectiveness coefficient able to take the shape effect

into account as given by Richart et al. [29] and expressed by:

$$k_1 = 6.779 - 2.645 \frac{a}{b} \quad (24)$$

$$k_2 = 5k_1 \quad (25)$$

where  $f_l$  is the lateral confining pressure imposed by the steel tube. The lateral confining pressure  $f_l$  depends on the sectional shape, width to thickness ratio ( $B/t$  or  $D/t$ ) and the steel tube yield stress  $f_y$ . In our case, due to the specific geometry of folded flange beam that is octahedral cross-section, the distribution of the lateral confining pressures will not be uniform.

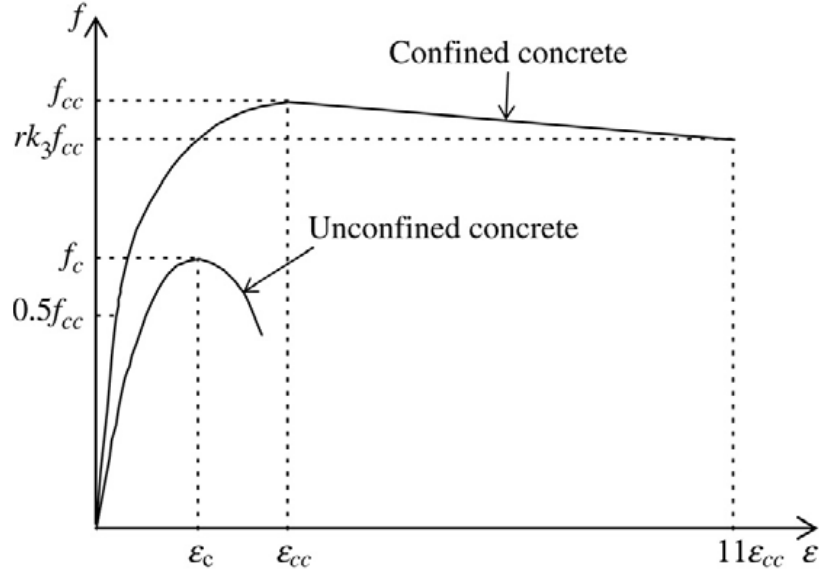


Figure 4.83: Equivalent uniaxial stress-strain curves for confined and unconfined

The experimental results highlight the fact that the effectiveness of the confinement diminishes as the aspect ratio (i.e., the ratio between the lengths of the major and minor axes of the section) increases and becomes insignificant (irrespective of the amount of lateral confinement) when  $a/b > 2.6$  [30][31]. In our case, this ratio is  $a/b = 3.53$ , which clearly exceeds the critical threshold. This suggests that the lateral confinement provided is largely ineffective in enhancing the structural performance or ductility of the section. Consequently, the expected confinement-related benefits, such as increased load-carrying capacity or energy dissipation, are likely to be minimal.

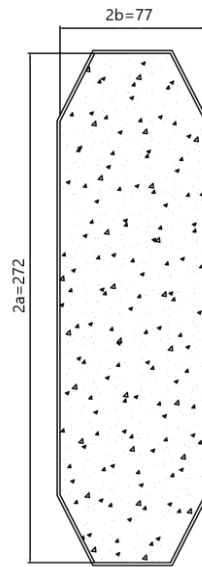


Figure 4.84: geometry of folded flange beam

### Uniaxial compressive behavior

For concrete material Generally, uniaxial compressive behavior could be characterized by either experimental tests or existing constitutive models. In the present study, the Stress-strain relation for non-linear structural analysis according to Eurocode2 was utilized, the relation between  $\sigma_c$  and  $\varepsilon_c$  shown in Figure 4.85 (compressive stress and shortening strain shown as absolute values) for short term uniaxial loading is described by the Expression [32]:

$$\sigma_c = f_{cm} \left( \frac{k\eta - \eta^2}{1 + (k-2)\eta} \right) \quad (26)$$

Where:

$$\eta = \frac{\varepsilon_c}{\varepsilon_{c1}} \quad (27)$$

$\varepsilon_{c1}$  is the strain at peak stress according to Table 3.1

$k = 1.05 E_{cm} \times |\varepsilon_{c1}| / f_{cm}$  ( $f_{cm}$  according to Table 3.1)

Expression (24) is valid for  $0 < |\varepsilon_c| < |\varepsilon_{cu1}|$  where  $\varepsilon_{cu1}$  is the nominal ultimate strain.

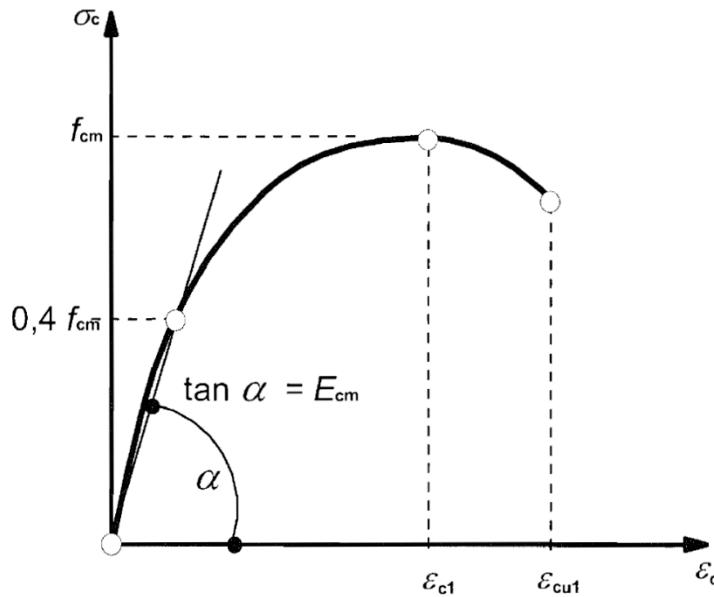


Figure 4.85: Schematic representation of the stress-strain relation for structural analysis (the use  $0.4f_{cm}$  for the definition of  $E_{cm}$  is approximate). [32]



For both normal-strength (NSC) and high-strength (HSC) concrete, the Comité Euro-International du Béton and the Fédération Internationale de la Précontrainte (CEB-FIP) Model Code and Euro code 2 suggest that the approximate value of secant modulus  $E_{cm}$  of concrete with quartzite aggregates can be obtained from the mean compressive strength  $f_{cm}$  as below:

$$E_{cm} = 22\alpha \left( \frac{f_{cm}}{10} \right)^{0.3} GPa \quad (28)$$

$$f_{cm} = f_{ck} + 8 MPa \quad (29)$$

Where  $f_{cm} = f_{ck} + 8 MPa$ , and  $f_{ck}$  is the cylinder compressive strength of concrete. The coefficient  $\alpha$  present only in the CEB-FIP Model code has a value of 1.2 for basalt and dense limestone, 1.0 for quartzite, 0.9 for limestone, and 0.7 for sandstone aggregates. When lightweight aggregates are used, the CEB-FIP equation was found to overestimate the modulus, and the calculated values decreased when coarse aggregate such as crushed quartzite, crushed limestone, and calcined bauxite was used (Vakhshouri and Nejadi, 2019).

Table 9: strength and deformation characteristics for concrete [32]

| Strength classes for concrete |      |     |     |     |     |      |     |     |      |      |     |      |     |     | Analytical relation / Explanation   |
|-------------------------------|------|-----|-----|-----|-----|------|-----|-----|------|------|-----|------|-----|-----|---|
| $f_{ck}$ (MPa)                | 12   | 16  | 20  | 25  | 30  | 35   | 40  | 45  | 50   | 55   | 60  | 70   | 80  | 90  |   |
| $f_{ck,cube}$ (MPa)           | 15   | 20  | 25  | 30  | 37  | 45   | 50  | 55  | 60   | 67   | 75  | 85   | 95  | 105 | 2.8   |
| $f_{cm}$ (MPa)                | 20   | 24  | 28  | 33  | 38  | 43   | 48  | 53  | 58   | 63   | 68  | 78   | 88  | 98  | $f_{cm} = f_{ck} + 8$ (MPa)   |
| $f_{ctm}$ (MPa)               | 1,6  | 1,9 | 2,2 | 2,6 | 2,9 | 3,2  | 3,5 | 3,8 | 4,1  | 4,2  | 4,4 | 4,6  | 4,8 | 5,0 | $f_{ctm} = 0,30 \times f_{ck}^{(2/3)} \leq C50/60$<br>$f_{ctm} = 2,12 \cdot \ln(1 + (f_{cm}/10)) > C50/60$  |
| $f_{ctk,0,05}$ (MPa)          | 1,1  | 1,3 | 1,5 | 1,8 | 2,0 | 2,2  | 2,5 | 2,7 | 2,9  | 3,0  | 3,1 | 3,2  | 3,4 | 3,5 | $f_{ctk,0,05} = 0,7 \times f_{ctm}$<br>5% fractile  |
| $f_{ctk,0,95}$ (MPa)          | 2,0  | 2,5 | 2,9 | 3,3 | 3,8 | 4,2  | 4,6 | 4,9 | 5,3  | 5,5  | 5,7 | 6,0  | 6,3 | 6,6 | $f_{ctk,0,95} = 1,3 \times f_{ctm}$<br>95% fractile   |
| $E_{cm}$ (GPa)                | 27   | 29  | 30  | 31  | 33  | 34   | 35  | 36  | 37   | 38   | 39  | 41   | 42  | 44  | $E_{cm} = 22[(f_{cm})/10]^{0,3}$<br>( $f_{cm}$ in MPa)  |
| $\varepsilon_{c1}$ (‰)        | 1,8  | 1,9 | 2,0 | 2,1 | 2,2 | 2,25 | 2,3 | 2,4 | 2,45 | 2,5  | 2,6 | 2,7  | 2,8 | 2,8 | see Figure 3.2<br>$\varepsilon_{c1}^{(0)}/\varepsilon_{c1}^{(0)}/\varepsilon_{c1}^{(0)} = 0,7 f_{cm}^{0,31} \leq 2,8$ (‰)                               |
| $\varepsilon_{cu1}$ (‰)       | 3,5  |     |     |     |     |      |     |     |      | 3,2  | 3,0 | 2,8  | 2,8 | 2,8 | see Figure 3.2<br>for $f_{ck} \geq 50$ Mpa<br>$\varepsilon_{cu1}^{(0)}/\varepsilon_{cu1}^{(0)}/\varepsilon_{cu1}^{(0)} = 2,8 + 27[(98 - f_{ck})/100]^4$ |
| $\varepsilon_{c2}$ (‰)        | 2,0  |     |     |     |     |      |     |     |      | 2,2  | 2,3 | 2,4  | 2,5 | 2,6 | see Figure 3.3<br>for $f_{ck} \geq 50$ Mpa<br>$\varepsilon_{c2}^{(0)}/\varepsilon_{c2}^{(0)}/\varepsilon_{c2}^{(0)} = 2,0 + 0,085(f_{ck} - 50)^{0,53}$  |
| $\varepsilon_{cu2}$ (‰)       | 3,5  |     |     |     |     |      |     |     |      | 3,1  | 2,9 | 2,7  | 2,6 | 2,6 | see Figure 3.3<br>for $f_{ck} \geq 50$ Mpa<br>$\varepsilon_{cu2}^{(0)}/\varepsilon_{cu2}^{(0)}/\varepsilon_{cu2}^{(0)} = 2,6 + 35[(90 - f_{ck})/100]^4$ |
| $n$                           | 2,0  |     |     |     |     |      |     |     |      | 1,75 | 1,6 | 1,45 | 1,4 | 1,4 | for $f_{ck} \geq 50$ Mpa<br>$n = 1,4 + 23,4[(90 - f_{ck})/100]^4$   |
| $\varepsilon_{c3}$ (‰)        | 1,75 |     |     |     |     |      |     |     |      | 1,8  | 1,9 | 2,0  | 2,2 | 2,3 | see Figure 3.4<br>for $f_{ck} \geq 50$ Mpa<br>$\varepsilon_{c3}^{(0)}/\varepsilon_{c3}^{(0)}/\varepsilon_{c3}^{(0)} = 1,75 + 0,55[(f_{ck} - 50)/40]$    |
| $\varepsilon_{cu3}$ (‰)       | 3,5  |     |     |     |     |      |     |     |      | 3,1  | 2,9 | 2,7  | 2,6 | 2,6 | see Figure 3.4<br>for $f_{ck} \geq 50$ Mpa<br>$\varepsilon_{cu3}^{(0)}/\varepsilon_{cu3}^{(0)}/\varepsilon_{cu3}^{(0)} = 2,6 + 35[(90 - f_{ck})/100]^4$ |

## 4.5 Uniaxial Tensile Behavior

Concrete is a quasi-brittle material that exhibits distinct behavior under tensile loading compared to compressive loading. While concrete has relatively high compressive strength, its tensile strength is much lower, typically ranging between 7% and 10% of its compressive strength. The Eurocode 2 (EC2) provides guidelines for estimating the uniaxial tensile strength and describes the stress-strain response for structural design and numerical modeling. According to EN 1992-1-1, the mean axial tensile strength of concrete ( $f_{ctm}$ ) is expressed as a function of its characteristic compressive strength ( $f_{ck}$ ) using the empirical formula:

$$f_{ctm} = 0.3 \times f_{ck}^{(2/3)} \quad (30)$$

The stress-strain response of concrete under uniaxial tension can be divided into three phases: pre-cracking (elastic phase), softening (post-peak phase), and post-failure (fully cracked phase). In the pre-cracking phase, concrete behaves elastically, following Hooke's Law up to its peak tensile strength ( $f_{ctm}$ ), with stress increasing proportionally to strain according to the equation  $\sigma_t = E_{cm} \cdot \varepsilon_t$ , where  $E_{cm}$  is the modulus of elasticity. Once concrete reaches its tensile strength limit, it begins to crack, marking the transition into the softening phase. The stress in this phase gradually reduces as strain increases, leading to complete tensile failure at an ultimate tensile strain ( $\varepsilon_u$ ), where stress approaches zero, however in this study, 1% of the tensile strength was considered during the analysis regardless of the realistic condition to prevent numerical instability. In contrast, correspondence strain value, where stress is 1% of the ultimate tensile strength, was taken as 10 times the percentage of the strain, in which stress was equal to ultimate tensile strength as suggested by Hafezolghorani [40].

## 4.6 Concrete Test Modeling: Compression, Tension, and Bending

For the compressive, tensile, and three-point bending test simulations, the numerical analyses encountered convergence issues when using the Static General (Abaqus/Standard) solver. These challenges were primarily due to the nonlinear behavior associated with plasticity and material damage within the concrete. To address these issues, the Abaqus/Explicit solver was adopted. Although primarily designed for dynamic analyses, this solver is widely accepted in both literature and official documentation for quasi-static simulations involving complex nonlinear effects. As stated in the Abaqus documentation [36]:

*“The explicit dynamics procedure is typically used to solve two classes of problems: transient dynamic response calculations and quasi-static simulations involving complex nonlinear effects (most commonly problems involving complex contact conditions).”*

### 4.6.1 Uniaxial Compressive Test

To validate the concrete material models adopted in this study, a series of uniaxial compression simulations were conducted on a standard 150 mm × 300 mm cylindrical specimen representing C40 concrete, in accordance with Eurocode 2 provisions. Both the Concrete Damaged Plasticity (CDP) model and the Drucker–Prager (DP) model were tested using two mesh sizes: 20 mm and 40 mm. The goal was to assess the accuracy, mesh sensitivity, and post-peak behavior of each

model. The simulated results, specifically the peak compressive stress and corresponding strain values, were compared against the reference values provided by Eurocode 2 for C40 concrete, where the mean compressive strength  $f_{cm} = 48$  MPa and the strain at peak stress  $\epsilon_{c1} = 0.0022$ . This allowed for validation of the implemented material models against standardized benchmarks for both strength and deformation capacity.

### **Concrete Damaged Plasticity (CDP) Model**

As shown in Figure 4.86, the CDP model effectively captures the typical stress–strain behavior of unconfined concrete under compression, including the linear elastic phase, nonlinear hardening, peak strength, and post-peak softening. The simulation with a 20 mm mesh reached a peak compressive stress of approximately 42 MPa at a strain of around 0.0021, which aligns closely with the Eurocode 2 reference value of  $\epsilon_{c1} = 0.0022$  for C40 concrete. The 40 mm mesh yielded a slightly lower peak stress of about 39 MPa, along with a more gradual softening response. While both mesh sizes replicated the general curve shape well, the post-peak region exhibited pronounced mesh sensitivity. The finer mesh displayed sharper strain localization and more abrupt degradation, consistent with the behavior expected in damage-based material formulations. These findings underscore the CDP model’s capability to simulate realistic concrete degradation and stiffness loss, while also highlighting the need for mesh refinement in regions of high stress gradients to avoid artificial energy dissipation or premature failure localization.

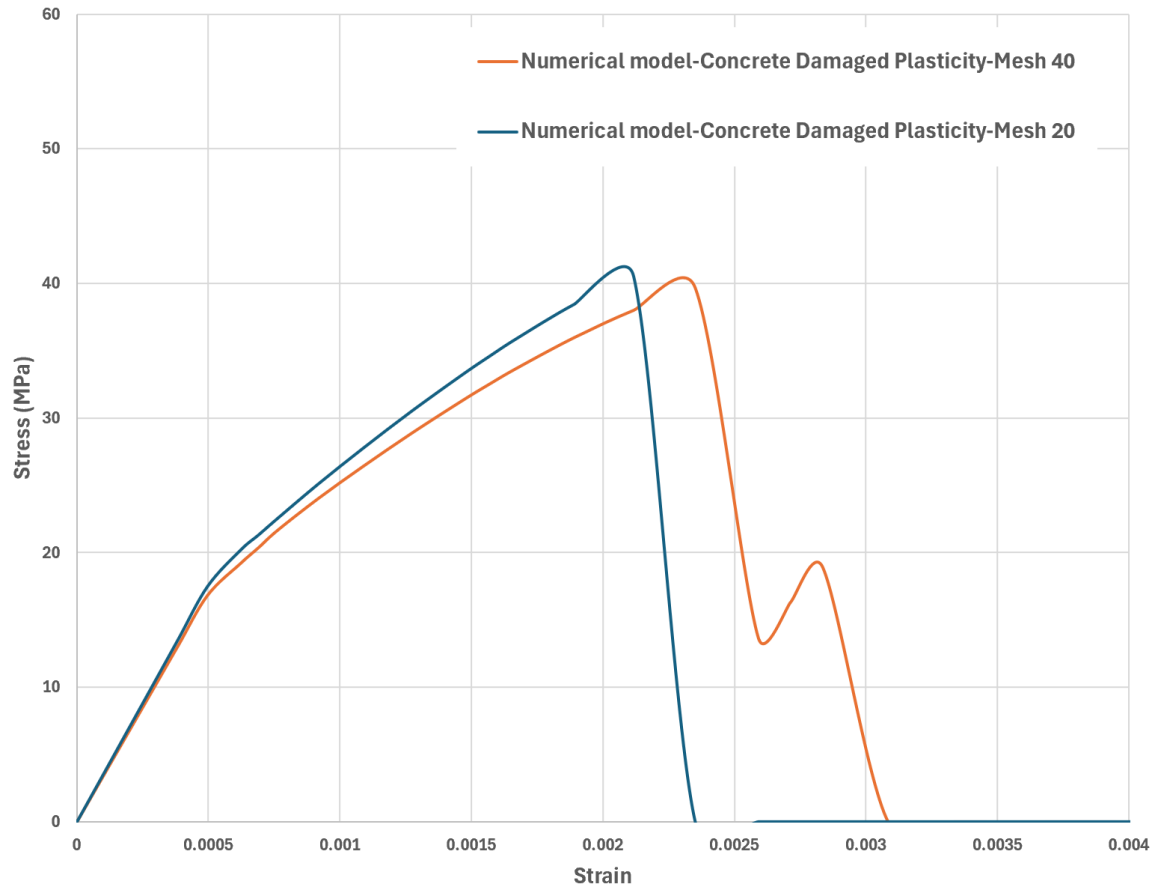


Figure 4.86: Stress–strain curves for C40 concrete cylinder using the CDP model with 20 mm and 40 mm mesh sizes (compressive test)

### Drucker–Prager (DP) Model

Figure 4.87 presents the stress–strain response of the same 150 mm × 300 mm concrete cylinder modeled using the Drucker–Prager plasticity model. Similar to the CDP model, both mesh sizes accurately captured the initial linear elastic behavior and peak compressive strength. The finer 20 mm mesh reached a peak stress of approximately 45 MPa, while the 40 mm mesh peaked around 43 MPa, both slightly underestimating the Eurocode 2 mean compressive strength for C40 concrete ( $f_{cm} = 48$  MPa). The post-peak softening response in the DP model was smoother and more gradual compared to CDP, and the results demonstrated less sensitivity to mesh size. However, the DP model showed a residual stress plateau beyond the peak, which is not fully representative of the brittle failure typically observed in unconfined concrete cylinders. This behavior stems from the fact that the standard Drucker–Prager model lacks an explicit damage mechanism and thus tends to overpredict the load-carrying capacity after peak, unless calibrated

with additional softening or damage criteria. Therefore, while the DP model is computationally stable and mesh-insensitive, it may not accurately capture the post-peak degradation and localization behavior critical in simulating concrete failure under seismic or collapse scenarios.

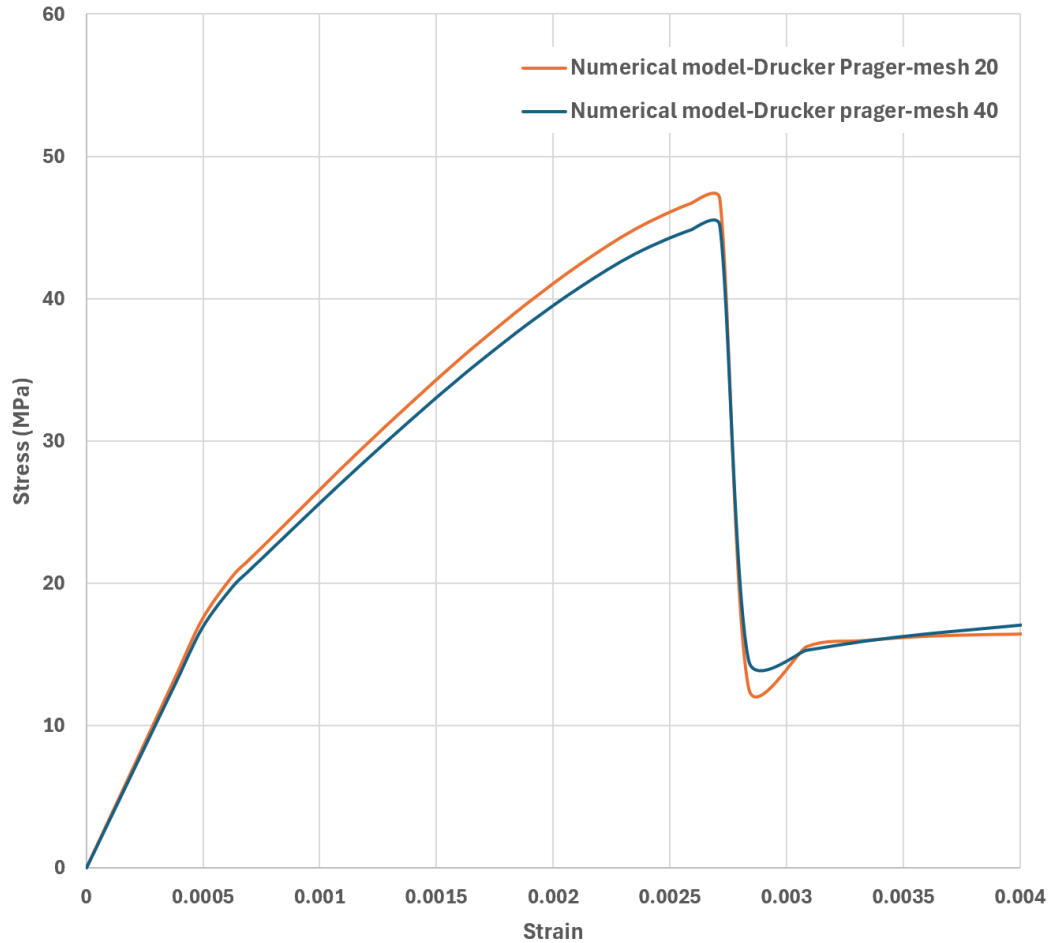


Figure 87: Stress–strain curves for C40 concrete cylinder using the DP model with 20 mm and 40 mm mesh sizes (compressive test)

#### 4.6.2 Uniaxial Tensile Test

In this study, the tensile behavior of concrete was investigated through numerical simulations using the Concrete Damaged Plasticity (CDP) and Drucker–Prager (DP) models within ABAQUS. A standard cylindrical specimen (150 mm diameter  $\times$  300 mm height) was modeled, and the material properties were defined according to Eurocode 2 for C40 concrete, with a mean compressive strength  $f_{cm} = 48$  MPa and a mean tensile strength  $f_{ctm} = 3.5$  MPa.

Both material models were tested using two mesh sizes (20 mm and 40 mm) to evaluate mesh sensitivity as shown in figure 4.88. Figures 4.89 and 4.90 illustrate the corresponding stress–strain responses. The CDP model showed peak tensile stresses of approximately 3.4 MPa, aligning well with the Eurocode value. The finer mesh (20 mm) produced sharper strain localization and more abrupt post-peak softening, reflecting the mesh-dependent nature of damage evolution. In contrast, the coarser mesh (40 mm) yielded smoother softening curves.

Similarly, the DP model also achieved peak tensile stresses in the range of 3.3–3.4 MPa. However, unlike CDP, the post-peak response in DP was more gradual and showed residual strength retention, particularly with the 40 mm mesh. This behavior highlights the absence of an internal damage mechanism in the standard DP formulation, which may lead to non-physical softening behavior unless calibrated or extended with fracture energy control.

The comparison between the two models confirms that while both can approximate the peak tensile strength of concrete, CDP provides a more realistic representation of cracking and stiffness degradation under tensile loading, especially when sufficient mesh refinement is applied. The DP model, on the other hand, remains computationally efficient but may overestimate post-peak capacity in tension unless enhanced with softening regularization or damage coupling.

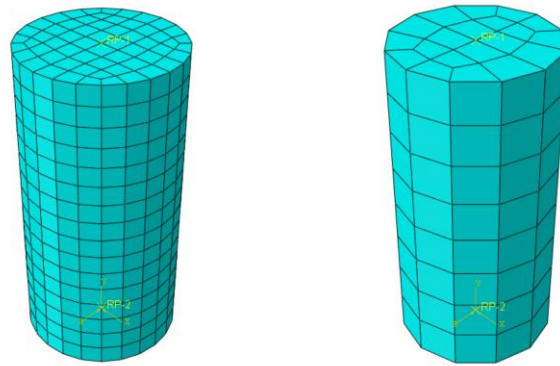


Figure 4.88: cylindrical mesh sizes 20mm and 40 mm from left to right respectively.

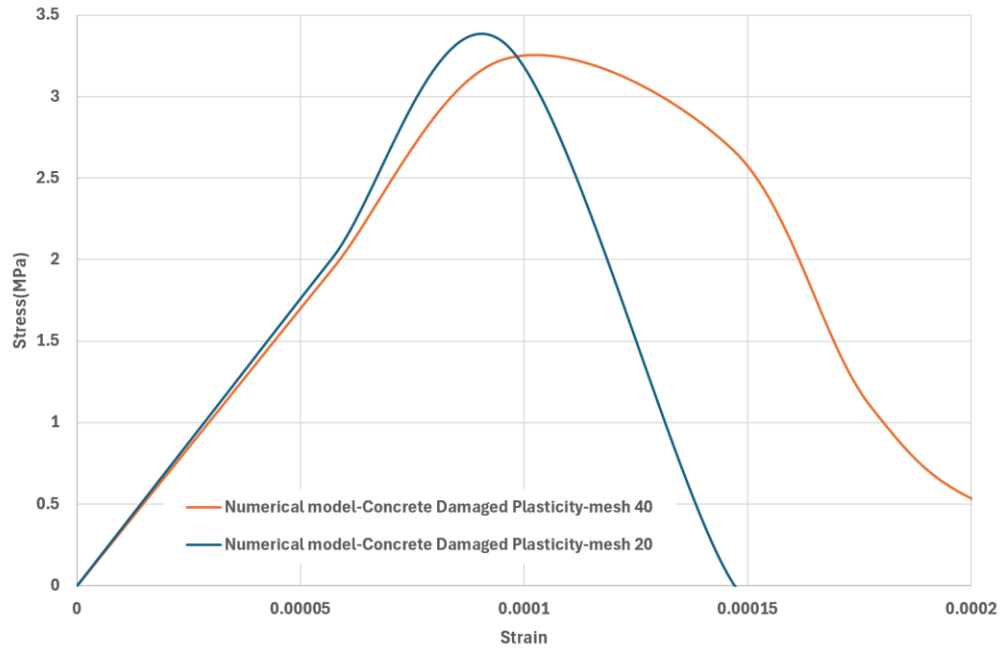


Figure 4.89: Stress–strain curves for C40 concrete cylinder using the CDP model with 20 mm and 40 mm mesh sizes (tensile test)

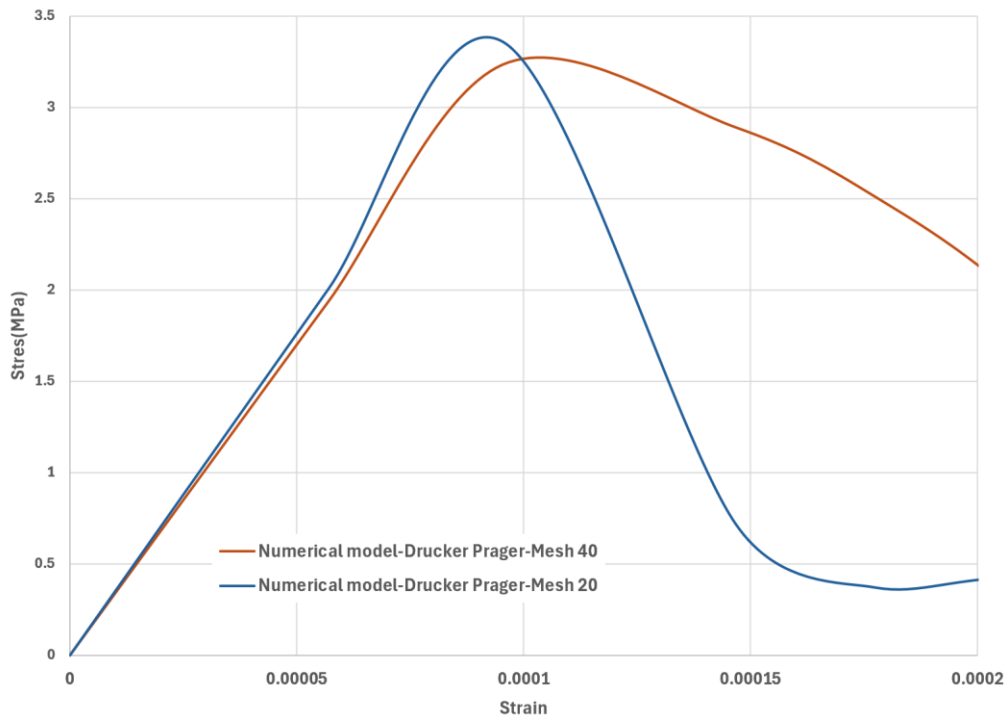


Figure 4.90: Stress–strain curves for C40 concrete cylinder using the DP model with 20 mm and 40 mm mesh sizes (tensile test)



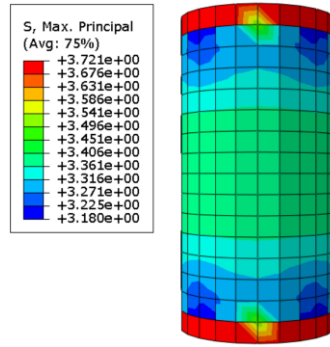


Figure 4.91: Plot of Maximum Principal Stress Distribution Numerical model (DP) of a cylinder under uniaxial tensile loading, Mesh 20mm

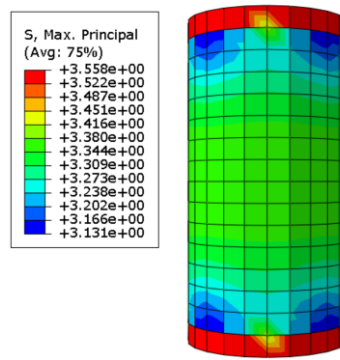


Figure 4.92: Plot of Maximum Principal Stress Distribution Numerical model (CDP) of a cylinder under uniaxial tensile loading, Mesh 20mm

### 4.6.3 Three-Point Bending Test

To further validate the adopted concrete material model and simulation strategy, a three-point bending test was simulated in Abaqus/Explicit and compared against experimental results from the literature. The verification focused on the configuration without a notch (referred to as "No Slot – Large Beam") to isolate the material response from fracture initiation effects.

#### Experimental Setup

The reference experimental study, conducted by J. Davies at the University of Glamorgan, investigated the fracture behavior of mortar beam specimens under three-point bending conditions [41]. The test setup involved concrete beams with dimensions 100 mm × 100 mm × 250 mm, simply supported over a 200 mm span and subjected to a central point load. The reported compressive strength was 38 MPa, and loading was applied at a constant displacement rate of 0.003 mm/sec. Load-deflection data was captured to characterize the mechanical behavior.

### **Numerical Model (Abaqus/Explicit)**

To replicate the experimental configuration, a numerical model was developed in Abaqus/Explicit. The beam geometry and support conditions were modeled precisely, with rigid cylindrical rollers used at the supports and load point. The concrete was defined using the Concrete Damaged Plasticity (CDP) model, with material parameters corresponding to C40 concrete according to Eurocode 2, closely matching the experimental strength. A mesh size of 50 mm was adopted to reduce computational cost and simplify the analysis, while still capturing the overall structural response. The simulation was carried out under displacement-controlled loading up to  $-0.5$  mm vertical displacement, with a total simulation time of 166 seconds, maintaining the same loading rate as the experiment (0.003 mm/sec).

### **Comparison and Results**

Figure 4.93 compares the numerical load-deflection curve (orange line) with the experimental data for the "No Slot – Large Beam" case. The model shows a strong correlation in the initial stiffness and peak load, validating the accuracy of the concrete material parameters and mesh choice. The post-peak softening trend is also captured, though with some deviation likely due to mesh coarseness and rate sensitivity in dynamic simulation.

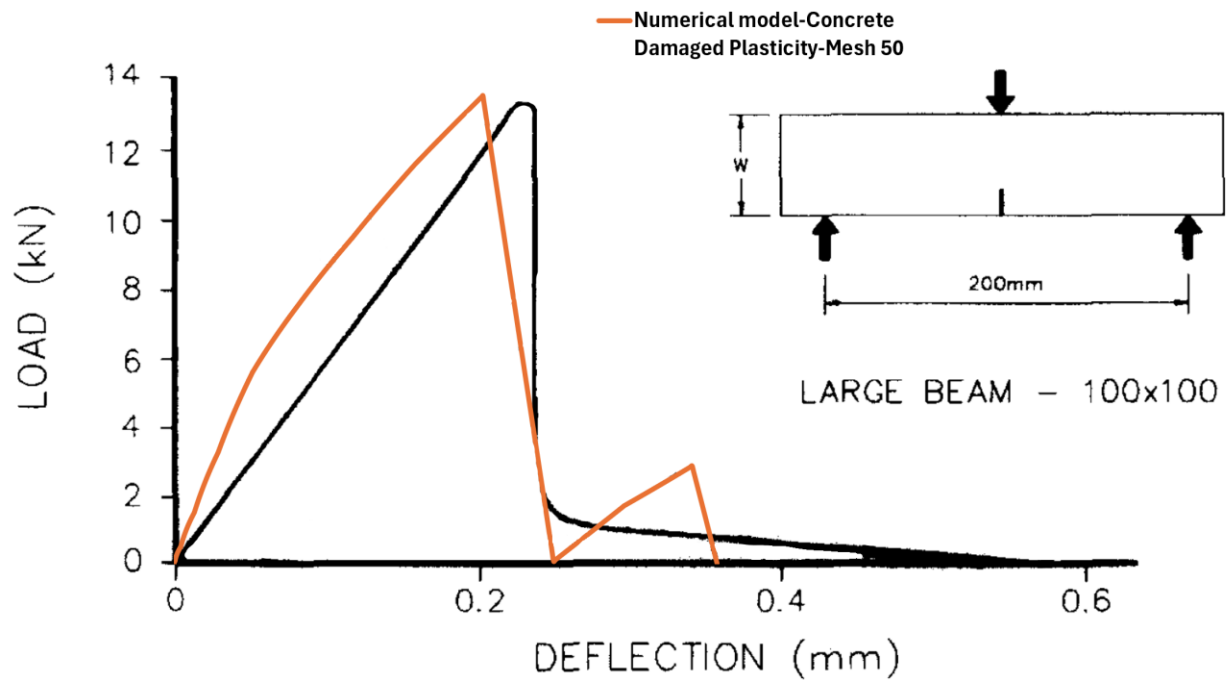


Figure 4.93: Comparison of Numerical (CDP) and Experimental Load-Deflection Curves under Three-Point Bending.

Figure 4.94 presents the numerical load–deflection response obtained using the Drucker-Prager material model (green curve) with a mesh size of 50, compared against the experimental data for the "No Slot – Large Beam" configuration. The Drucker-Prager model demonstrates accurate stiffness and peak load prediction, aligning well with the experimental curve in the pre-peak phase. One notable advantage of this model is the more ductile post-peak response, which smoothens the softening behavior typically observed in quasi-brittle materials like concrete. However, a limitation arises in the overestimation of the residual load, likely due to the model's inability to fully capture damage evolution and stiffness degradation beyond the peak, resulting in an overly optimistic representation of the structure's post-failure capacity.

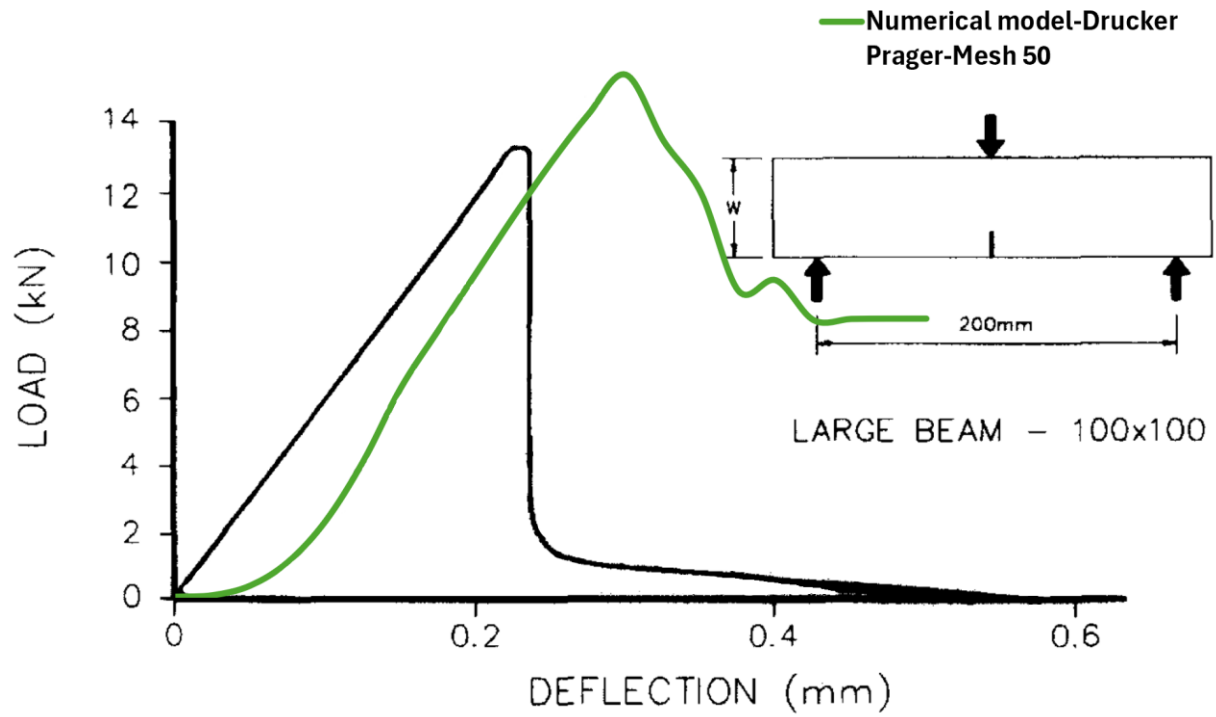


Figure 4.94: Comparison of Numerical (DP) and Experimental Load-Deflection Curves under Three-Point Bending.

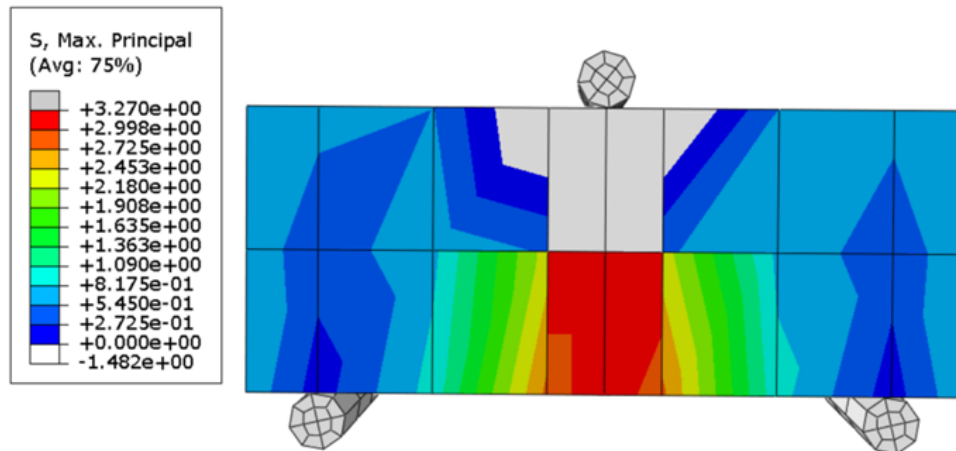


Figure 4.95: Maximum principal stress contour for the mesh 50, CDP Model.

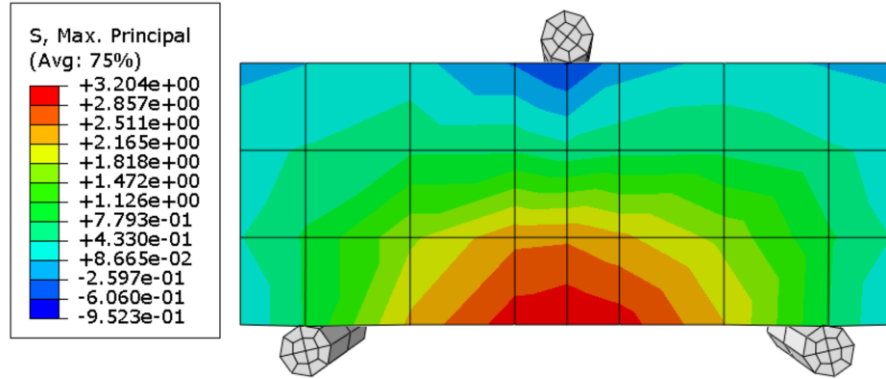


Figure 4.96 : Maximum principal stress contour for the mesh 50, DP Model

As shown in Figure 4.95, the maximum principal stress over time at this critical point was extracted from the Abaqus simulation. The plot reveals that the stress gradually increases and reaches a peak of approximately 3.27 MPa at around 49.8 seconds. After this point, a noticeable stress drop occurs, indicating the onset of tensile cracking and loss of load-carrying capacity. This value correlates well with the theoretical tensile strength of C40 concrete, as defined by Eurocode 2, which estimates the mean tensile strength using:

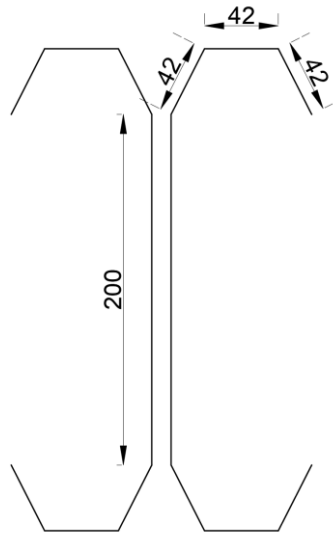
$$f_{ctm} = 0.3 \times f_{ck}^{(2/3)} = 3.5 \text{ MPa for } f_{ck} = 40 \text{ MPa}$$

Furthermore, the corresponding stress contour confirms that the highest tensile stresses are concentrated at the mid-span bottom zone, beneath the applied load. This distribution is consistent with theoretical expectations for flexural stress in three-point bending and visually aligns with typical crack initiation regions observed experimentally.

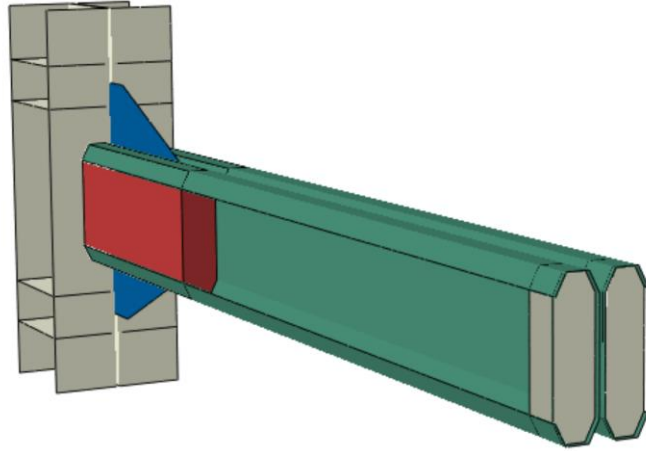
## 4.7 Case Study Description and Modeling Assumptions

### Geometry and Configuration

The studied structural element consists of a cold-formed folded flange beam filled with plain concrete at the connection region. The cross-section of the folded flange, shown in the Figures 4.97 and 4.98, has a total depth of 200 mm, with folded segments forming a symmetrical geometry composed of angled flanges and lips, each measuring 42 mm in width and leg length. The concrete infill is confined within a 600 mm long segment of the folded flange beam adjacent to the joint, where the highest interaction between steel and concrete is expected. This region was specifically selected to evaluate the contribution of the concrete core to the joint's moment resistance and local confinement. The remaining length of the beam beyond the filled region is modeled as hollow and unfilled.



*Figure 4.97: Cross-sectional geometry of the cold-formed folded flange beam used in the numerical model*



*Figure 4.98: Folded flange beam-to-column connection with 600 mm concrete infill at the joint region.*

### **Concrete Material Model**

For the concrete core, the Concrete Damaged Plasticity (CDP) model was used to simulate both compressive crushing and tensile cracking. A C40 concrete class was assumed. The input parameters were chosen based on established literature values as we can see in the table below, appropriate for quasi-static monotonic loading. The uniaxial compressive and tensile behavior was defined via tabulated stress–strain data derived from the material's expected strength class.

| Young's modulus [Mpa] | Poisson's ratio  | Mass density [kg/m3] | Dilation angle     | Eccentricity $\epsilon$ | fbo/fco          | K       | Viscosity parameter |
|-----------------------|------------------|----------------------|--------------------|-------------------------|------------------|---------|---------------------|
| 35220                 | 0.2              | 2.40E-09             | 15                 | 0.1                     | 1.16             | 0.66667 | 0                   |
| Compressive behaviour |                  |                      |                    | Tensile behaviour       |                  |         |                     |
| Yield stress [MPa]    | Inelastic strain | Damage parameter     | Yield stress [MPa] | Cracking strain         | Damage parameter |         |                     |
| 19.2                  | 0                | 0                    | 3.508821286        | 0                       | 0                |         |                     |
| 21.4534727            | 0.0001           | 0                    | 3.254889786        | 0.0008                  | 0.07236946       |         |                     |
| 24.31403599           | 0.0002           | 0                    | 3.000958286        | 0.0016                  | 0.144738919      |         |                     |
| 27.03842412           | 0.0003           | 0                    | 2.747026786        | 0.0024                  | 0.217108379      |         |                     |
| 29.62216933           | 0.0004           | 0                    | 2.493095286        | 0.0032                  | 0.289477838      |         |                     |
| 32.06060628           | 0.0005           | 0                    | 2.239163786        | 0.004                   | 0.361847298      |         |                     |
| 34.34886098           | 0.0006           | 0                    | 1.985232286        | 0.0048                  | 0.434216757      |         |                     |
| 36.48183898           | 0.0007           | 0                    | 1.731300786        | 0.0056                  | 0.506586217      |         |                     |
| 38.45421278           | 0.0008           | 0                    | 1.477369286        | 0.0064                  | 0.578955676      |         |                     |
| 40.26040837           | 0.0009           | 0                    | 1.223437786        | 0.0072                  | 0.651325136      |         |                     |
| 41.89459075           | 0.001            | 0                    | 0.035088213        | 0.008                   | 0.99             |         |                     |
| 43.35064853           | 0.0011           | 0                    | 0.017544106        | 0.01                    | 0.995            |         |                     |
| 44.62217733           | 0.0012           | 0                    |                    |                         |                  |         |                     |
| 45.70246203           | 0.0013           | 0                    |                    |                         |                  |         |                     |
| 46.58445768           | 0.0014           | 0                    |                    |                         |                  |         |                     |
| 47.26076903           | 0.0015           | 0                    |                    |                         |                  |         |                     |
| 47.72362842           | 0.0016           | 0                    |                    |                         |                  |         |                     |
| 47.9648721            | 0.0017           | 0                    |                    |                         |                  |         |                     |
| 48                    | 0.001754862      | 0                    |                    |                         |                  |         |                     |
| 47.88094065           | 0.001854862      | 0.002480403          |                    |                         |                  |         |                     |
| 47.51748728           | 0.001954862      | 0.010052348          |                    |                         |                  |         |                     |
| 46.89984978           | 0.002054862      | 0.022919796          |                    |                         |                  |         |                     |
| 46.01770809           | 0.002154862      | 0.041297748          |                    |                         |                  |         |                     |
| 44.86017581           | 0.002254862      | 0.065413004          |                    |                         |                  |         |                     |
| 43.41576081           | 0.002354862      | 0.095504983          |                    |                         |                  |         |                     |
| 41.67232253           | 0.002454862      | 0.131826614          |                    |                         |                  |         |                     |
| 39.61702556           | 0.002554862      | 0.174645301          |                    |                         |                  |         |                     |
| 37.23628921           | 0.002654862      | 0.224243975          |                    |                         |                  |         |                     |
| 34.51573267           | 0.002754862      | 0.280922236          |                    |                         |                  |         |                     |
| 31.44011513           | 0.002854862      | 0.344997602          |                    |                         |                  |         |                     |
| 27.99327058           | 0.002954862      | 0.416806863          |                    |                         |                  |         |                     |
| 9.6                   | 0.005454862      | 0.8                  |                    |                         |                  |         |                     |



## **Numerical Modeling Setup in Abaqus**

Both Static General and Dynamic Explicit analyses were performed in Abaqus to simulate the structural behavior of the folded flange beams, with and without concrete infill. In the Dynamic Explicit simulations, a displacement of  $-100$  mm was applied. For beams without concrete, the displacement was imposed over 20 seconds, corresponding to a loading rate of  $5$  mm/s. For the concrete-infilled beam, the same displacement was applied over 40 seconds, reducing the loading rate to  $2.5$  mm/s. These rates, being equal to or below  $5$  mm/s, fall within the quasi-static range, effectively minimizing inertial effects and ensuring realistic monotonic response while optimizing computational time, especially for complex nonlinear behavior.

In parallel, Static General simulations were conducted using a larger imposed displacement of  $-150$  mm. This allowed for a broader assessment of post-peak response and facilitated validation of load-bearing capacity across different analysis methods. The dual use of static and dynamic simulations enabled a robust and comprehensive evaluation of the beams' structural performance under monotonic loading.

## **Contact Interaction**

The interaction between the concrete infill and the cold-formed steel beam was a key focus of this study. To investigate its influence on structural response, two contact conditions were modeled. In the full bond configuration, the concrete and steel surfaces were fully tied using the Tie Constraint in Abaqus, which assumes perfect composite action with no relative slip or separation along the interface. In this setup, the steel surface was defined as the master and the concrete as the slave.

## **Mesh Configuration**

The steel components, including the beam, beam-end stiffeners, throughplate, column, and its stiffeners were discretized using S4R shell elements (4-node, reduced integration, with hourglass control). A refined mesh size of  $20 \times 20$  mm was applied in regions with high stress gradients, such as the beam, beam stiffeners, and throughplate, while a coarser mesh of  $40 \times 40$  mm was used for less critical regions like the column and its stiffeners.

For the concrete infill, C3D8R solid elements (8-node linear brick elements with reduced integration) were employed. In the Dynamic Explicit analysis, a coarser mesh of  $50 \times 50$  mm was

used to reduce computational time, whereas in the Static General analysis, a finer mesh of  $30 \times 30$  mm was adopted to improve numerical accuracy. All other components retained the same mesh configuration across both analyses.

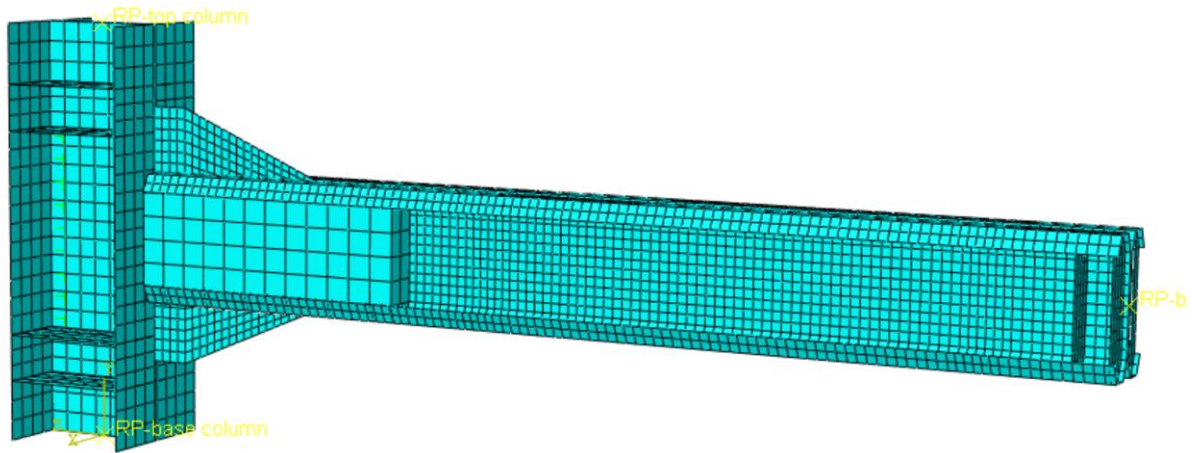


Figure 4.99: Meshed Model of Folded Flange Beam with Concrete Infill In the Dynamic Explicit analysis

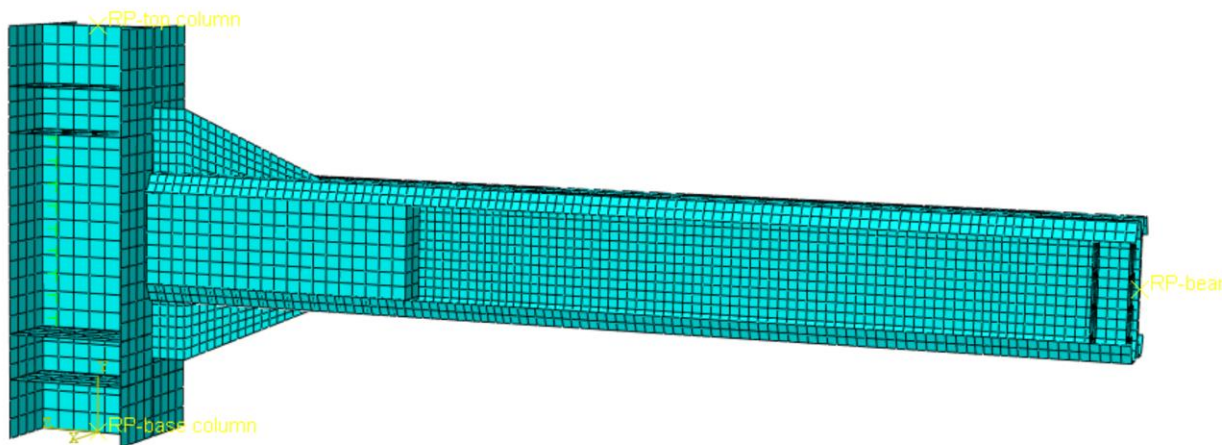


Figure 4.100: Meshed Model of Folded Flange Beam with Concrete Infill In the Static General analysis

# Chapter 5. Result and Numerical Investigation

## 5.1 Overview of Finite Element Models

To investigate the structural behavior of Cold-Formed Steel (CFS) folded flange beams, three finite element models were developed and analyzed using Abaqus as reported in the following:

1. a beam without stiffeners
2. a beam with vertical and horizontal stiffeners, recognized as optimal arrangement by other researchers ... Reference
3. a beam in which the stiffeners were replaced with a plain concrete infill, limiting local instability instead of stiffeners in the connection zone

The interaction between the concrete infill and the CFS beam was modeled using a full bond connection, implemented through the Tie Constraint in Abaqus. This approach assumes perfect composite action, preventing any relative slip or separation at the interface, with the steel surface defined as the master and the concrete as the slave. Also, to model the behavior of concrete material in the third configuration, the Concrete Damaged Plasticity (CDP) model was adopted, allowing for realistic representation of cracking, crushing, and post-peak degradation in the infill region.

Table 10: FEA Models

| FEA Model     | Description  | Bond Description           | Concrete model | Analysis                |
|---------------|--|----------------------------|----------------|-------------------------|
| <b>FFNSS</b>  | <b>FEA Folded Flange – without stiffeners</b>  | -                          | -              | <b>Static-General</b>   |
| <b>FFNSD</b>  | <b>FEA Folded Flange – without stiffeners</b>  | -                          | -              | <b>Dynamic-Explicit</b> |
| <b>FFWSS</b>  | <b>FEA Folded Flange – with (V-H) stiffeners</b>   | -                          | -              | <b>Static-General</b>   |
| <b>FFWSD</b>  | <b>FEA Folded Flange – with (V-H) stiffeners</b>   | -                          | -              | <b>Dynamic-Explicit</b> |
| <b>FFFBES</b> | <b>FEA Folded Flange – Full bond between concrete and steel – Elastic behavior of concrete</b>             | <b>Full Bond (no slip)</b> | <b>Elastic</b> | <b>Static-General</b>   |
| <b>FFFBPD</b> | <b>FEA Folded Flange – Full bond between concrete and steel – Elastic and plastic behavior of concrete</b> | <b>Full Bond (no slip)</b> | <b>CDP</b>     | <b>Dynamic-Explicit</b> |

### (1) a beam without stiffeners

The first simulations focused on a folded flange CFS beam without any stiffeners. This served as the control case to evaluate the baseline performance of the thin-walled section under loading, done through both static and dynamic analysis:

#### FFNSS Model:

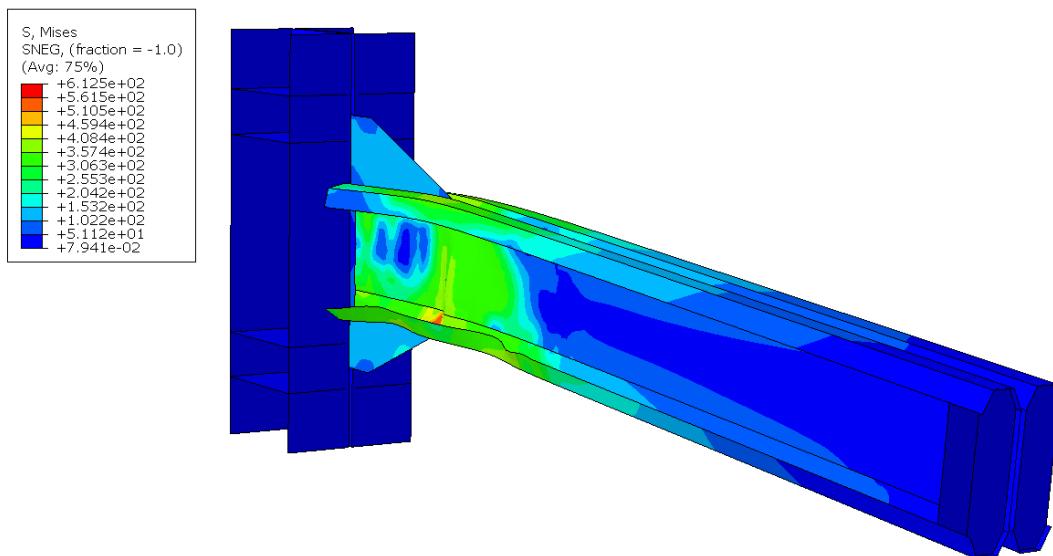


Figure 5.101: Von Mises Stress Contour- FFNSS Model

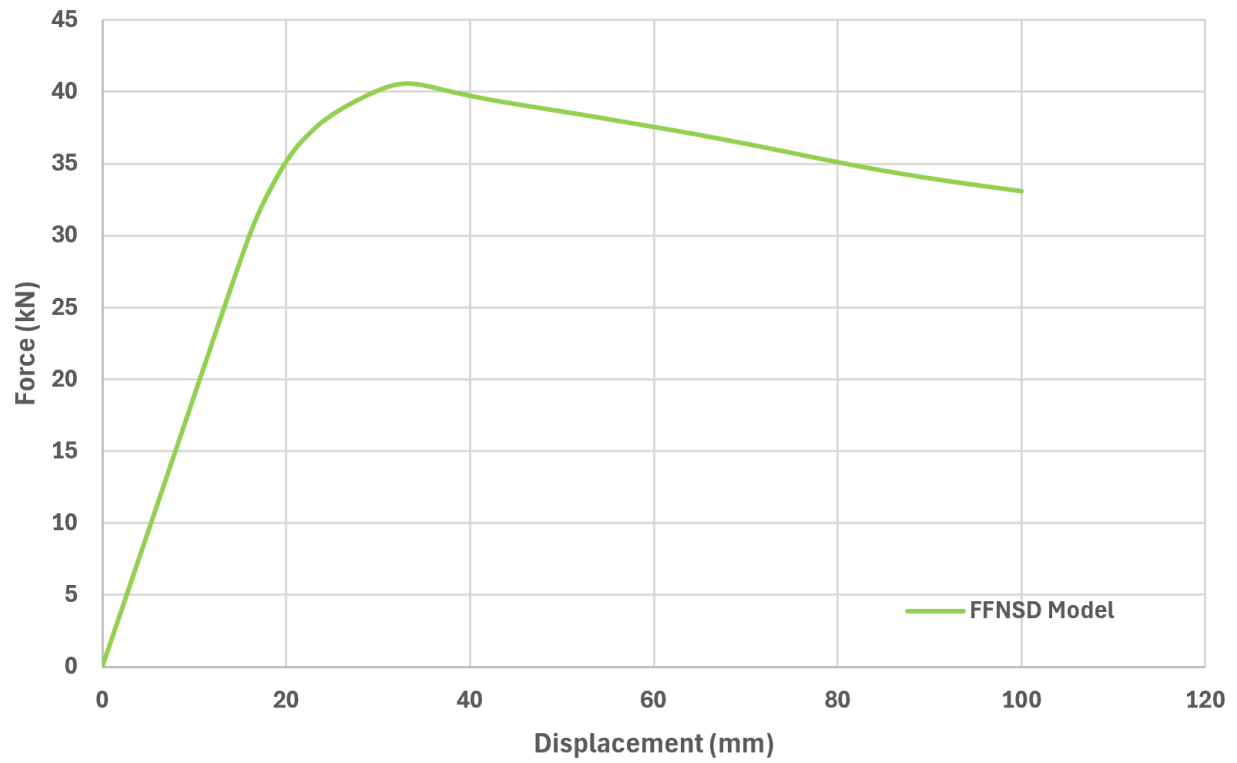


Figure 5.102: Force-Displacement Diagram-FFNSS Model

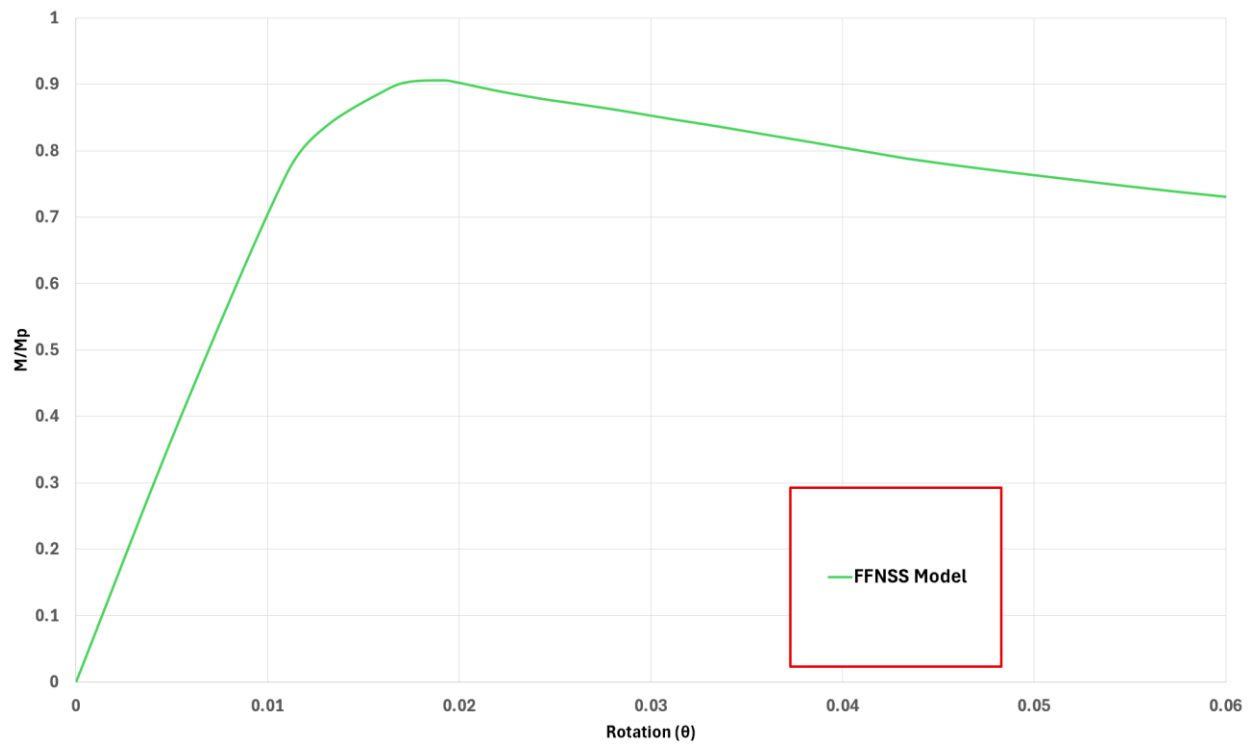


Figure 5.103: Moment-Rotation Diagram-FFNSS Model

### FFNSD Model:

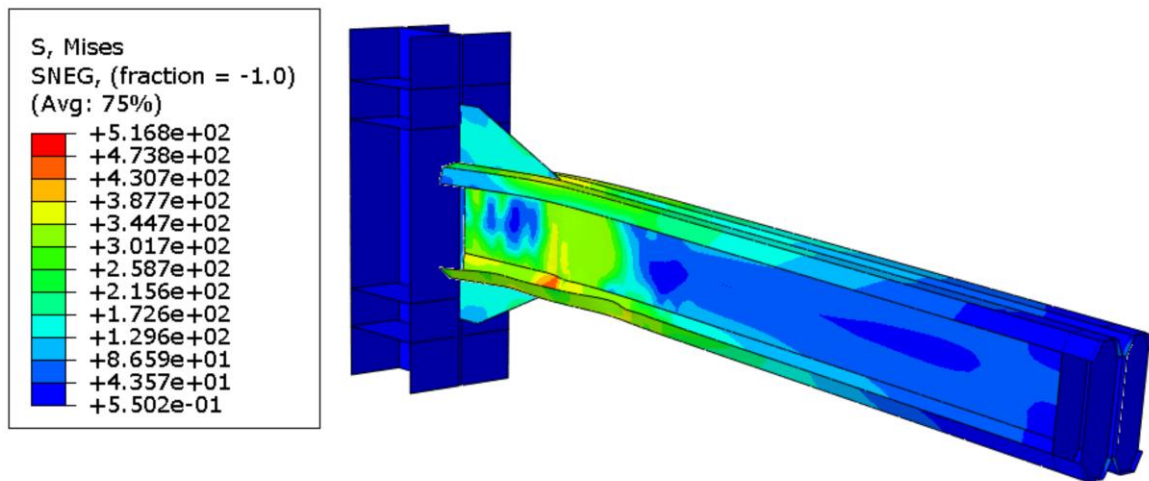


Figure 5.104: Von Mises Stress Contour- FFNSD Model

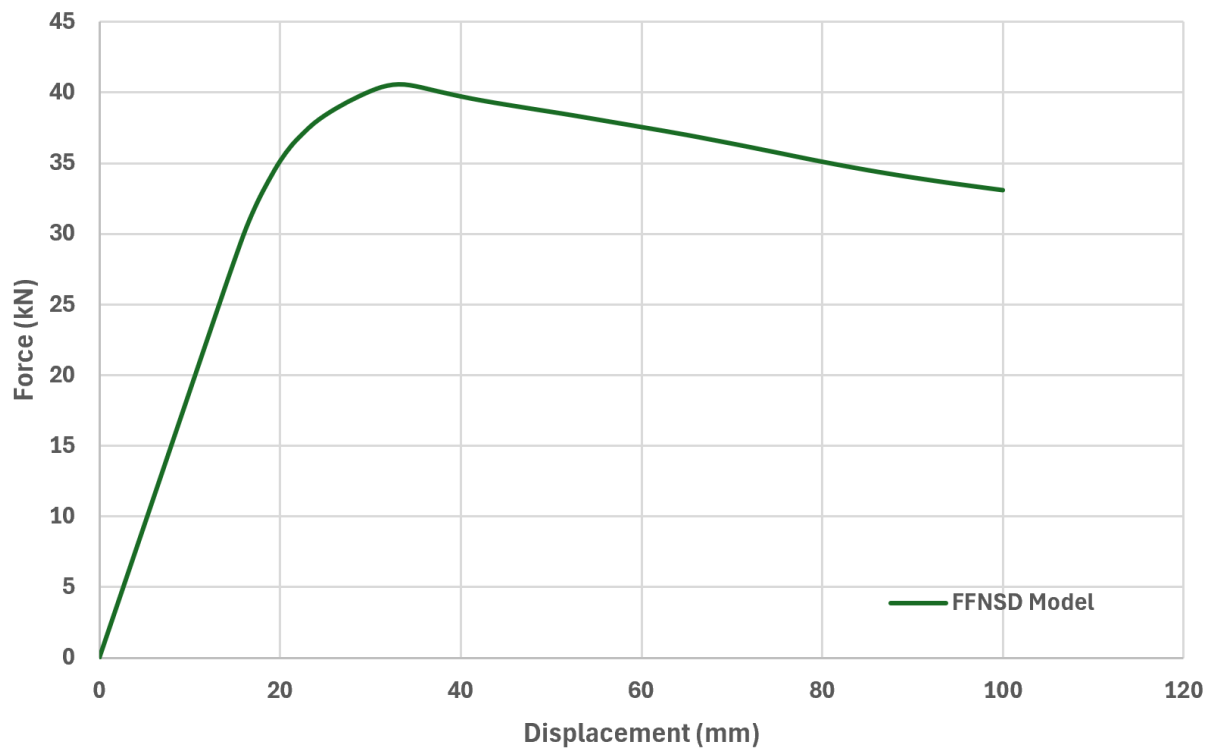


Figure 5.105: Force-Displacement Diagram-FFNSD Model

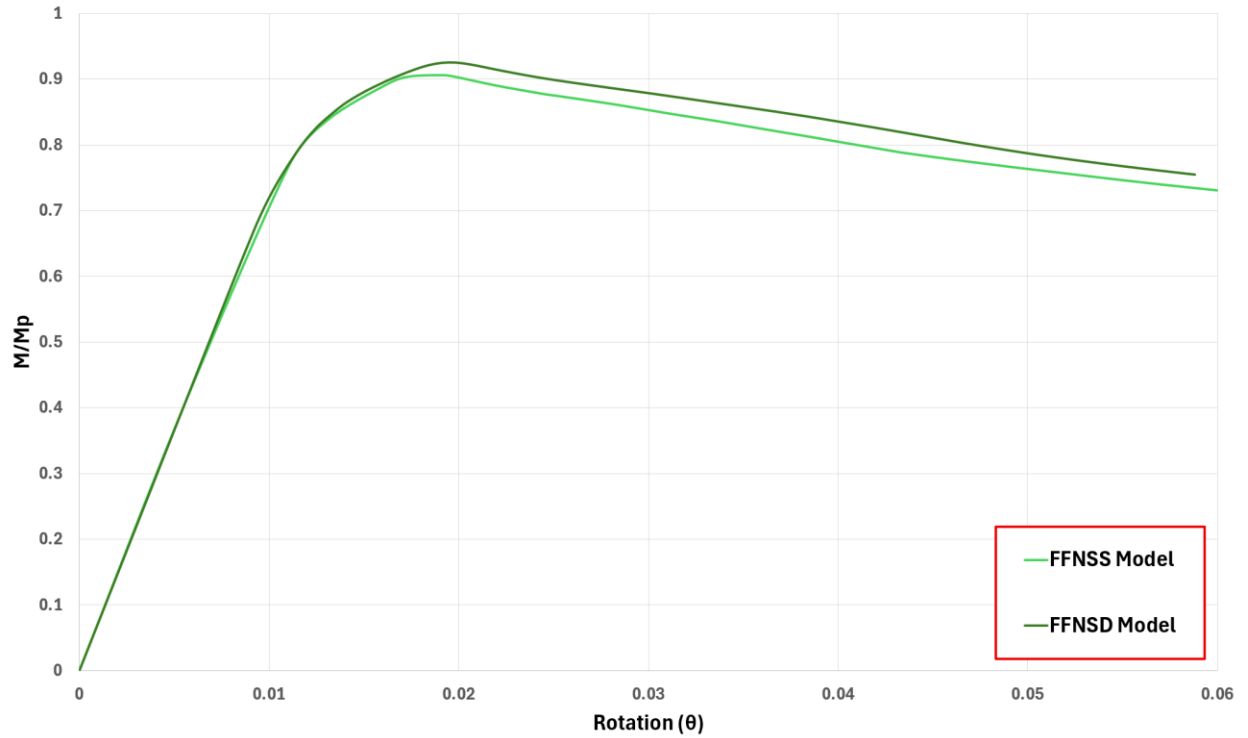


Figure 5.106: Moment-Rotation Diagram-FFNSD Model

## ***(2) a beam with vertical and horizontal stiffeners***

An additional model incorporating vertical and horizontal stiffeners, similar to the verified model A3 from the referenced experimental test, was introduced not only to enhance local buckling resistance and flexural capacity but also to serve as a benchmark for comparison. This configuration was evaluated against both the baseline model without any stiffeners and an alternative solution in which the stiffeners were replaced with concrete infill. The analysis was conducted using both static and dynamic simulations.

## FFWSS Model:

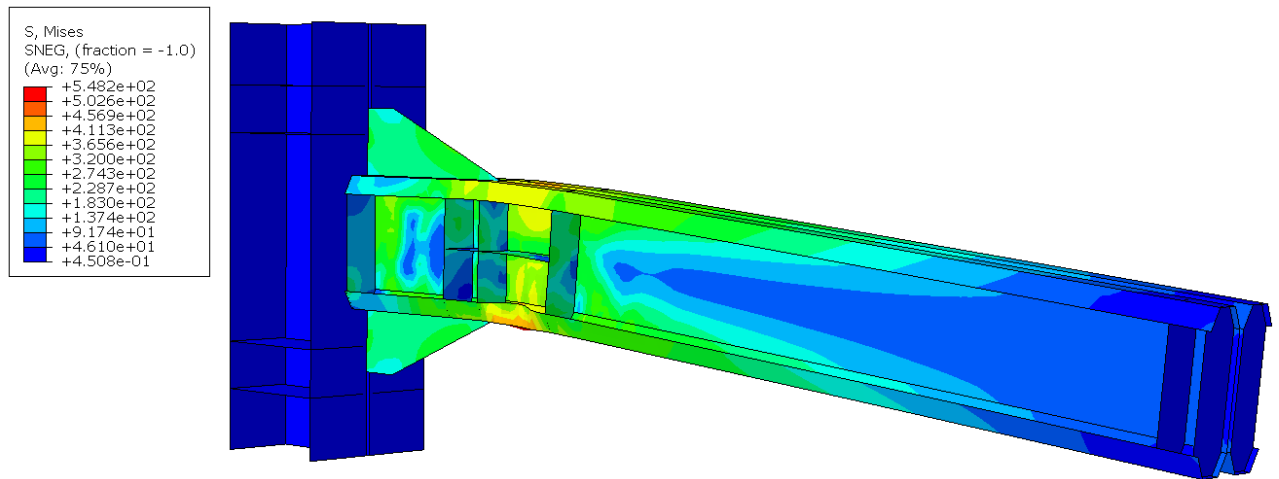


Figure 5.107: Von Mises Stress Contour- FFWSS Model

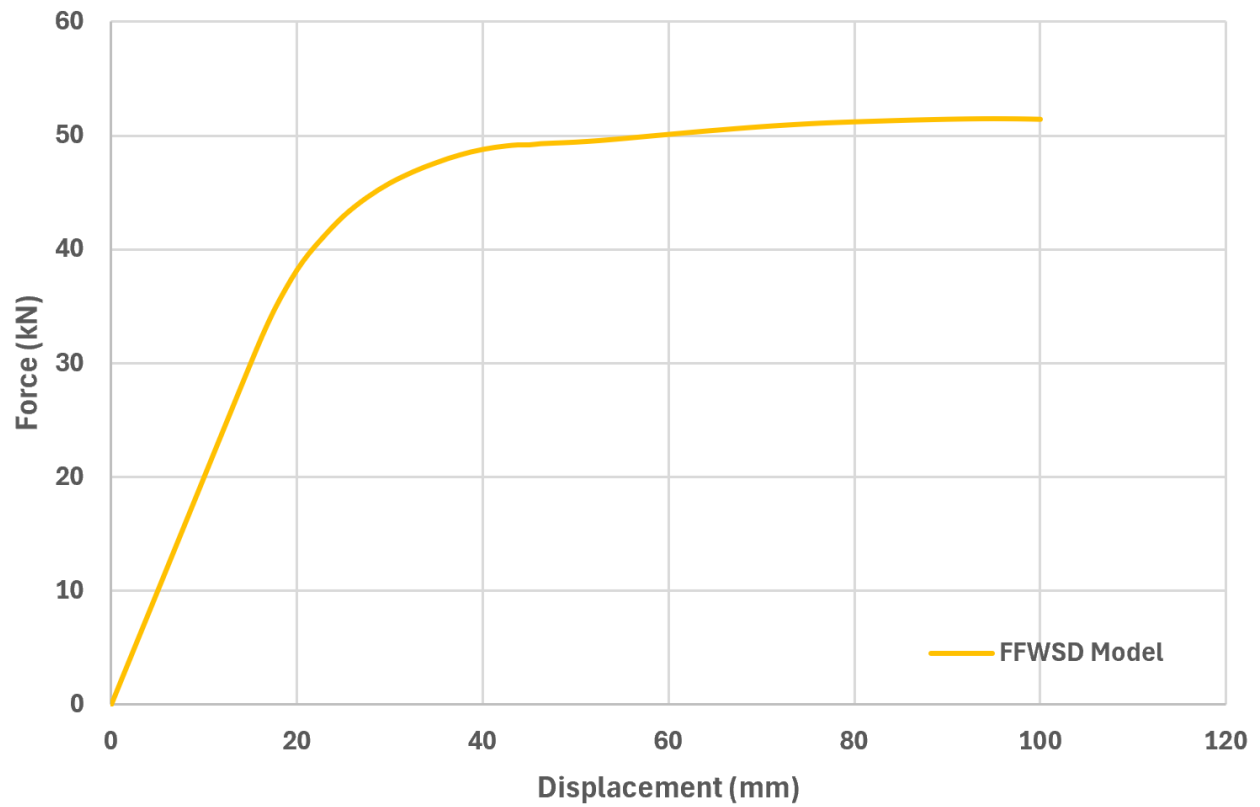


Figure 5.108: Force-Displacement Diagram-FFWSS Model



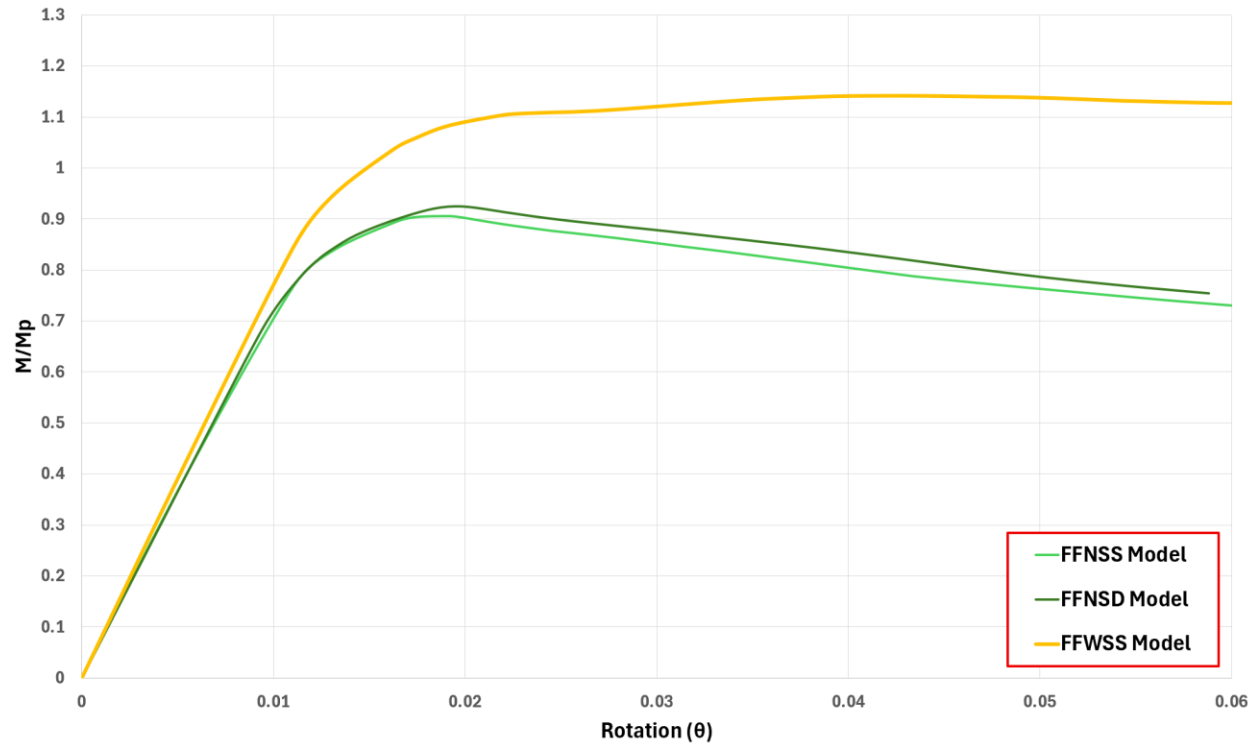


Figure 5.109 : Moment-Rotation Diagram-FFWSS Model

### FFWSD Model:

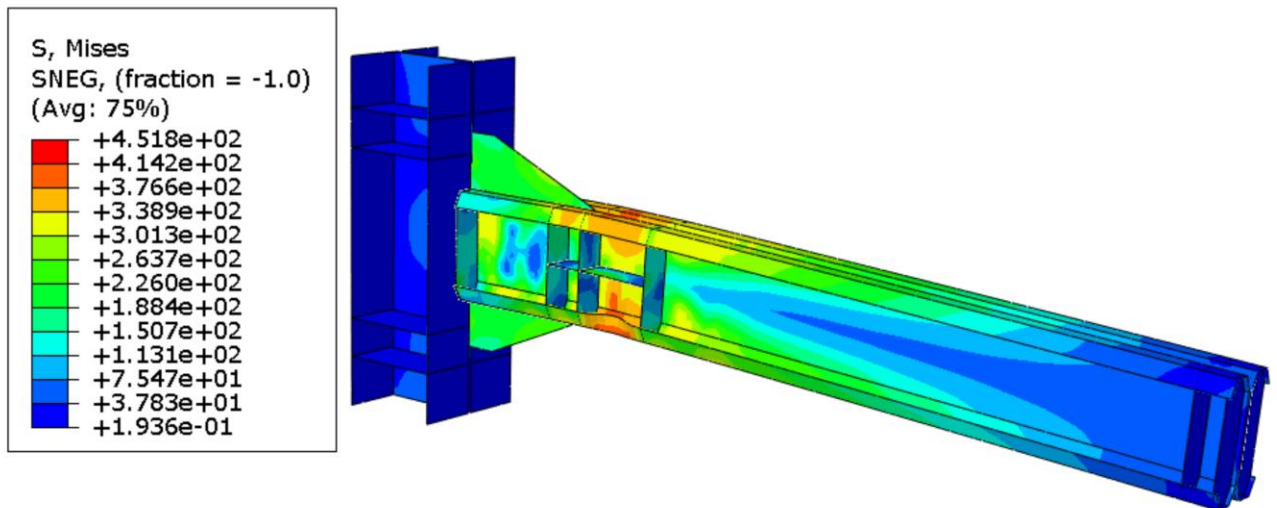


Figure 110: Von Mises Stress Contour- FFWSD Model

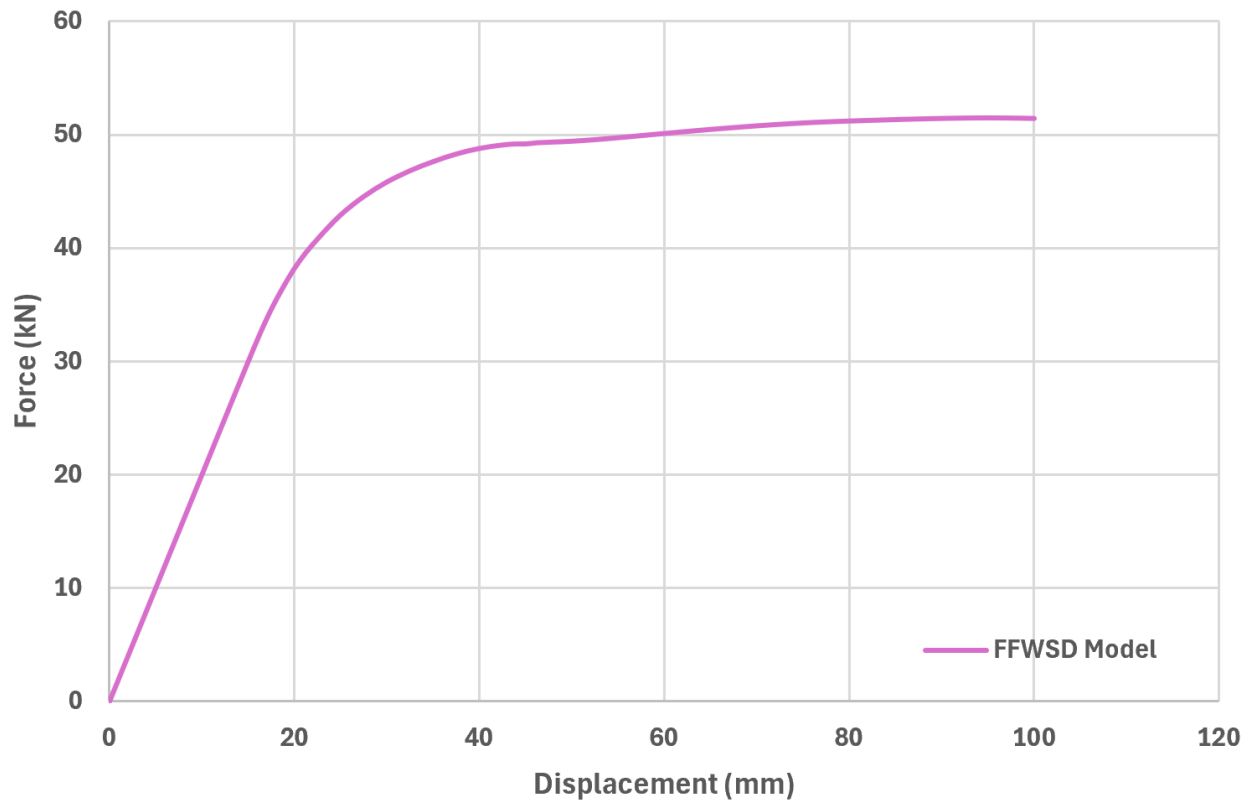


Figure 5.111: Force-Displacement Diagram-FFWSD Model

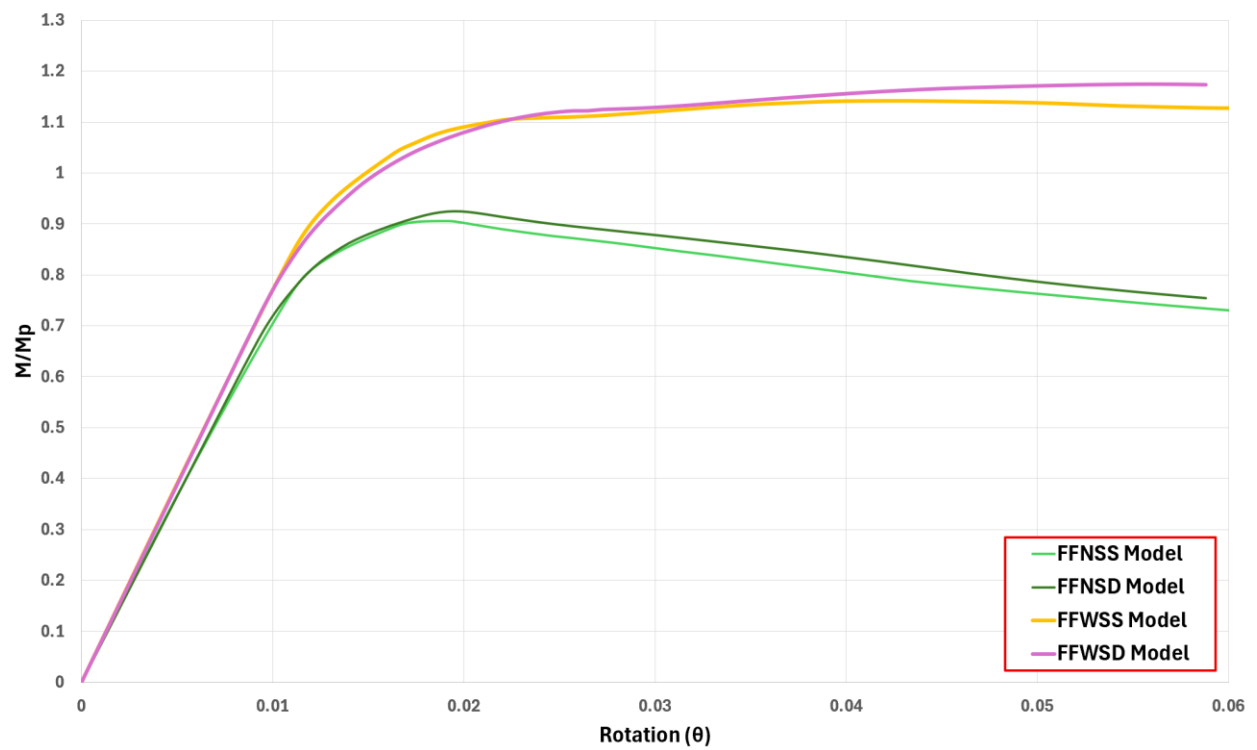


Figure 5.112: Moment-Rotation Diagram-FFWSD Model

### (3) a beam in which the stiffeners were replaced with a plain concrete infill

In the final models, the stiffeners were replaced with plain C40 concrete, cast into the beam cavity over a 600 mm length at the connection zone. The aim was to explore the strengthening effect of the infill concrete under full bond conditions. With the steel–concrete interface fully tied, the system was assumed to exhibit full composite behavior, allowing efficient stress transfer and improved structural performance at the joint.

#### FFFBES Model:

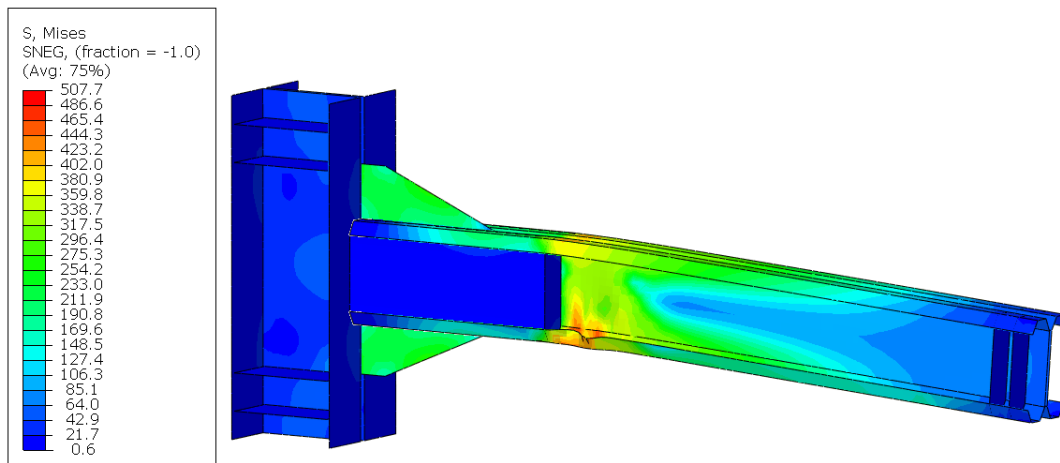


Figure 5.113: Von Mises Stress Contour- FFBES Model

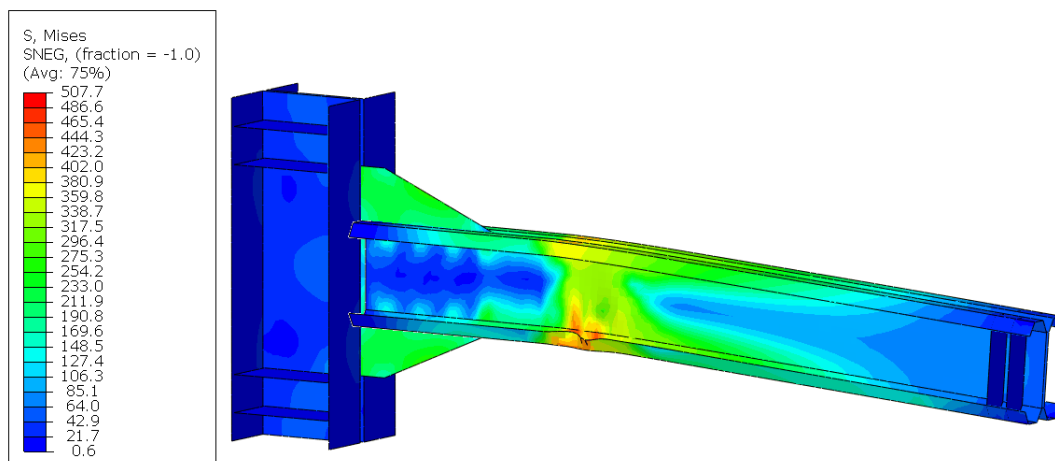


Figure 5.114: Von Mises Stress Contour in CFS Beam- FFBES Model

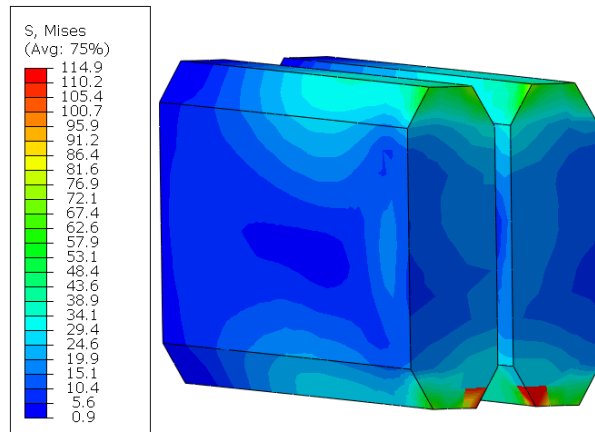


Figure 5.115: Von Mises Stress Contour in Concrete Infill- FFFBES Model

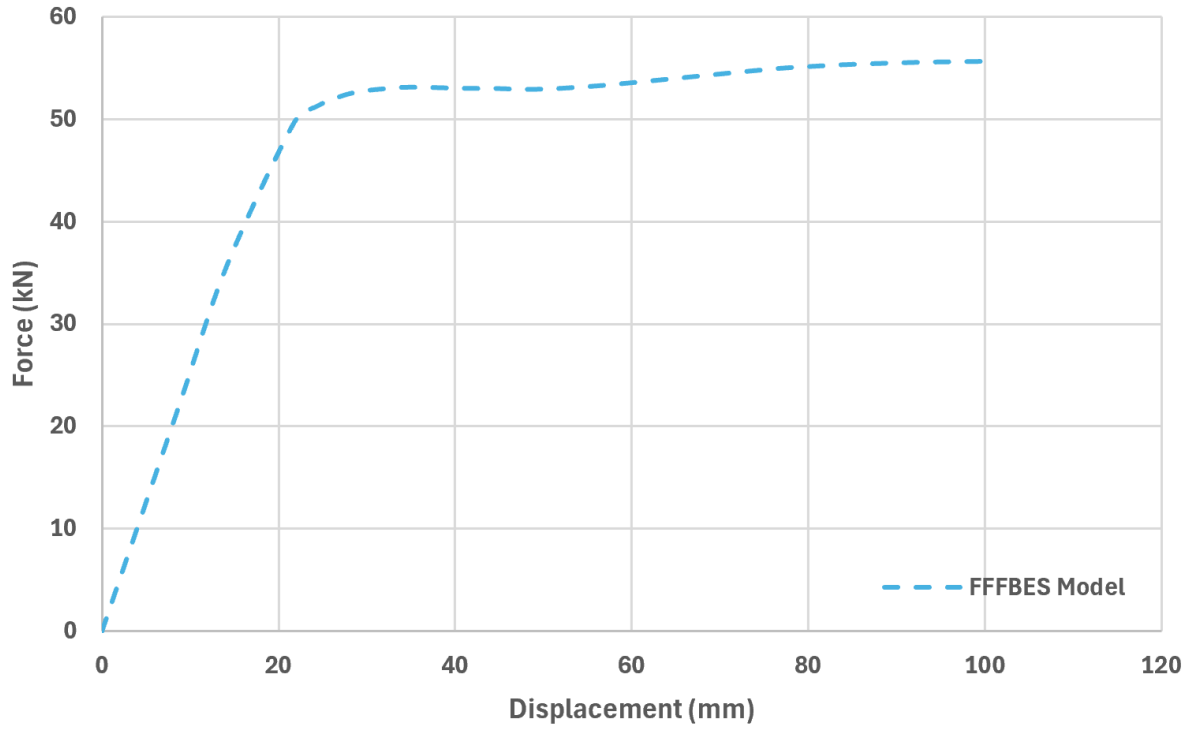


Figure 5.116: Force–displacement curve for FFFBES Model

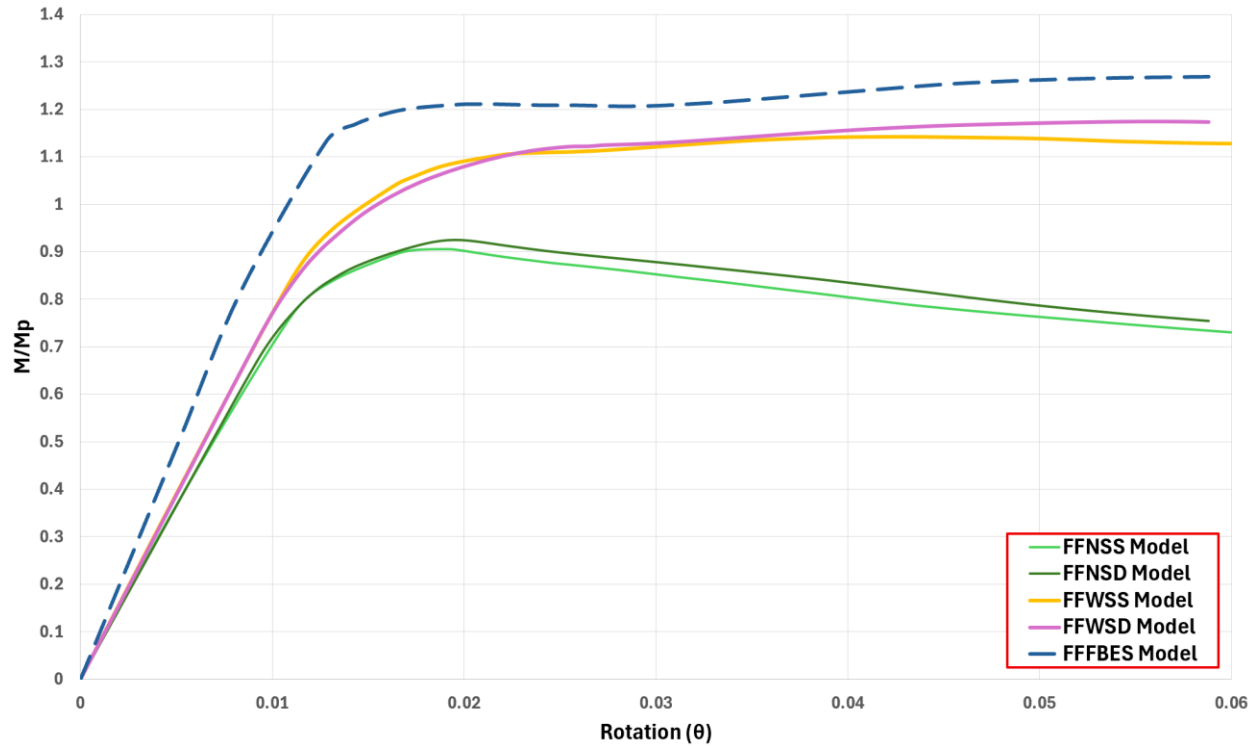


Figure 5.117: Moment-Rotation Diagram-FFFBES Model

### FFFBPD Model:

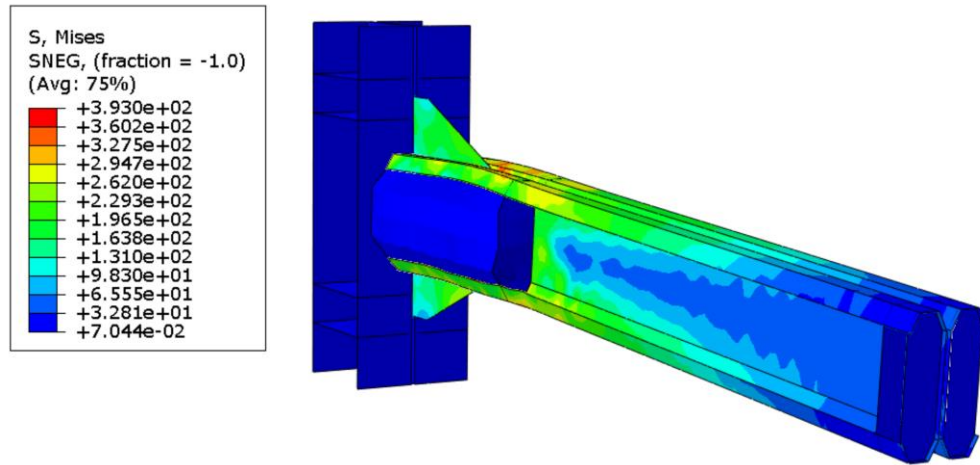


Figure 5.118: Von Mises Stress Contour- FFBPD Model

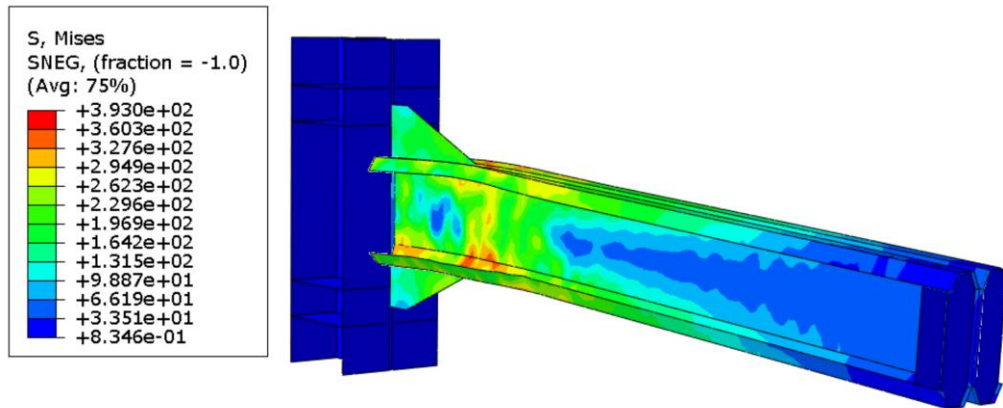


Figure 5.119: Von Mises Stress Contour in CFS Beam- FFFBPD Model

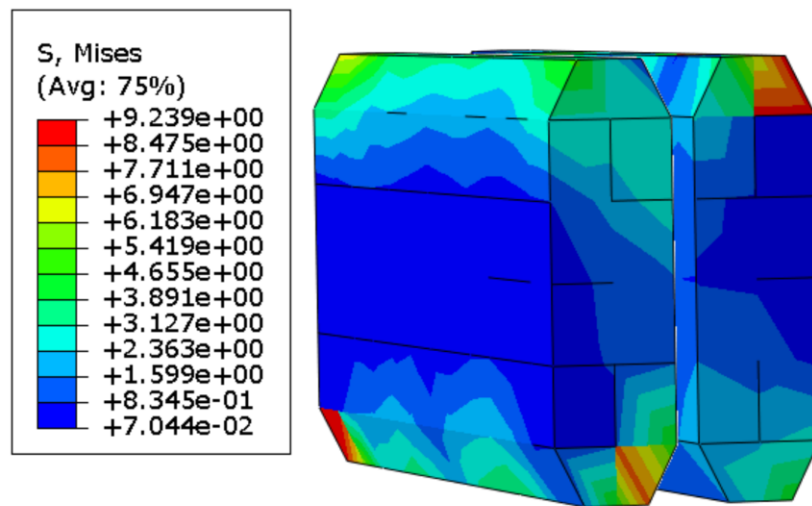


Figure 5.120: Von Mises Stress Contour in Concrete Infill- FFFBPD Model

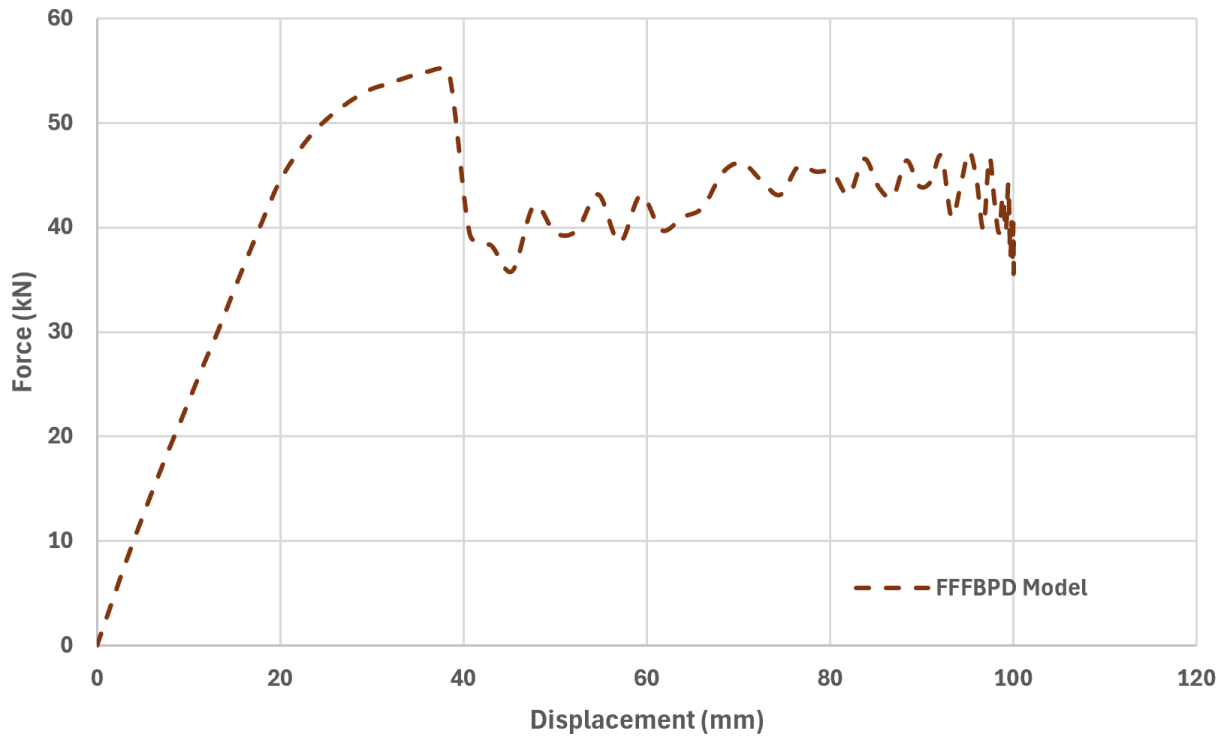


Figure 5.121 : Force-displacement curve for FFFBPD Model

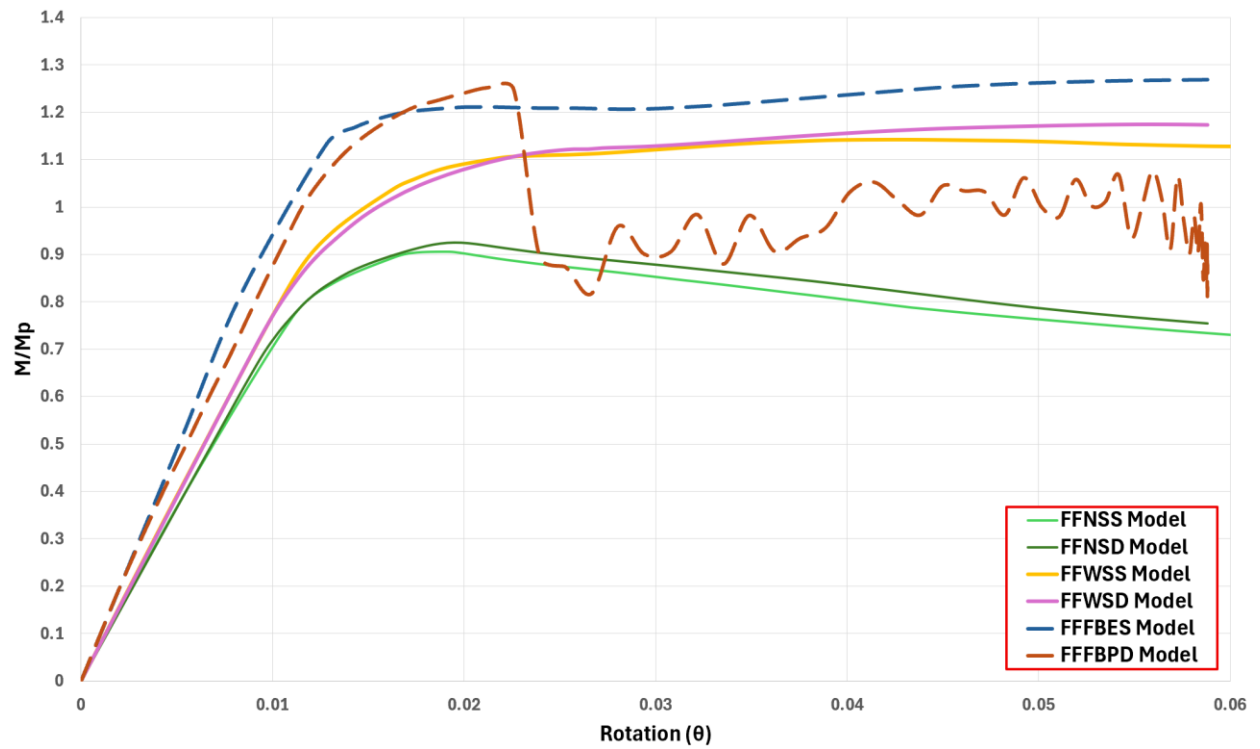


Figure 5.122: Moment-Rotation Diagram-FFFBPD Model

## 5.2 Comparative Analysis of Normalized Moment–Rotation Behavior

To evaluate the effectiveness of different stiffening strategies in folded flange (FF) beams, a normalized moment–rotation analysis was conducted. All models are compared based on normalized moment capacity ( $M/M_p$ ) plotted against rotation ( $\theta$ ). This method offers a clear, objective comparison of structural stiffness and capacity. In this study:

- The plastic moment capacity ( $M_p$ ) of the folded flange beam is considered as 74.6 kN·m.
- The moment ( $M$ ) is calculated by multiplying the reaction force ( $F$ ) by the distance from load point to connection zone, which is 1.7 m.
- The rotation ( $\theta$ ) is computed as the displacement ( $\delta$ ) at the load point divided by the same 1.7 m arm.

### 5.2.1 Main Model Response: FFNSS and FFNSD

The FFNSS model exhibited the lowest moment capacity, with a maximum normalized moment of approximately  $0.9 M/M_p$ , classifying it as a partial-strength joint according to EN 1993-1-8 [42]. It failed early due to local buckling and yielding at the flange–web connections. Its moment–rotation curve showed a sharp peak followed by a steep decline, indicating brittle behavior with minimal post-peak resistance and energy dissipation. This configuration serves as the reference benchmark for all other models. The dynamic counterpart, FFNSD, demonstrated a similar failure mechanism but with a slightly higher post-peak residual capacity than FFNSS. However, its maximum moment also remained near  $0.9 M/M_p$ , confirming its partial-strength nature. Both models confirm that in the absence of any stiffener, folded flange beams are highly susceptible to premature failure and exhibit poor rotational capacity, underscoring the need for stiffening or composite action.



### 5.2.2 Steel Stiffener Models: FFWSS and FFWSD

Both stiffened models exhibited significant improvements compared to the unstiffened models (FFNSS and FFNSD), which reached a maximum normalized moment of approximately  $0.9 M/M_p$ . The FFWSS model achieved a peak normalized moment of around  $1.20 M/M_p$ , reflecting a 33% increase in strength, thereby classifying it as a full-strength joint according to EN 1993-1-8 [42]. Unlike the sharp post-peak drop seen in FFNSS, the FFWSS curve displayed a gradual and stable upward trend, indicating enhanced flexural stiffness and better control of local buckling. Similarly, the FFWSD model (dynamic version) reached a comparable peak of about  $1.20 M/M_p$  and exhibited an even smoother post-peak response, with a continually rising or plateauing trend rather than a decline. This improved curve shape implies better energy dissipation, even though the overall rotation capacity remains moderate. In contrast to the brittle and unstable response of the unstiffened models, both FFWSS and FFWSD demonstrated stable and resilient performance, confirming their classification as full-strength joints and making them effective stiffening strategies for increasing strength and delaying failure mechanisms in folded flange beams.

### 5.2.3 Fully Bonded Concrete Infill Models – FFFBES and FFFBPD

The FFFBES and FFFBPD models represent the most integrated concrete–steel interaction, both employing a full bond (tie constraint) between the infill concrete and the folded flange beam. The FFFBES model adopts a linear elastic approach for concrete, while the FFFBPD model uses the Concrete Damaged Plasticity (CDP) model to capture nonlinearities, cracking, and post-peak softening. Among all models, FFFBES demonstrates the most favorable performance, maintaining a stable and increasing moment–rotation response throughout the entire range, with no evident strength loss. In comparison, FFFBPD shows an early peak followed by a notable strength drop and oscillations, reflecting damage evolution and reduced confinement effectiveness typical in CDP simulations. When compared to the steel-stiffened configurations (FFWSS and FFWSD), the FFFBES model exhibits higher peak strength and more stable post-peak behavior, achieving a clear full-strength classification. The stiffened models, while effective in enhancing the performance over the main models, show slightly lower moment capacity and more gradual post-peak stabilization, particularly under dynamic loading (FFWSD). In contrast, the main models (FFNSS and FFNSD), which lack any stiffening or concrete enhancement, display the weakest

responses. Both show limited strength development and noticeable post-peak degradation, remaining in the partial-strength category. Overall, the results confirm that full-bonded concrete infill, especially with elastic modeling, offers superior performance to both conventional steel stiffeners and the main unstiffened configurations. It enhances both the strength and rotational stability of CFS joints, making it a promising solution for achieving full-strength structural connection classification.

# Chapter 6. Conclusions and Recommendations for Future Work

## Summary of Key Findings

This study focused on enhancing the structural performance of cold-formed steel (CFS) bolted moment connections by introducing concrete infill into the beam-column joint region. CFS elements are gaining increasing attention in modern construction not only for their high material efficiency and cost-effectiveness but also for their environmental advantages, including lower energy demand during production and reduced CO<sub>2</sub> emissions compared to traditional hot-rolled steel. These characteristics position CFS as a more sustainable structural solution, especially when paired with efficient connection strategies. A series of finite element models developed in ABAQUS were used to evaluate the effectiveness of three joint configurations, main unstiffened models, steel-stiffened models, and fully bonded concrete-infilled models based on their normalized moment–rotation behavior. The modeling approach was first validated through cyclic (hysteretic) analysis of back-to-back curved CFS beams, showing strong agreement with experimental data in terms of stiffness, energy dissipation, and strength degradation. This validation ensured the reliability of subsequent simulations involving folded flange (FF) beam models.

Key insights from the simulations include:

- Unstiffened models (FFNSS/FFNSD) showed limited strength (peak at around  $0.9 M/M_p$ ), classifying them as partial-strength joints.
- Steel-stiffened models (FFWSS/FFWSD) significantly improved performance, achieving approximately  $1.20 M/M_p$ , meeting full-strength classification.
- Fully bonded models revealed a key contrast:
  - The FFFBES model, using elastic concrete, demonstrated the best performance with smooth, stable strength development and full-strength classification.
  - The FFFBPD model, incorporating Concrete Damaged Plasticity (CDP), showed early peak strength followed by substantial degradation, falling back into the partial-strength category.

These results emphasize the importance of concrete modeling under full bond conditions. Even with a simple elastic assumption, the fully bonded concrete infill configuration outperformed both the main and steel-stiffened models in terms of peak strength and post-peak stability. Under full composite interaction, the choice of concrete model plays a pivotal role in determining joint efficiency.

In conclusion, the integration of sustainable CFS members with optimized concrete-filled connections not only addresses structural design challenges but also aligns with environmental goals, offering a structurally and ecologically efficient solution for modern construction. Compared to welded steel stiffeners which require additional fabrication time, welding operations, and labor, using concrete infill in the connection zone presents a simpler, faster, and more cost-effective alternative, reducing on-site complexity while still achieving full-strength performance under full bond conditions.

## Future Work Recommendations

Based on the findings of this research, several potential directions for future work are proposed:

- **Experimental Validation of Folded Flange Configurations:** Conduct full-scale experimental testing on selected FF beam configurations, especially the FFFBES and FFFBPD models, to validate the numerical results and assess real-world behavior under cyclic or seismic loading.
- **Improved CDP Modeling and Mesh Optimization:** Investigate the effects of mesh density, element types, and tension-compression damage parameters in CDP to reduce localization issues and enhance stability in post-peak regions.
- **Anchorage and Stiffening Strategies:** Explore the use of mechanical anchorage, shear connectors, or embedded reinforcement to improve concrete confinement in the joint region, particularly for nonlinear CDP models under dynamic loading.
- **Parametric Studies and Design Guidelines:** Conduct broader parametric studies involving varying concrete grades, steel thicknesses, connection geometries, and interface conditions to develop generalized design charts or simplified formulas for practical engineering use.
- **Interface Behavior and Slip Effects:** Study the frictional interaction between concrete and steel at the interface by introducing slip conditions and varying friction coefficients. This would allow for a more realistic representation of partially bonded behavior and improve understanding of composite action degradation under seismic or cyclic demands.

## Bibliography

- 1- European Parliament. Directive (EU) 2018/844 of the European Parliament and of the Council of 30 May 2018 amending Directive 2010/31/EU on the energy performance of buildings and Directive 2012/27/EU on energy efficiency. Off. J. Eur. Union 2018, 156, 75–91.
- 2- <https://steelnet.org/>
- 3- Ross P.D. Johnston. Sustainability of Cold-formed Steel Portal Frames in Developing Countries in the Context of Life Cycle Assessment and Life Cycle Costs.
- 4- Lim JBP, Nethercot DA. Design and development of a general cold- formed steel portal frame system. Struct Eng 2002;80(21):31–40.
- 5- Dubina, D., Ungureanu, V., & Landolfo, R. (2013). Design of cold-formed steel structures: Eurocode 3: Design of steel structures
- 6- Gardner Nethercot. 2015. Designers' Guide to Eurocode 3: Design of Steel Buildings, 2nd ed. ICE Publishing.
- 7- American Iron and Steel Institute. (1946). Specification for the Design of Light Gage Steel Structural Members. AISI-Specifications for the Design of Cold-Formed Steel Structural Members
- 8- EN 1993-1-3 (2006) (English): Eurocode 3: Design of steel structures - Part 1-3: General rules - Supplementary rules for cold-formed members and sheeting [Authority: The European Union Per Regulation 305/2011, Directive 98/34/EC, Directive 2004/18/EC]
- 9- AISI S100-16. North American specification for the design of cold-formed steel structural members. Washington, DC: American Iron and Steel Institute; 2020.
- 10- <https://buildsteel.org/>
- 11- AISI S400-15. North American standard for seismic design of cold-formed steel structural systems. Washington, DC: American Iron and Steel Institute; 2015.
- 12- Seismic Design of Cold-Formed Steel Lateral Load-Resisting Systems (NEHRP Seismic Design Technical Brief No. 12)
- 13- Bagheri Sabbagh A, Petkovski M, Pilakoutas K, Mirghaderi R. Ductile moment-resisting frames using cold-formed steel sections: an analytical investigation. J Constr Steel Res 2011;67:634–46.

- 14- Bagheri Sabbagh A, Petkovski M, Pilakoutas K, Mirghaderi R. Development of cold-formed steel elements for earthquake resistant moment frame buildings. *Thin Walled Struct* 2012;53:99–108.
- 15- Bagheri Sabbagh A, Petkovski M, Pilakoutas K, Mirghaderi R. Experimental work on cold-formed steel elements for earthquake resilient moment frame buildings. *Eng Struct* 2012;42:371–86.
- 16- A. Bagheri Sabbagh, M. Petkovski, K. Pilakoutas, R. Mirghaderi, Cyclic behaviour of bolted cold-formed steel moment connections: FE modelling including slip, *J. Constr. Steel Res.* 80 (2013) 100–108.
- 17- J. Ye, S.M. Mojtabaei, I. Hajirasouliha. Seismic performance of cold-formed steel bolted moment connections with bolting friction-slip mechanism, *J. Constr. Steel Res.* 156 (2019) 122–136.
- 18- J. Ye, S.M. Mojtabaei, I. Hajirasouliha, K. Pilakoutas. Efficient design of cold-formed steel bolted-moment connections for earthquake resistant frames, *Thin-Walled Structures* 150 (2020) 105926.
- 19- I. Papargyriou, S.M Mojtabaei, I. Hajirasouliha, J. Becque, K. Pilakoutas. Cold-formed steel beam-to-column bolted connections for seismic applications, *Thin-Walled Structures* 172 (2022) 108876.
- 20- Daryl L. Logan, *A First Course in the Finite Element Method*, University of Wisconsin–Platteville.
- 21- Tahouni, S. (Year). *Finite Element Method for Structural Analysis (in Persian)*. Tehran: University of Tehran Press. شاپور طاهونی، اجزای محدود برای تحلیل سازه ها
- 22- Dassault Systèmes Simulia. (2022). *Abaqus 2022 documentation*. Dassault Systèmes.
- 23- M.R. Haidarali, D.A. Nethercot, Finite element modelling of cold-formed steel beams under local buckling or combined local/distortional buckling, *Thin-Walled Struct.* 49 (2011) 1554–1562.
- 24- A.B. Sabbagh, *Cold - Formed Steel Elements for Earthquake Resistant Moment Frame Buildings (Ph.D. thesis)*, The University of Sheffield, 2011.
- 25- W. Ramberg, W. Osgood, *Description of Stress–Strain Curves by Three Parameters*, Technical Note No. 902, National Advisory Committee for Aeronautics, Washington, D.C., USA, 1943.

- 26- N. Hill, Determination of Stress–Strain Relations from the Offset Yield Strength Values, Technical Note No. 927, 1944.
- 27- K.J.R. Rasmussen, Full-range stress–strain curves for stainless steel alloys, J. Constr. Steel Res. 59 (2003) 47–61.
- 28- Mander JB, Priestley MJN, Park R. Theoretical stress–strain model for confined concrete. Journal of Structural Engineering, ASCE 1988;114(8):1804–26.
- 29- Richart FE, Brandzaeg A, Brown RL. A study of the failure of concrete under combined compressive stresses. Bull. 185. Champaign (IL, USA): University of Illinois Engineering Experimental Station; 1928.
- 30- G. Campione, M. Fossetti, Compressive behavior of concrete elliptical columns confined by single hoops. Engineering Structures 29 (2007) 408–417.
- 31- X. Zha, G. Gong and X. Liu, Study on behavior of concrete filled elliptical steel tube members. Advanced Steel Construction Vol. 9, No. 2, pp. 90-107 (2013).
- 32- EN 1992-1-1 (2004) (English): Eurocode 2: Design of concrete structures – Part 1-1: General rules and rules for buildings [Authority: The European Union Per Regulation 305/2011, Directive 98/34/EC, Directive 2004/18/EC]
- 33- Hu HT, Huang CS, Wu MH, Wu YM. Nonlinear analysis of axially loaded concrete-filled tube columns with confinement effect. Journal of Structural Engineering, ASCE 2003;129(10):1322–9.
- 34- Ehab Ellobodya, Ben Young, Dennis Lamc. Behaviour of normal and high strength concrete-filled compact steel tube circular stub columns. Journal of Constructional Steel Research 62 (2006) 706–715.
- 35- H. Hu, C. Huang, M. Wu and Y Wu, Nonlinear Analysis of Axially Loaded Concrete-Filled Tube Columns with Confinement Effect, Journal of Structural Engineering · October 2003.
- 36- Dassault Systèmes Simulia. (2006). *Abaqus 6.6 documentation*. Dassault Systèmes.
- 37- AISC, Seismic Provisions for Structural Steel Buildings, ANSI/AISC 341-16, 2016.
- 38- J Lubliner, J Oliver, S Oller, and E Onate. A plastic-damage model for concrete, 1989.
- 39- Jeeho Lee and Gregory L. Fenves. Plastic-damage model for cyclic loading of concrete structures. Journal of Engineering Mechanics, 124:892–900, 8 1998. ISSN 0733-9399.



- 40- Hafezolghorani M., Hejazi F., Vaghei R., bin Jaafar M.S., Karimzade K., Simplified damage plasticity model for concrete, *Structural Engineering International*, 27(1): 68–78, 2018.
- 41- Davies J., Observation of fracture path development in mortar beam specimens, *Advn. Cem. Bas. Mat.*, 3(1996)31-36.
- 42- CEN (European Committee for Standardization). (2005). EN 1993-1-8: Eurocode 3 – Design of steel structures – Part 1-8: Design of joints. Brussels: CEN.